UNIVERSITÀ DI TRENTO
Department of Industrial Engineering

Doctoral School in Materials, Mechatronics and Systems Engineering

XXXV cycle

Advancing three-dimensional electrophysiology: Development and evaluation of versatile platform for tailored 3D microelectrode array fabrication

Neeraj Yadav

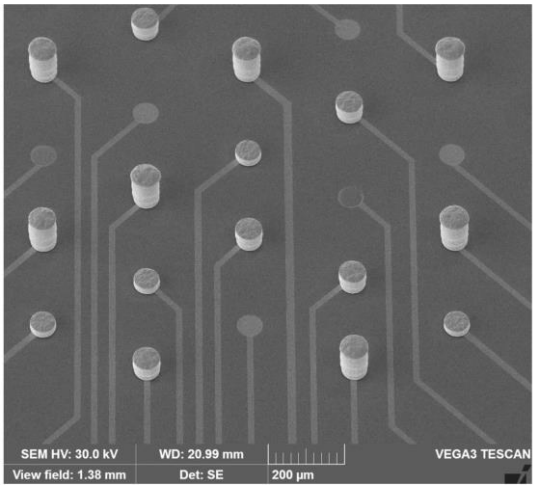

February 2024

ADVANCING THREE-DIMENSIONAL ELECTROPHYSIOLOGY: DEVELOPMENT AND EVALUATION OF VERSATILE PLATFORM FOR TAILORED 3D MICROELECTRODE ARRAY FABRICATION

Neeraj Yadav
E-mail: neeraj.yadav@unitn.it

Approved by:

Dr.Leandro Lorenzelli, Advisor
Center for Sensors & Devices (SD)
Foundation Bruno Kessler, Italy.

Dr.Andrea Adami, Advisor
Center for Sensors & Devices (SD)
Foundation Bruno Kessler, Italy.

Prof. Ing. Gian-Franco Dalla Betta, Advisor
Department of Industrial Engineering
University of Trento, Italy.

Ph.D. Commission:

Prof. Lucio Pancheri,
Department of Industrial Engineering
University of Trento, Italy.

Prof. Stefano Vassanelli,
Department of Biomedical Sciences
University of Padova, Italy.

Prof. Albert Romano Rodriguez,
Department of Electronic and Biomedical Engineering
University of Barcelona, Spain.

University of Trento,
Department of Industrial Engineering

February 2024

University of Trento - ***Department of Industrial Engineering***

Doctoral Thesis

Neeraj Yadav – February 2024
Published in Trento (Italy) – by University of Trento

Dedicated to all Doctors, Nurses, Researchers, and other Medical Staff who worked tirelessly and selflessly during peak COVID-19 times.

Table of Contents

Abbreviations

MEA: Microelectrode array

ECM: Extracellular matrix

SNR: Signal-to-noise ratio

PVD: Physical vapor deposition

SEM: Scanning electron microscopy

AFM: Atomic force microscopy

XRD: X-ray diffraction

FWHM: Full width at half maximum

PDMS: Polydimethylsiloxane

HMDS: Hexamethyldisilazane

CMOS: Complementary metal-oxide semiconductor

NSED: No sonication electrodeposition

PSED: Pulsed sonication electrodeposition

CSED: Continuous sonication electrodeposition

PECVD: Plasma-enhanced chemical vapor deposition

Abstract

Microelectrode arrays (MEAs) are widely used tools to investigate *in vitro* neuronal networks and acute brain slices. Planar or 2D MEAs have been the conventional standard for decades, enabling the extracellular recording and stimulation of cultured neuronal cells and tissue slices. However, the effectiveness of planar MEAs diminishes when stimulating or recording from 3D *in vitro* neuronal cultures or brain slices owing to rapid data attenuation in the z-direction. Existing 3D *in vitro* neuronal models only permit recording electrophysiological activity from the bottom layer directly connected to planar MEAs. Consequently, to advance and optimize 3D neuronal network systems and comprehensively study the dynamics of neuronal networks across different layers of 3D structures, the development of new three-dimensional microelectrode arrays (3D MEAs) is necessary. Over the last three decades, numerous approaches for developing 3D MEAs have been reported; however, most reported technologies can develop quasi-3D MEAs, that is, 3D MEAs with uniform electrode heights. To fully exploit the potential of 3D neuronal constructs, advanced technological platforms capable of developing versatile 3D MEAs consisting of variable-height electrodes, customizing the array topography on demand, and compatibility with existing readout platforms are required.

This thesis introduces a novel technological platform for fabricating diverse 3D MEA architectures using established micromachining techniques such as lithography and templated-assisted electrodeposition. The key to this platform is an innovative approach that enables selective electrodeposition of 3D electrodes within an array. This technological platform utilizes an advanced method to enhance the deposition rate and uniformity of electrodeposited microstructures, which is crucial for precise control over the electrode height in 3D MEAs. Using template-assisted electrodeposition, this platform facilitated the transformation of planar MEAs into 3D configurations with varying electrode heights. Notably, the platform enables the development of 3D MEAs with up to four different electrode heights using a single layout definition mask, ensuring cost-effectiveness and scalability. This precise control

over electrode height unlocks the potential for tailoring 3D MEAs to specific research needs.

A unique multi-height 3D MEA was created to demonstrate the versatility of the proposed platform. This MEA features uniformly distributed electrodes of four distinct heights across the array, enabling the probing of 3D neuronal constructs from the surface to multiple depths. This unique design approach has the potential to provide insights into cellular activities. The performance of the multi-height 3D MEA was validated through rigorous testing involving the recording of electrophysiological activities from a neurospheroid and comparison with a commercially available 3D MEA with similar electrode layouts. This comparative analysis demonstrates the proposed platform's superiority and adaptability.

This thesis is divided into seven chapters. Chapter 1 lays the groundwork by explaining the significance of electrophysiological investigations in understanding brain function and highlighting the limitations of traditional electrophysiological techniques designed for 2D cultures or tissue slices. This chapter sets the stage for the core focus of this thesis, that is, the development of advanced 3D MEAs consisting of electrodes with variable heights. It outlines the morphological and functional advantages offered by 3D neuronal constructs and introduces the escalating demand for innovative MEAs capable of navigating the complexities of these environments. Furthermore, this chapter discusses state-of-the-art approaches for developing 3D MEAs and identifies the limitations of existing technologies.

Chapter 2 presents a comprehensive overview of the current knowledge landscape in the field of MEA technology in the context of both traditional 2D MEA technology and recent advancements in 3D MEA technology. This chapter delves into the intricacies of each aspect, including design considerations, fabrication techniques, electrode materials, integration and interface electronics, cell-loading methods, recording electrophysiological activities, applications, challenges, and future directions associated with each of these areas. The thorough review presented in this chapter serves as the theoretical foundation for subsequent empirical investigation.

Chapter 3 provides an in-depth analysis of the design philosophy and inception of the MEA fabrication platform, shedding light on the motivations, design objectives, and methodology employed in developing this innovative technology. This chapter is

a crucial building block for subsequent discussions on the fabrication processes and outcomes.

Chapter 4 introduces the conceptualized platform by developing multilevel 3D MEAs using a conceptualized platform consisting of electrodes with three distinct heights. This chapter describes the device layout at the wafer scale and individual MEA levels. This chapter details the layout and functioning of custom circuitry to enable the selective electrodeposition of 3D electrodes. Finally, this chapter highlights the platform's advantages, shortcomings, and potential solutions.

Chapter 5 explores the cutting-edge application of ultrasonic vibrations in template-assisted electrodeposition to enhance the fabrication of three-dimensional (3D) microelectrode arrays (MEAs). Building on the insights from Chapter 4, which highlighted the development of multilevel 3D MEAs using the proposed platform, this study aimed to overcome the limitations of conventional electrodeposition methods. By incorporating ultrasonic vibrations into the electrodeposition process, this chapter seeks to increase the deposition rate and improve the uniformity of microstructures, such as micropillars, within MEAs.

Chapter 6 details the development of a multi-height 3D MEA comprising four electrode heights. This was achieved using optimized layouts and an enhanced electrodeposition process incorporating ultrasonic vibrations. This marks the culmination of extensive research. This chapter presents the empirical results of electrophysiological recordings, including their interpretation and comparison with existing state-of-the-art commercial 3D MEA.

Finally, Chapter 7 offers a reflective synthesis. It summarizes the research findings, accentuates their significance, and underscores their contributions to the field. Importantly, this chapter sets the stage for future inquiries, identifying unresolved questions and proposing avenues for further research and technological advancements.

This thesis embarks on a multifaceted exploration of seamlessly weaving theoretical frameworks, experimental methodologies, and empirical findings. Through a meticulously structured journey, it endeavors to contribute to the advancement of 3D MEA technology, bridging the gap between traditional electrophysiological tools and the intricacies of 3D neuronal cultures by focusing on the development and application

of advanced 3D MEAs for electrophysiological recordings in 3D neuronal cultures. It delves into the principles of 3D MEA technology, discusses the challenges and solutions to its implementation, and highlights its significance in advancing neuroscientific research.

Chapter I: Introduction

I.1 Significance of electrophysiological investigations

Understanding the complex functioning of the brain is paramount for unraveling the mysteries of neurobiology and addressing neurological disorders [1]. The core of this endeavor lies in the fundamental unit of the nervous system: the neuron. Neurons are crucial for transmitting electrical signals and enabling communication within the brain and throughout the body. These specialized cells comprise three primary components: the cell body (soma), dendrites, and axon (refer to Figure I-1a). Neuronal communication begins when the dendrites receive signals from other neurons. These signals are aggregated within the cell body. If the integrated signal reaches a certain threshold, it triggers the generation of an action potential (refer to Figure I-1b). This action potential, a rapid change in the neuron's membrane potential, travels along the axon, a long projection extending from the cell body. The opening and closing of ion channels facilitate the propagation of the action potential along the axon membrane, leading to depolarization and repolarization. This process, known as neuronal firing, allows electrical signals to travel long distances within the nervous system. Upon reaching the axon terminals, the action potential triggers the dispense of neurotransmitters into the synaptic cleft, the gap between the axon terminal of one neuron and the dendrites of another. The neurotransmitters then bind to receptors on the postsynaptic neuron, initiating electrical signals in the next neuron and perpetuating neuronal communication [2]. The transmission of electrical signals through neurons is a fundamental mechanism underlying various physiological processes, including sensory perception, motor control, and cognitive function. Studying these signals provides invaluable insights into neural circuitry, synaptic plasticity, and disease mechanisms, thereby driving advancements in neurology and biomedical research [3,4].

In vitro investigations using tissue slices and neuronal cultures play a pivotal role in unraveling the intricacies of brain electrophysiology. These experimental platforms offer controlled environments where researchers can meticulously manipulate variables to examine the fundamental mechanisms underlying neuronal function. Tissue slices, typically obtained from specific brain regions, allow the study of intact neural circuits while maintaining physiological architecture and synaptic connections. By employing sophisticated electrophysiological techniques, such as patch-clamp recording [5] and microelectrode arrays [6], researchers can probe the electrical activity of individual neurons and networks within these slices, deciphering the dynamics of synaptic transmission, neuronal excitability, and network synchronization. Moreover, neuronal cultures derived from primary neuronal cultures or stem cell-derived neurons offer a simplified yet highly reproducible system for investigating the cellular and molecular mechanisms underlying neuronal excitability and synaptic plasticity. These cultures enable researchers to manipulate cellular

composition, growth conditions, and pharmacological interventions, thereby facilitating exploring diverse aspects of brain electrophysiology under controlled experimental conditions.

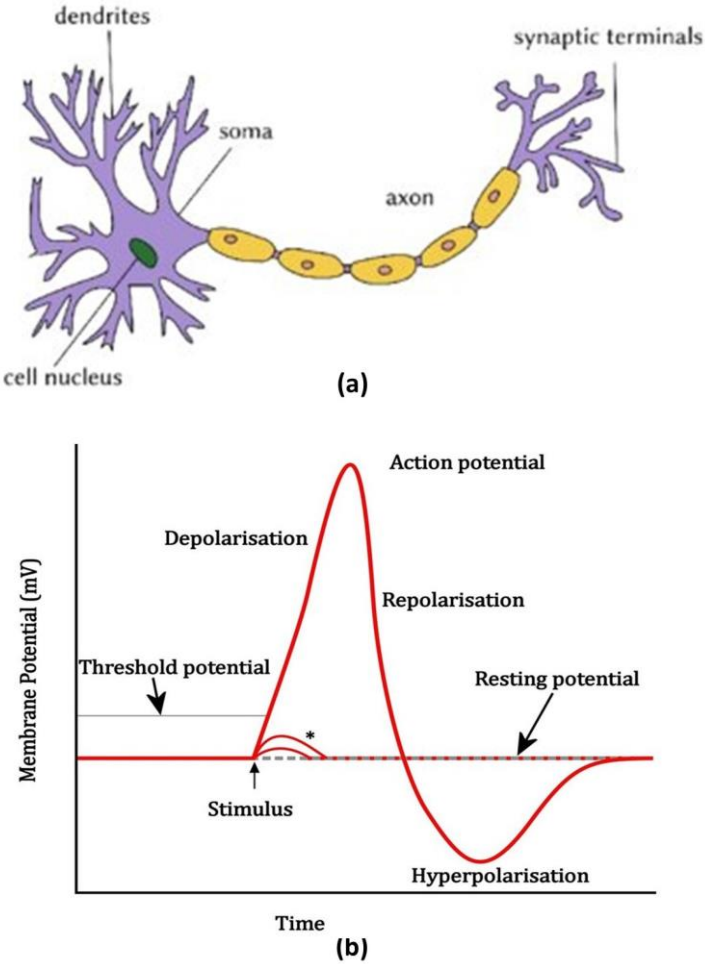

Figure I - 1. Morphology of neurons and the action potential. (a) Sketch of a neuron with annotated morphology. The tree-like dendritic structure receives inputs from other neurons, which are then integrated into the soma. An action potential is generated at the soma. It travels through the axon to synaptic terminals, triggering synaptic transmission to other receiving neurons. (b) Sketch of the temporal course of action potential. If sufficient input arrives, the spike-generating mechanism is activated. The resulting action potential follows a stereotypical form, beginning with strong depolarization followed by hyperpolarization. During the latter, the spike generation is prohibited; hence, it is called the refractory period.[7]

The complexity of the brain arises from its three-dimensional (3D) structure, which encompasses intricate cellular arrangements, cell-cell interactions, and connectivity patterns. To bridge the gap between traditional two-dimensional (2D) neuronal cultures and the native brain environment, researchers have focused on 3D neuronal cultures. These 3D constructs aim to capture the physiological and morphological properties of the neurons observed *in vivo*. 3D neuronal cultures can be generated using various techniques, including cell aggregation methods, scaffold-based approaches, and bioprinting technologies [6]. Three-dimensional (3D) neuronal cultures offer several advantages over 2D cultures. First, neurons in 3D environments exhibit enhanced morphological complexity, including axonal outgrowth and synaptic connections, resembling the *in vivo* neuronal architecture [8]. Second, 3D cultures provide a microenvironment that better mimics the extracellular matrix and cellular interactions in the brain, resulting in improved cell viability, differentiation, and functionality [6]. Finally, 3D neuronal cultures can support the formation of organized neural networks, enabling the study of complex network dynamics, neural circuitry, and synaptic plasticity [9].

These 3D models preserve the spatial arrangement of neurons and better mimic the cellular and extracellular environment of the brain. Consequently, they offer more accurate representations of *in vivo* neurobiology and are particularly beneficial for studying complex brain functions, disease modeling, and drug testing [10]. However, the transition from 2D to 3D neuronal cultures presents new challenges for electrophysiological investigations, as the traditional tools designed for 2D cultures are not equipped to probe electrical activity effectively within 3D neurostructures.

I.2 Investigating electrophysiological activities through MEAs

To capture and analyze neuronal activity, researchers rely on electrophysiological techniques with electrodes serving as essential tools for signal detection. Traditional electrophysiological techniques, such as patch-clamp recording [5], have contributed immensely to our understanding of individual neuronal functions. These methods allow measurement of the electrical activity of a single neuron or a small group of neurons. However, they fail to capture the complex dynamics of large neuronal networks, which comprise many interconnected neurons that interact in a highly coordinated manner.

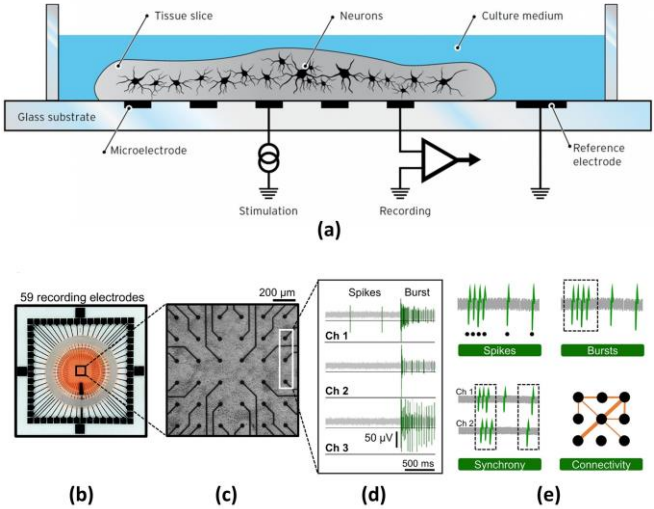

Figure I - 2. *In vitro* Electrophysiological characterization of neuron cultures on MEAs. (a) Schematic representations of an experimental platform for investigating electrophysiological activity using a planar microelectrode array.[11] (b) Photograph of a 60-electrode MEA device. (c) Phase-contrast image of cortical neurons in culture on the MEA. The distance between electrodes is 200 µm. Each black dot corresponds to one of the recording electrodes. (d) Three channels recorded sample traces of spontaneous electrical activity. Electrical events, spikes, and bursts that crossed a threshold (horizontal black line) were recorded. (e) Spontaneous activity of cortical neurons was analyzed according to electrophysiological features of spikes, bursts, synchrony, and connectivity.[12]

The development of conventional microelectrode arrays (MEAs), also known as planar or 2D MEAs, has significantly addressed this limitation. Planar MEAs represent a foundational technology in neuroscience research, facilitating the simultaneous recording of electrical activity from multiple neurons or other electrically excitable cells and providing a more comprehensive view of network dynamics [6]. These arrays consist of flat substrates typically made of materials such as glass or silicon, onto which an array of microscale electrodes is patterned. Electrodes are typically made of conductive metals such as gold, platinum, or iridium oxide. Planar MEAs are configured with a regular grid layout, where each electrode serves as a recording or stimulation site (refer to Figure I-2a). The electrodes are insulated from each other, except for their exposed tips, which come in contact with the cells or tissues being studied. When cells are cultured on the surface of an array, they form direct electrical connections with the electrodes, allowing the array to detect extracellular voltage changes that result from neuronal activity. These changes in voltage, known as action potentials or spikes, are detected as electrical signals by electrodes and can be amplified and recorded using the associated instrumentation (refer to Figure I-2b-e).

Planar MEAs offer several advantages, including the ability to monitor the electrophysiological activity of large populations of cells simultaneously, high spatial resolution, and compatibility with standard laboratory equipment. They have been widely used in various applications, including basic neuroscience research, drug discovery, and neurotoxicity testing.

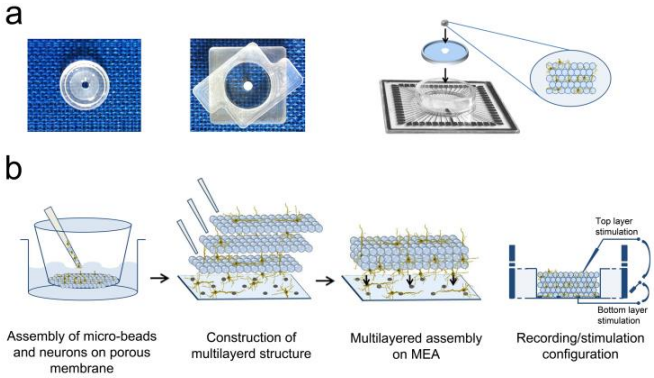

Figure I - 3. Construction of 3D neural networks. (a). Left to right: PDMS structure allowing to confine microbeads and neurons on the recording site area; molder used to build the confinement structure; cartoon that illustrates the final configuration (multi-layers of microbeads and neurons confined by a PDMS structure onto the active area of the Micro-Electrode Array). (b). Main steps for building a 3D neural network. Microbeads were placed onto a porous Transwell® membrane, self-assembled in a hexagonal geometrical structure; dissociated hippocampal cells were plated on such coated microbeads. To obtain a 3D structure, the suspension of neurons and microbeads was moved from the membrane to the MEA surface several times. The last sketch depicts the recording/stimulation configuration: the electrophysiological activity of the 3D network is recorded from the substrate MEA electrodes (bottom layer); the network is stimulated by using both MEA and tungsten electrodes (bottom and top layers).[13]

Employing dissociated neuronal cultures in conjunction with MEAs has become a widely accepted experimental model *in vitro* for studying fundamental aspects of brain function, examining computational characteristics, and understanding electrophysiological responses to electrical or chemical stimuli [14]. Numerous efforts have been undertaken to engineer neuronal networks that closely resemble the microstructured circuits found in the topological organization of the *in vivo* brain [15]. However, in 2008, a significant constraint of *in vitro* experimental models based on dissociated cultures was addressed: the inherent three-dimensional (3D) nature of the brain, which a reduced two-dimensional (2D) configuration cannot adequately replicate, hinders the manifestation of most morphological and electrophysiological characteristics observed *in vivo* [16]. Pautot et al. introduced a protocol in 2008 that facilitated the 3D growth of dissociated hippocampal neurons using a self-assembled scaffold composed of glass microbeads [17]. Subsequently, Frega et al., incorporating this protocol with microelectrode arrays (MEAs), observed distinct patterns of

electrophysiological activity compared with those observed in 2D cultures, characterized by differences in both spiking and bursting features [13,18]. These pioneering studies laid the foundation for 3D cultures to emulate *in vivo* brain properties better. Several subsequent studies have focused on enhancing cell density to approximate *in vivo* conditions and improve scaffold mechanical properties, such as porosity and stiffness, to mimic the extracellular matrix more accurately [19]. Materials such as 3D electrospun polymers and hydrogels have been explored as potential solutions to achieve these objectives. Hydrogels have emerged as promising candidates due to their low cytotoxicity and gas and nutrient exchange facilitation. Natural soft materials, such as collagen, have also been utilized as scaffolds to develop 3D neuronal assemblies.

In 2015, a model of 3D brain-like tissue was established using silk-collagen proteins, in which neurons plated within a porous silk sponge developed extensive projections within a collagen-rich central region, forming dense 3D neuronal networks [20]. However, a significant limitation of many hydrogel-based materials is their rapid mechanical degradation. To address this issue, in 2015, Bosi et al. engineered a synthetic biocompatible PDMS scaffold with tunable micro-and nanomechanical properties [21]. Nonetheless, this type of structure impedes recording electrophysiological activity, as most electrodes are covered by PDMS, rendering the use of planar MEAs ineffective. Moreover, coupling 3D neuronal networks with MEAs presents additional challenges. Existing studies suffer from the intrinsic technological limitations of planar devices, where only a small subset of neurons located in the bottom layer and directly connected to the active area of the MEA can be recorded [22–24]. Recently, efforts have been directed toward developing 3D devices capable of mapping the electrophysiological activity of 3D networks within spatial dimensions. In 2020, Soscia et al. devised an *in vitro* platform to simultaneously measure the electrophysiological activity in three independent 3D cultures [25].

Similarly, in 2021, Shin et al. designed a device capable of recording the electrophysiological activity of *in vitro* 3D assemblies up to a height of 300 µm, thereby providing initial insights into the functional connectivity of 3D neuronal assemblies [26]. However, despite the potential of these technological advancements to overcome experimental limitations, the topological properties of 3D networks, including clusterization, degree distribution, emergence of small-world properties and modular communities, and presence of highly connected neurons (hubs), remain unexplored. Thus, an effective understanding of 3D topology is still lacking [27].

I.3 Progress in 3D MEA technology

Over the past few decades, a rich research landscape has emerged to address the limitations of planar MEA technology in the pursuit of introducing and refining three-dimensional Microelectrode Arrays (3D MEAs). The pioneering work by Thiebaud et al. in 1997 marked a seminal moment in presenting a 3D MEA featuring partially

passivated silicon nitride microelectrodes [28]. The exposed Pt tips, though limited to the top 15 µm, showed early potential by successfully recording responses to picrotoxin from rat hippocampal slices. This early work laid the foundation for subsequent explorations in the field.

Advancing this trajectory, Heuschkel et al. (2002) developed a 3D-MEA with tip-shaped protruding microelectrodes, providing a comparative analysis that underscored the advantages of three-dimensional configurations over their planar counterparts [29]. This work was pivotal in establishing a superior signal magnitude achievable with 3D microelectrodes and setting a benchmark for future designs. Nam et al. 2006 demonstrated the applicability of 3D tip MEAs in interfacing with dissociated neuronal cultures [30]. Notably, the recording quality was comparable to that of conventional 2D flat electrodes but with a reduced noise profile [30]. This advancement underscores the potential of 3D MEAs to mitigate some of the limitations associated with 2D systems.

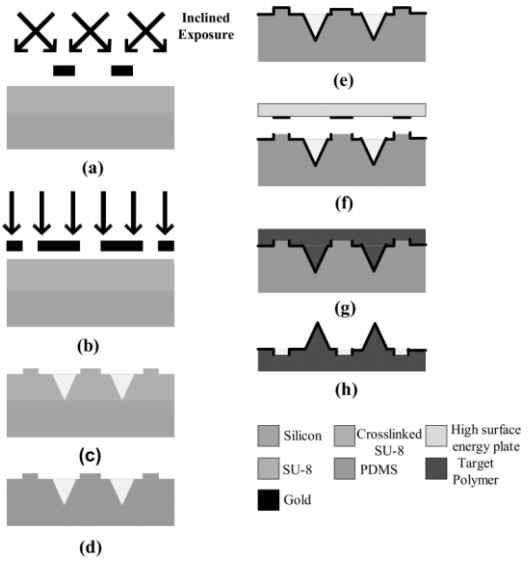

Figure I - 4. Development of metal-transfer-micromolded 3D MEAs consisting of individually addressed 2D and 3D electrodes. (a) Pyramidal pits are exposed on a 700µm thick SU-8 layer using inclined lithography. (b) A second layer of SU-8 (100µm thick) is coated on the mold without developing the first layer, and a mask with metal interconnection patterns is aligned and exposed. (c) After post-exposure baking, both layers are developed simultaneously to obtain a two-layer SU-8 rigid mold. (d) The rigid mold is duplicated twice to create a flexible PDMS mold with identical patterns. (e) Electrodes are defined by evaporating a layer of Au/Cr (500nm/10nm) onto the PDMS mold. (f) The metal transfer is achieved by contacting a high surface energy plate with the metalized PDMS mold, patterning the metal. (g) The target polymer is cast onto the patterned PDMS mold, and various polymers such as SU-8, PMMA, PU, and PDMS can be used. (h) The

device is demolded from the flexible mold, resulting in a patterned 3-D MEA device with 50 individually addressed 2-D and 3-D electrodes.[31]

Rajaraman et al. (2007) proposed an innovative based on metal-transfer micro-molding technology for producing nonplanar metalized patterned microelectromechanical-systems devices such as MEAs on polymeric substrates. This work marked a significant step in enhancing *in vitro* interfacing with neuronal cells and tissue slices, offering a dynamic environment for network growth [31]. However, challenges related to the complexity of the fabrication techniques persist.

Musick et al. (2009) introduced an alternative approach by stacking individually patterned thin films, creating an electrically and fluidically active 3D-MEA [32]. This innovative concept adds versatility to 3D-MEAs, enabling the simultaneous recording and stimulation of neurons. However, challenges remain, particularly in terms of the intricate fabrication processes.

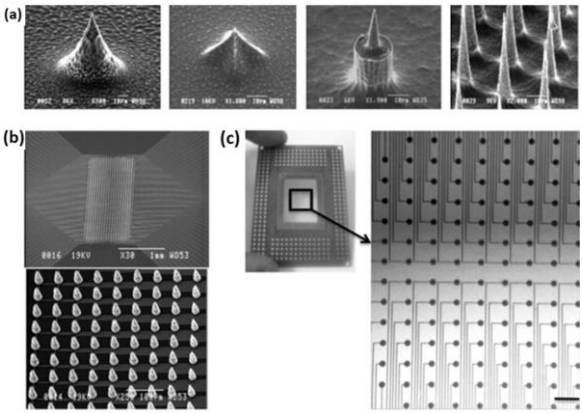

Figure I - 5. Development of high-density arrays of 3D-shaped electrodes. (A) 3D-tip electrodes were fabricated using alternations of isotropic and anisotropic etching approaches. Different shapes were achieved using different etching and mask parameters. (B) Example of a dense 1024-electrode array with 80-µm-high electrodes spaced every 50 µm (in this case, the electrode leads were passing under the micro-needles). (C) The final PCB-mounted transparent electrode array with 256 3D Pt-plated silicon electrodes was reported on a glass substrate. Scale bars: 10 µm in all panels of A, 1 mm in the top panel of B, 100 µm in the bottom panel of B, 300 µm in the right panel of C.[33]

Charvet et al. (2010) substantially contributed by developing a modular 256-channel MEA with integrated electronics [33]. Using isotropic and non-isotropic step etching techniques allows for high electrode aspect ratios and different tip electrode shapes, enhancing the adaptability of 3D MEAs for various applications. Dimaki's work in 2010, focusing on the development of 3D micro- and nanoelectrodes, is noteworthy for its potential implications in extracellular and intracellular studies [34]. The

advantage here lies in the applicability of these electrodes to diverse scenarios, ranging from brain slice recordings to highly localized measurements, suggesting a broader utility of 3D microelectrode arrays in various experimental setups, demonstrating their adaptability to different neural preparations. Goncalves et al. (2015) reported electrodes with different penetration lengths, introducing diversity in the design [35]. This work showed the potential for tailoring 3D-MEAs based on specific experimental needs, providing flexibility in electrode design. However, questions regarding the scalability and practical implementation of such designs persist.

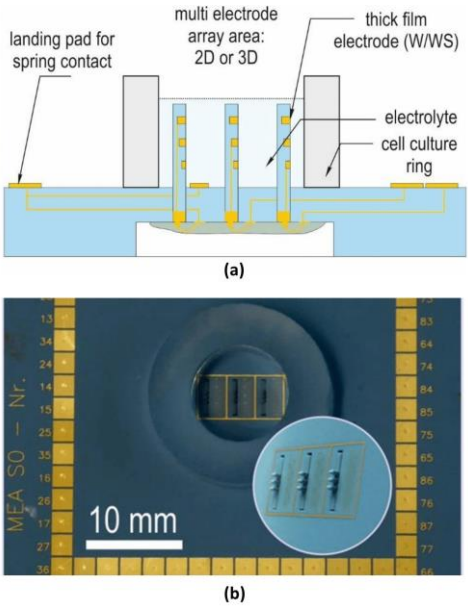

Figure I - 6. Development of 3D MEAs consisting of individually addressed 2-D and 3-D electrodes. (a) Cross-section of the 3D MEA, three miniaturized ceramic circuit boards, assembled perpendicularly through slots of the ceramic base plate. (b) Image of 3D MEA assembly.[36]

Bartsch et al. (2018) brought a distinctive perspective by utilizing a low-temperature cofired ceramic (LTCC) board as the base plate for 3D microelectrodes [36]. This unconventional approach provides an alternative platform for integrating 3D components into standard 2D MEAs. Nonetheless, the challenges in optimizing the coordination between 2D and 3D elements remain.

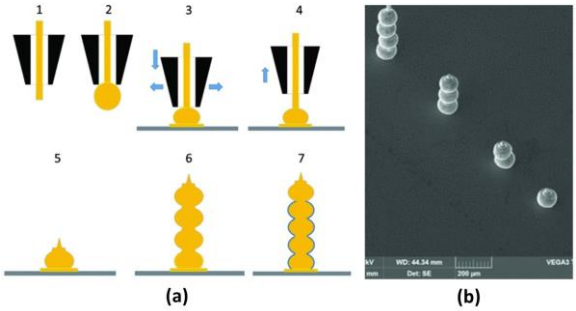

Figure I - 7. Fabrication of vertically stacked beads based 3D MEAs. (a) Process outline (steps 1-7) for fabricating the stacked beads. 1. Capillary tool with Au-wire; 2. Bead formation by high voltage electric charge; 3. Bead bonding on the top of the microelectrode; 4. Capillary tool pulled up; 5. Wire cutting and first bead formation; 6. The procedure is iterated for the formation of stacked beads; 7. The procedure is finalized after the passivation of the staked beads with the Parylene layer and the bonding of the last bead with no passivation. (b) SEM image of vertically stacked beads representing variable height 3D electrodes.[37]

In 2019, Lorenzelli et al. employed a unique ball-bonding technique by stacking gold beads to introduce variable-height 3D electrodes on a standard planar MEA chip [37]. This approach allows for controlled height and uniform distribution of multi-level microelectrodes, offering a nuanced approach to 3D design. This method's potential application and scalability to larger arrays and diverse experimental conditions are open questions.

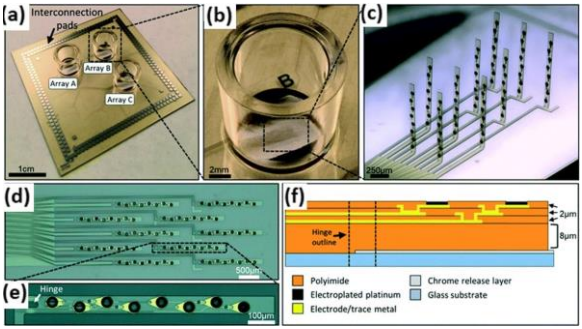

Figure I - 7. Design and development of a flexible 3D MEA. (a) A completed device. The overall length, width, and pad locations are identical to a commercial multichannel systems brand device, allowing for seamless integration into existing electrophysiology electronics. (b) Close-up image of a single cell culture well. The prominent dark metal features at the top and bottom of each cell culture well are ground electrodes, which are all electrically shorted to each other. (c) Light micrograph of a single 3DMEA post-actuation. The hinge regions are plastically deformed, allowing the probes to stand upright without additional support. (d) Brightfield image of one MEA array containing ten probes and 80 electrodes prior to actuation. From left to right, columns containing 2, 3, 2, and 3 probes can be seen, respectively. (e) Detail of one probe containing

eight electrodes, all electroplated with platinum black. The hinge region to the left is plastically deformed during the actuation process. (f) Cross-sectional cartoon showing a material stack of the microfabricated probe and the relative location of the hinge (not to scale).[25]

Soscia et al. (2020) reported a thin film-based, non-invasive, flexible 3D MEA [25]. This novel design features polyamide probes, each containing an array of eight electrode pads. Mechanical actuation to lift arrays vertically introduces a dynamic element into 3D MEAs. The advantages of this approach include non-invasiveness, flexibility, and the ability to record and stimulate neurons at multiple heights in *in vitro* neuronal cultures. However, challenges may arise regarding the scalability and complexity of the mechanical actuation system. Spanu et al. (2020) introduced a straightforward method for fabricating pillar-shaped 3D electrodes exceeding 100 µm in height, suitable for various metal MEAs, whether custom-made or commercially available [38]. The fabrication involved standard photolithography on thick resists combined with gold electroplating, resulting in pillar-shaped structures originating from planar MEA devices. Notably, the electrodes feature flat tips, making them well-suited for delicate tissue interactions. However, this approach is limited to developing 3D MEAs with uniform electrode heights.

Shin's contributions in 2021 take the advancements further by integrating optical stimulation and drug delivery functionalities into 3D high-density microelectrode arrays [26]. This integrated approach introduces new dimensions for investigating the neural circuit dynamics within engineered 3D neural tissues. The significance of this development lies in its ability to monitor and actively modulate neural activity within a 3D neuronal construct, providing a more comprehensive understanding of complex neural networks.

Saleh and colleagues in 2022 presented a novel approach utilizing 3D nanoparticle printing to address existing limitations in electrode design for *in vivo* recordings [39]. This innovative methodology marks a significant advancement, facilitating the first successful *in vivo* recording from electrodes engineered to leverage the flexibility inherent in the 3D printing process. The resulting 3D multi-electrode devices offer several key features, including high electrode densities (2600 channels/cm^2 footprint), minimal tissue damage upon insertion, and exceptional signal-to-noise ratios. Notably, the fabrication process allows for flexible reconfiguration, accommodating variations in individual shank lengths and layouts while maintaining low overall channel impedances. This flexibility is facilitated by the development of custom 3D-printed multilayer circuit boards, representing a notable fabrication advancement with broad potential applications in both *in vivo* and *in vitro* electrophysiological investigations.

Mapelli et al. (2022) introduced a novel fabrication technique capable of producing a chip featuring thousands of microneedles (µneedles) with heights ranging from 60 to 90 µm and widths from 14 to 26 µm, spaced at a pitch of 60 µm [40]. Each needle was accompanied by a larger pedestal at its base, forming a dense matrix of

microchannels beneath the tissue penetrated by the needles, thereby preventing direct contact with the base of the chip. Remarkably, this fabrication process is entirely CMOS compatible, enabling the development of the first high-density Microelectrode Arrays (MEAs). The outcome was a monolithic CMOS high-density MEA incorporating a 64 × 64 μneedle electrode grid with an integrated microfluidic system, ensuring efficient diffusion of oxygen, nutrients, and chemicals to the lower tissue layers. This technology combines penetration capability, high-resolution recording, and enhanced tissue viability in a single device. The system's efficacy was validated by recording spontaneous, chemically modulated, and electrically evoked activity in cerebellar and cortico-hippocampal brain slices.

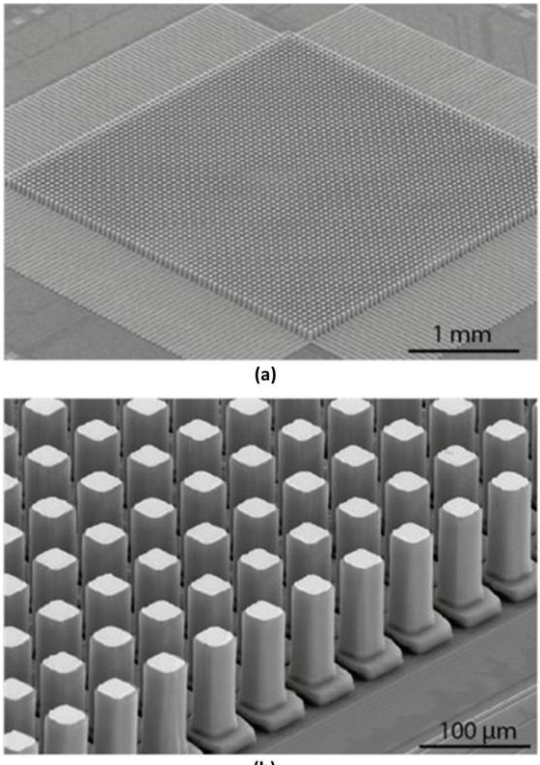

Figure I - 8. Scanning Microscopy Imaging (SEM) showing, (a) overview of the 3D high-density CMOS MEA, (b) a close-up view of the microelectrodes.[40]

Although the CMOS 3D MEA presented in this study [40] offers several advantages over other state-of-the-art 3D MEAs, it is still constrained by a limitation concerning the probing of the 3D neuronal construct in a single plane along the z-

direction. This limitation arises from the uniform height of 3D electrodes, which restricts their ability to access neuronal activity across multiple depth levels within the tissue. As a result, despite the enhanced capabilities of the CMOS 3D MEA, its efficacy in capturing the full complexity of neural networks within three-dimensional structures may be somewhat restricted. Addressing this limitation could potentially involve the development of electrodes with variable heights or other innovative approaches to enable multi-level probing within the 3D neuronal construct. Such advancements would enhance the utility and applicability of CMOS 3D MEA for a broader range of neuroscientific investigations requiring comprehensive spatial sampling capabilities.

I.4 Challenges and opportunities in 3D MEA research

Despite notable strides in 3D microelectrode array research, critical research gaps and limitations have emerged, which demand urgent attention and innovation. Saleh's examination (CMU, 2022) highlights the existing electrode issues, exposing coverage, fragility, and cost shortcomings [39]. These limitations underscore the pressing gaps in electrode design, calling for advancements that extend coverage, enhance durability, and reduce expenses.

Dong's recent findings in 2022 underscore a significant challenge: the weakness of electrical signals from cells, posing a hindrance to the precise measurement of electrophysiological properties[41]. This research gap emphasizes the urgent need to refine the sensitivity and accuracy of microelectrodes to capture and interpret nuanced cellular activities effectively. Kundu A.'s work in 2021 spotlights a concerning aspect of 3D-printed microelectrode arrays—the poor adhesion between the insulative layer and substrate material [42]. This limitation severely restricts their biomedical application, signifying a clear gap in material integration.

Molina-Martínez's research in 2022 emphasizes the critical need for improved integration of electrical recording with other readout modalities in 3D neuronal cultures [43]. This knowledge gap reflects a broader challenge to achieving a more comprehensive understanding of neuronal activity through multimodal measurements.

Spira's influential work from 2013 points to a crucial research gap, the inability of existing microelectrode arrays to capture subthreshold synaptic potentials and membrane oscillations, highlighting a significant limitation in current methodologies and calls for innovative approaches to bridge this gap in understanding neural activity at a finer scale [44].

Du's work in 2009 and Soscia's findings in 2020 converge on the shared need for improved spatial resolution and the ability to simultaneously record from multiple locations within 3D networks of neurons[25,45]. This research gap underscores the need for more sophisticated recording technologies to provide a richer and more detailed understanding of complex neural circuitry.

Revyn's insights in 2022 draw attention to a critical research gap in commercial microelectrode array platforms: their inability to allow 3D spatial recording of neuronal

activity and high-throughput single-unit recordings [46]. This limitation severely hampers the study of neuronal tissues and organoids, highlighting the importance of platforms that can provide comprehensive insights into intricate neural structures.

The collective body of research by Saleh, Dong, Azim N., Molina-Martínez, Spira, Du, Soscia, and Revyn identifies current limitations and illuminates significant research gaps. Addressing these gaps requires advancements in electrode design, signal measurement accuracy, material integration, and recording capabilities, signifying a crucial frontier for future innovations in 3D MEAs. A significant challenge lies in the lack of precise control over the height of the 3D electrodes at an individual level, which is critical for achieving accurate and realistic neural modeling. Additionally, the existing methods are not sufficiently robust to facilitate wafer-scale production, raising concerns about scalability and broader applicability. Furthermore, the compatibility of 3D MEAs with existing experimental platforms remains an issue that hinders seamless integration into established research setups. Another drawback is the poor volumetric distribution of electrodes in the X, Y, and Z dimensions, which restricts the comprehensive coverage required for in-depth electrophysiological investigations. The current state of 3D MEAs also falls short of providing customization options for electrode array topography and configuration, limiting their adaptability to diverse experimental needs. Moreover, concerns about cost-effectiveness add another layer of complexity, necessitating careful evaluation of the practical feasibility of these advanced geometries in the broader landscape of neuroscience research.

Overall, the majority of the 3D MEA device spectrum can be divided into two primary categories based on the electrode design, topography of the electrode arrays, and interactions with tissue cultures. The first category is represented by 3D MEA devices comprising partially passivated protruding-tip-based electrodes [30,31,47] and uniform-height 3D electrode arrays [38,40]. The protruding 3D tip electrodes allow access through surface dead cell layers to the intact cell layer in the brain slice, allowing the detection of more signals compared to conventional 2D type electrodes [29,30]. Protruding tip-based 3D MEAs have numerous advantages over 2D MEAs. However, the constant electrode height is a major limitation, allowing the recording of electrophysiological activities from a single plane in a complex 3D neuronal construct.

This limitation is addressed by the second category of 3D MEA devices, consisting of multiple electrodes on a vertical shank [25,26,45,46] and electrodes with varying heights [35,37,39,48]. This category of 3D MEAs has shown great potential for investigating the electrophysiological activity of 3D neuronal constructs. However, some key concerns must be addressed. 3D MEA devices consisting of multiple electrodes on vertical shanks offer excellent resolution in the Z dimension, often achieved at the cost of lateral resolution owing to complex fabrication approaches [25]. However, variable shank height 3D MEAs stand out because of their unparalleled customizability, allowing researchers to control shank heights precisely. This adaptability is crucial for tailoring studies to diverse neural tissues, achieving improved

spatial resolution, and ensuring precise recording and stimulation. However, these 3D MEAs are mostly fabricated using various 3D printing technologies. The use of 3D printing technology in electrode fabrication, while offering unparalleled design flexibility and the potential for complex geometries, is not without limitations. Veloso et al. (2023) emphasized a key limitation: the impact of the contact resistance on the electrochemical response of 3D-printed electrodes [49]. This challenge stems from the inherent electrical conductivity of the printed material, which debunks the conventional assumption that finite electron transfer is the primary limiting factor. Despite the ability to modulate the contact resistance through the design of 3D-printed electrode geometries, the electrical properties of the printed material persist as a constraint. Additionally, while surface modifications demonstrate promise for enhancing the standard heterogeneous rate constant, intrinsic challenges are tied to the fundamental electrical conductivity of 3D printed materials. These limitations necessitate further exploration to refine the electrode design and improve the electrochemical performance [49].

I.5 Platform for development of variable-height 3D MEA

This thesis presents a new technological platform to develop highly customizable multi-depth probing 3D MEA devices with precisely controlled variable electrode heights. This platform utilizes a multistage bottom-up fabrication approach capable of developing 2D and 3D MEAs and hybrid 3D MEAs capable of probing 3D neuronal constructs on the surface and at multiple depths. This approach utilizes well-established micromachining processes, such as deposition, photolithography, and etching, to develop planar MEAs with customized layouts that define the core of the technology. These planar MEAs are then transformed into 3D MEAs using a template-assisted electrodeposition process. This transformation is achieved using an innovative selective electrodeposition mechanism, allowing control over the electrode heights and array topography, discussed in detail in the third chapter of the thesis.

This technological platform addresses some critical limitations of existing platforms for developing customizable 3D MEAs. The current approach uses electrodeposition to fabricate 3D electrodes, addressing the issues of the printed electrode's contact resistance and poor electrical conductivity. Another key issue addressed is the ability of the reported platform to enable customization at a batch-processing scale. Further research and development on the technology could further enhance its scalability, cost-effectiveness, and customizability.

The proposed technological platform presented in this chapter builds upon the rich heritage of existing MEA technology. As discussed in the next chapter, MEA technology has evolved significantly over the years, driven by a quest to enhance our understanding of neural activity and brain function.

Chapter II: Exploring essential elements of MEA technologies

II.1 Evolution of MEA technology

II.1.1 Overview of planar (2D) MEA technology

Planar MEA technology represents a significant advancement in electrophysiology, serving as a crucial instrument for understanding the behavior of neuronal networks. The fundamental principle underlying MEA technology involves the arrangement of multiple microelectrodes on a shared substrate, enabling the simultaneous recording or stimulation of neuronal activity from various locations [50]. Traditional MEAs, commonly called planar MEAs, typically consist of biocompatible substrates (such as glass or silicon) onto which metal (such as gold or platinum) or conductive polymer electrodes are patterned. These microelectrodes were connected to an electronic interface that amplified and digitized the recorded signals for further analysis.

In 1972, Thomas et al. demonstrated the first functional planar or 2-dimensional (2D) MEA [51]. The device consisted of two rows of platinized gold electrodes (15 electrodes in each row), separated by a distance of 100 µm on a glass substrate and passivated with a photoresist. Although proficient in recording field potentials from spontaneously contracting sheets of cultured chick cardiomyocytes, this early MEA design fell short of capturing single-cell activity. Subsequently, Gross et al. merged photolithography and laser etching techniques, resulting in a high-density MEA capable of recording electrical activity from over 30 neurons dissociated from the snail ganglia [52]. The groundbreaking achievement of a single recording from a network of rat superior cervical ganglion neurons cultured for up to three weeks occurred in 1980 when Pine utilized a 2D MEA with 32 platinized gold electrodes insulated by silicon dioxide [53]. The concept of fabricating rigid electrodes directly on a glass substrate, where the 2D MEA features gold electrodes with platinum black-coated tips, was initially proposed by Novak and Wheeler in 1988 [54].

During the early 1990s, progress in complementary metal–oxide–semiconductor (CMOS) technology played a pivotal role in significantly advancing MEA technology. Integrating CMOS and MEA technologies has led to more precise and accurate high-density MEAs. These CMOS-based MEAs enable measurements with superior spatial and temporal resolutions, overcoming certain limitations associated with passive MEAs. Over the years, various high-density microelectrode arrays (HD-MEAs) have employed post-processing techniques to manufacture electrodes onto embedded CMOS electronics [55]. A notable milestone occurred in 2007 when Frey et al. introduced a device featuring reconfigurable electrode/readout-channel routing [56]. The novel device included 11,011 metal electrodes and 126

channels with reconfigurable routing, allowing each electrode to perform simultaneous stimulation and electrophysiological recordings of neurons.

It is imperative to augment electrode density to enhance the comprehension of signal propagation within neural networks. With this objective, Berdondini et al. pioneered the development of a CMOS-based solid-state Active Pixel Sensor (APS) array in 2009 [57]. The apparatus comprised 4096 pixels, organized in a 64 × 64 MEA, facilitating micro- and macro-circuitry electrophysiological recordings within *in vitro* neuronal preparations. Subsequently, in 2014, Ballini et al. demonstrated a remarkably high-resolution CMOS-based MEA device designed for scrutinizing electrophysiological activities at the subcellular, cellular, and network levels. This innovative device featured a rapidly reconfigurable array of 26,400 microelectrodes crafted using narrow-pitch lithography [58].

Planar MEAs have been instrumental in studying neuronal cultures and offer several advantages over classical single-cell electrophysiological methods. First, they allow for noninvasive, long-term monitoring of neuronal activity, enabling the study of network development and dynamics over time. Second, they provide simultaneous multi-site recordings, capture the spatiotemporal patterns of neuronal activity, and reveal the underlying network structure [59]. Planar MEAs have found widespread applications beyond basic research. They have been used to create *in vitro* models of neurological diseases, assess the neurotoxic effects of drugs, and investigate the bioelectric behavior of other cell types, such as cardiomyocytes [60,61].

II.1.2 Limitations of planar arrays for 3D neuronal cultures

Despite the significant contributions of planar MEAs to neuroscience, they have inherent limitations when studying three-dimensional (3D) neuronal cultures. A primary constraint is the 2D design of planar MEAs, which restricts recording and stimulation to the bottom layer of cells in 3D cultures [32]. This limitation overlooks the intricate depth-dependent dynamics within 3D neuronal networks, providing a limited view of overall network activity [6].

Furthermore, the spatial resolution of planar MEAs is constrained by the electrode pitch, typically tens to hundreds of micrometers. This constraint limits the ability of MEAs to capture fine spatial patterns of activity within dense 3D neuronal cultures [44]. Another key limitation concerns the mechanical mismatch between the rigid planar MEA substrate and the soft 3D neuronal culture. This mismatch can strain and potentially damage the culture, affecting its health and function [62].

Although planar MEAs have been instrumental in advancing our understanding of neuronal networks, their limitations concerning 3D neuronal cultures necessitate the development of more advanced recording technologies. The advent of 3D MEAs represents a promising strategy towards this goal, offering the potential to explore depth-dependent dynamics in 3D neuronal cultures.

II.2 Advantages and Challenges of 3D MEAs

II.2.1 Enhanced neuronal morphology and connectivity

The emergence of 3D MEAs marks a significant leap in electrophysiology, addressing the limitations associated with planar MEAs and bridging the gap between *in vitro* and *in vivo* models of neuronal activity [63]. One of the key advantages of 3D MEAs is their ability to accommodate the natural 3D morphology and connectivity of neurons, thereby providing a more accurate reflection of the *in vivo* neural environment [64].

Neurons in 3D cultures display more realistic axonal and dendritic arborization patterns than 2D cultures [65]. This complex morphology, coupled with the fact that 3D cultures allow neurons to form connections in all directions, leads to a network topology that closely mimics actual brain tissue [10].

3D MEAs can capture this enhanced connectivity with their ability to record data from multiple points within a 3D culture. They provide a unique tool to study the spatial and temporal patterns of neuronal activity across the depth of a 3D network, thereby enriching our understanding of neuronal communication and function [66].

II.2.2 Physiologically relevant microenvironments

3D MEAs also take advantage of physiologically relevant microenvironments created by 3D neuronal cultures. These environments include the extracellular matrix and cellular components that mimic the *in vivo* brain environment, providing essential biochemical and biophysical cues for neuronal growth and function [67].

3D MEAs within such environments provide a more holistic view of the neuronal responses to these cues. For instance, they can be used to investigate how neurons respond to gradients of signaling molecules or the mechanical properties of the extracellular matrix, thereby shedding light on the complex interplay between neurons and their microenvironment [68].

II.2.3 Challenges in 3D MEA fabrication and integration

Despite the significant advantages of 3D MEAs, their fabrication and integration into 3D neuronal cultures pose substantial challenges [6]. The fabrication of 3D MEAs requires sophisticated manufacturing techniques to create a 3D electrode structure and to ensure biocompatibility.

The challenges in 3D multi-electrode array fabrication include customization to address specific experimental or clinical needs, limitations in coverage, fragility, and expense of current electrodes, and the complexity of surface electrode design with low-parasitic and high-density interconnection requirements. Other challenges include high alignment accuracy and reproducibility when assembling heterogeneous chips of different sizes and thicknesses. Additionally, there is a need for flexible reconfiguration

of electrode layouts, different individual shank lengths and layouts, and low overall channel impedances [39]. The fabrication of 3D multielectrode devices also requires the development of custom 3D-printed multilayer circuit boards to support the integration of high-density electrodes. Overall, the challenges in 3D multi-electrode array fabrication revolve around achieving customization, robustness, high alignment accuracy, and low impedance.

Integration of 3D MEAs with 3D neuronal cultures is a key challenge. The electrode array must be carefully inserted into the culture medium without causing significant mechanical disruption. Moreover, maintaining cell health and viability within the 3D culture, particularly in regions close to the electrodes, is crucial for reliable electrophysiological recording [29]. Another challenge lies in the interpretation of the data obtained from 3D MEAs. The complex 3D structure of the recorded network makes it difficult to accurately assign recorded signals to specific neurons or locations within the culture [57].

While 3D MEAs offer significant advantages for studying neuronal networks, their widespread adoption in neuroscience research requires further effort to overcome the technical challenges associated with their fabrication, integration, and data interpretation.

II.3 Design considerations for 3D MEAs

II.3.1 Electrode design, configuration, and density

Electrode design plays a crucial role in the performance of 3D MEAs, and an ideal electrode should have several key characteristics. The electrode should be highly sensitive to detect low-level neural signals with high fidelity. It should also minimize the electrical noise to ensure clean and reliable signal recording. Additionally, the electrode should maintain a stable impedance over time to avoid signal distortion and ensure a long-term recording capability. The electrode material and surface chemistry should be biocompatible and non-toxic to avoid harming neurons. Finally, the electrode should be mechanically stable and not prone to deformation or breakage in the complex microenvironment of the 3D cultures.

Electrode configuration and density are critical parameters in the design of 3D MEAs. They directly influence the spatial resolution and coverage of neuronal activity that can be recorded and, thus, the level of detail and accuracy in the data collected. In conventional 2D MEAs, electrodes are typically arranged in a planar grid [57]. However, in 3D MEAs, electrodes can be strategically distributed in three dimensions to maximize coverage within the volume of 3D culture. This approach improves the spatial resolution of recordings and enables the capture of depth-dependent characteristics of neuronal activity [25].

The electrode density, or number of electrodes per unit volume, also plays a critical role in determining the spatial resolution of the array. Higher electrode densities

can provide finer spatial resolution, allowing the detection of signals from individual neurons within a 3D network [29]. However, the increased complexity associated with higher densities can lead to signal processing and data management challenges.

II.3.2 Biocompatible substrates and materials

The choice of biocompatible substrates and materials is crucial for designing 3D MEAs to ensure they do not elicit adverse cellular responses. The materials used for the substrates and electrodes should be conductive, durable, and biocompatible. Negar Geramifard et al. have designed a helical 3D MEA using polyimide, amorphous silicon carbide, gold/titanium, and sputtered iridium oxide films [69]. Lisa Mapelli et al. have developed a CMOS high-density (HD) MEA with microneedles that can penetrate and record in-tissue signals, providing a 3D HD-MEA chip [40]. Kundu et al. used cost-effective makerspace microfabrication techniques to fabricate 3D MEAs with 3D printed base structures and metallization of micro towers and conductive traces [42]. Glass substrates have also been used because of their biocompatibility, chemical resistance, and optical transparency [70]. Yo Han Cho et al. discuss using 3D bioelectrodes to optimize the transfer of signals at tissue-electrode interfaces [71].

The use of silicon, gold, and platinum as electrode materials has been well-established because of their excellent conductivity and biocompatibility [72]. However, these materials may not ideally match the mechanical properties of soft neural tissues [73]. A platinum-elastomer composite was developed to address this mismatch, offering mechanical compliance and electrochemical properties [72]. Organic coatings, such as conductive polymers and carbon nanotubes, have also been explored to improve charge transfer and reduce mechanical mismatch with neural tissues [73]. Despite these advancements, challenges remain in optimizing these materials' electrical, mechanical, chemical, and biological properties to achieve long-term performance [74]. Further research is needed to address these challenges and develop more effective neural interface electrodes [75].

Recent advances in materials science have led to the development of novel materials with superior biocompatibility and mechanical flexibilities. Kaur et al. (2015) and Huang et al. (2019) highlighted the potential of conductive polymer composites comprising biostable/biocompatible polymers and conductive fillers, such as graphene, carbon nanotubes, and metallic nanoparticles [76,77]. These composites have shown promise for various biomedical applications, including biosensors, drug delivery systems, and tissue engineering. Zhou et al. (2023) discussed the utility of flexible and stretchable carbon-based sensors and actuators in soft robotics, emphasizing their biocompatibility, portability, and power efficiency [78]. Barreiro et al. (2019) further explore the use of biobased carbon materials in fabricating conductive silk-based composites, which are highly stretchable, flexible, and biocompatible [79].

II.3.3 Spatial and temporal resolution optimization

Spatial and temporal resolutions are crucial for recording electrophysiological activity in 3D MEA arrays. Spatial resolution refers to the ability to spatially discriminate between different neuronal sources, whereas temporal resolution is the ability to capture neural activity dynamics accurately. Research has shown that electrode size and shape significantly influence spatial resolution in extracellular recordings. Smaller and more precisely shaped electrodes can be recorded from smaller neuronal populations or individual neurons [80]. This approach is essential for high-density intracortical recording, where nanofabricated ultra-flexible electrode arrays have been shown to overcome physical limitations and achieve a high signal-to-noise ratio [81]. However, there is a trade-off between electrode size and recording characteristics, with an optimum size of approximately 20 × 20 µm for improved selectivity [82]. High-density arrays of 3D microneedle electrodes have been proposed to evaluate the spatial resolution of neuronal activity, with the spatial resolution of spike signals found to be smaller than the electrode interval [83].

On the other hand, the temporal resolution is determined by the sampling rate of the recording system. Higher sampling rates allow for the capture of more rapid changes in neuronal activity. However, higher sampling rates also lead to larger datasets and increased computational demands for data analyses [84]. Optimizing the spatial and temporal resolution is crucial for obtaining high-quality recordings that accurately reflect the complex dynamics of neuronal activity in 3D cultures [85]. However, trade-offs among resolution, complexity, and data management must be carefully considered when designing 3D MEAs.

II.4 Fabrication techniques for 3D MEAs

II.4.1 Photolithography-based approaches

Photolithography has been a staple in microfabrication since its inception and is indifferent to the fabrication of 3D MEAs. This process involves using light to transfer a geometric pattern from a photomask to a light-sensitive chemical or a photoresist on a substrate. After exposure, the photoresist undergoes a development process that removes the exposed or unexposed regions depending on the type of photoresist used. This process forms a patterned structure, which can then be used as a template for further processing, such as the deposition or etching of the electrode materials.

Photolithography, while effective for high-resolution patterning, can be time-consuming and costly because of the need for iterative mask development [86]. However, alternative methods, such as LCD stereolithographic 3D printing and liquid deposition photolithography, offer rapid and cost-effective fabrication of complex 3D microstructures [87,88]. Another approach involves using a flexible elastomeric photomask and near-field subdiffraction photolithography, further enhancing the

resolution and cost efficiency [89]. These advancements in fabrication techniques provide viable alternatives to traditional photolithography processes, thereby addressing their limitations.

II.4.2 Micromolding and soft lithography techniques

Micromolding and soft lithography techniques have also been extensively employed to fabricate 3D MEAs. These methods involve using a mold or template to shape a material into a desired structure [90]. In soft lithography techniques, the template is generated using a flexible material such as polydimethylsiloxane (PDMS), which can be peeled off from the cast structure without causing damage. These techniques offer advantages such as cost-effectiveness and ease of fabrication. They can also be used with various materials, including biocompatible polymers and hydrogels, and are particularly suitable for 3D MEA applications.

Various soft lithography techniques have been used to develop 3D MEAs for electrophysiological investigation. Yadav et al. (2021) introduced a multi-level 3D MEA with gold micro-pillars, while Morales-Carvajal et al. (2020) demonstrated a stainless steel 3D MEA on a glass substrate for simultaneous optical and electrical probing [47,91]. Didier et al. (2020) presented compact 3D MEAs with monolithically defined features, and Rajaraman et al. (2007) reported successful electrical characterization and electrophysiological recordings from brain slices using metal transfer micro molded 3D MEAs [31,92]. These studies highlight the potential of soft lithography techniques for advancing the 3D MEA technology for electrophysiological investigations.

II.4.3 3D Printing and additive manufacturing methods

3D printing, or additive manufacturing, is a relatively recent development in fabrication technology that has shown great potential for 3D MEA fabrication. This process involves the layer-by-layer deposition of the material to create a 3D structure guided by a digital model. Different 3D printing techniques, such as stereolithography (SLA), fused deposition modeling (FDM), and selective laser sintering (SLS), can be used depending on the material and resolution requirements [39,93]. With the development of conductive inks and filaments, 3D printing tools can fabricate substrates and electrodes for 3D MEAs [94].

Recent advancements in 3D printing technology have shown promise for addressing the challenges of achieving high resolution and precision in the fabrication of MEAs. Grob et al. (2019) and Kundu et al. (2020) demonstrated the feasibility of fabricating high-resolution 3D MEAs using electrohydrodynamic inkjet printing and microstereolithography (μSLA)-based 3D printing [95,96]. These methods allow for tuning the electrode dimensions and integrating all components of the MEA platform to realize high-throughput, self-insulated 3D MEAs. An et al. (2015) further highlighted

the potential of electrohydrodynamic inkjet printing in creating high-resolution complex 3D structures with multiple functional inks, which could be applied to fabricating MEA electrodes [97]. These studies underscore the potential of 3D printing to overcome the challenges of high resolution and precision in MEA electrode fabrication.

The fabrication of 3D MEAs has come a long way away, with various techniques being developed and refined to achieve the desired design and performance characteristics. Photolithography, micro-molding, and soft lithography have proven to be effective methods for fabricating these devices, whereas 3D printing offers exciting new possibilities. However, achieving the required electrode conductivity and biocompatibility remains challenging [49].

II.5 Electrode materials for 3D arrays

II.5.1 Metal electrodes: advantages and challenges

Metal electrodes have long been used in traditional MEAs and are widely employed in 3D MEAs. Materials such as gold, platinum, and titanium offer excellent electrical conductivity and biocompatibility, making them suitable for recording and stimulating neuronal activity [98]. Metal electrodes provide reliable and stable electrical contact with neurons, thus enabling high-quality signal recording. They exhibit low impedance, which facilitates the detection of weak neural signals and reduces noise interference. In addition, metal electrodes are relatively easy to fabricate and integrate into 3D MEAs.

However, metal electrodes have limitations. They are rigid and lack mechanical flexibility. This lack of flexibility may strain delicate 3D neuronal cultures and affect their function and viability. Furthermore, metal electrodes can induce corrosion over time, leading to the degradation of electrode performance and potential toxicity to the surrounding tissue. Despite these limitations, 3D MEAs have been successfully designed and utilized for recording and stimulating neuronal activity, with the potential to monitor neural network activity in all three dimensions [32,42]. These advancements in 3D MEAs offer promising solutions to the challenges posed by using metals as electrode materials. Efforts are being made to address these challenges; nanostructuration techniques have been explored to enhance the performance of MEAs, including using carbon nanotubes and conducting polymers [99].

II.5.2 Carbon-based electrodes: Graphene, Carbon Nanotubes, and Diamond

Carbon-based electrodes, including graphene, carbon nanotubes (CNTs), and diamond, have recently gained significant attention because of their unique properties and potential applications in 3D MEAs.

Graphene, a single layer of carbon atoms arranged in a hexagonal lattice, offers exceptional electrical conductivity, high mechanical strength, and chemical stability

[100]. They can be integrated into 3D MEAs as standalone electrodes or as coatings on other materials. Graphene electrodes have demonstrated superior sensitivity and signal-to-noise ratios in neuronal recordings, providing promising prospects for high-resolution electrophysiological studies [101].

Carbon nanotubes – cylindrical structures composed of rolled-up graphene sheets –also possess excellent electrical properties and mechanical flexibility [102]. Carbon nanotubes can be functionalized and aligned to create 3D networks, allowing for improved electrode-neuron interfacing and enhanced signal detection [103].

Diamond electrodes, made of synthetic diamond, exhibit a unique combination of properties, including high electrical conductivity, chemical inertness, biocompatibility, and low background noise. They offer long-term stability and durability in harsh environments, making them suitable for application in 3D MEAs [104].

II.5.3 Conducting polymer electrodes: PEDOT, PPy, and PANI

Conducting polymers have emerged as promising electrode materials for 3D MEAs owing to their unique combination of electrical conductivity, mechanical flexibility, and biocompatibility. Poly(3,4-ethylenedioxythiophene) (PEDOT), polypyrrole (PPy), and polyaniline (PANI) are conducting polymers widely used in neuroelectrodes [105]. These polymers can be electrodeposited or spin-coated onto electrode surfaces, providing a conformal and uniform coating that promotes close contact with the neurons.

Polymer electrodes offer several advantages, including enhanced electrode-neuron interfacing, reduced impedance, and improved long-term stability compared to metal electrodes [106]. They can also be functionalized with bioactive molecules to modulate neuronal adhesion, growth, and signaling. However, conducting polymer electrodes face challenges related to their stability and performance over time. Oxidative degradation, loss of conductivity, and potential toxicity are among the concerns that must be addressed to ensure a reliable and safe long-term operation.

II.5.4 Nanomaterial-based electrodes: Nanowires, Nanotubes, and Nanoparticles

Nanomaterials such as nanowires, nanotubes, and nanoparticles offer unique properties and functionalities that make them attractive candidates for 3D MEAs [107].

The high aspect ratio and small dimensions of nanowires enhance their sensitivity and spatial resolution in recording neuronal activity [63]. They can be fabricated from various materials, including silicon, metal oxides, and conductive polymers, and can be integrated into 3D MEAs to probe neuronal networks at the subcellular level.

Carbon nanotubes, mentioned earlier as carbon-based electrodes, also fall into the category of nanomaterials. Their high electrical conductivity, mechanical flexibility, and biocompatibility make them suitable for 3D MEAs. In addition to their use as electrodes, carbon nanotubes can serve as substrates for neuronal growth and guidance, promoting neuronal network formation [108].

Nanoparticles, such as gold nanoparticles or quantum dots, can be functionalized and coated onto electrode surfaces to enhance electrode-neuron interfacing and signal detection [109]. They offer the potential for enhanced biocompatibility, increased signal amplification, and the controlled release of bioactive molecules.

Although nanomaterial-based electrodes hold great promise, challenges remain regarding scalability, reproducibility, and long-term stability. Further research is needed to optimize the fabrication techniques, biocompatibility, and integration into 3D MEAs.

II.6 Integration and interface electronics

II.6.1 Readout circuitry: Amplification and signal conditioning

Effective integration of the readout circuitry is essential for accurate and reliable recording of neuronal activity using 3D MEA. The readout circuitry performs critical functions, such as amplification and signal conditioning, to ensure an optimal signal-to-noise ratio and fidelity in the recorded neural signals.

Amplification is necessary to enhance the weak electrical signals generated by neurons and overcome noise sources within the recording system. A neural amplifier is tasked with refining the neural waveforms by eliminating DC offsets and enhancing the amplitude of the resulting signal. For optimal signal quality, this amplifier must generate ample gain, filter within the appropriate bandwidth, exhibit a high signal-to-noise ratio (SNR) with superior linearity, and possess high common mode and power supply rejection ratios (CMRR and PSRR). Typically, the background noise at the electrode-tissue interface is around 10 μVrms or less, setting the foundation for practical neural signal recording. Successful neural amplifiers capable of extracting *in vivo* action potentials typically have an input-referred noise value below 3–7 μVrms [110]. Without maintaining this controlled noise level, the signal risks being overwhelmed by surrounding noise.

The action potential reaches 100 mV range at the neural cell membrane level but diminishes rapidly at a short distance from the cell surface. Hence, a gain in the range of 40 dB was considered the minimum necessary. Action potentials exhibit valuable frequency content between 100 Hz to 10 kHz, with signal amplitudes reaching the single-digit microvolt range [111]. Stimulation studies have revealed that various factors play a significant role, with signal characteristics being influenced by both physiological factors and aspects, such as electrode geometry (Krasteva et al., 2002),

composition of the target neural tissue, and electrode impedance (Bharucha et al., 2014) [110,112]. Managing external and internal noise sources and power supply noise is crucial for ensuring accurate signal representation.

Signal conditioning encompasses several processing steps, such as filtering, impedance matching, and artifact rejection, to enhance the quality and integrity of recorded neural signals. Liu et al. (2018) proposed an event-driven processing method aimed at efficient spike sorting, achieving comparable accuracy with lower hardware resources [113]. Novellino et al. (2009) also introduced the Neural Signal Manager, a software package designed for multi-channel spike train analysis incorporating burst detection and statistical algorithms [114]. Filtering techniques, including high-pass, low-pass, or band-pass filtering, can eliminate noise and unwanted frequency components from the signal. Impedance-matching techniques optimize the electrode and recording system coupling, ensuring efficient signal transfer while minimizing distortion. Utilization of artifact rejection techniques, as suggested by Lewicki et al. (1998), aids in identifying and eliminating artifacts induced by stimulation or electrical interference [115].

II.6.2 Data acquisition and processing

Efficient data acquisition and processing are critical components in integrating 3D MEAs. The large number of recording channels and high data rates associated with 3D MEAs require robust and scalable data acquisition systems [116]. Data acquisition systems typically consist of analog-to-digital converters (ADCs) that digitize analog neural signals, allowing for subsequent digital signal processing and analysis. High-speed ADCs with appropriate resolution and sampling rates are required to capture the rapid dynamics of neuronal activity.

Signal processing algorithms extract meaningful information from recorded neural signals. These algorithms include spike detection and sorting, event detection, feature extraction, and pattern-recognition techniques. Efficient processing algorithms enable the identification of neural activity patterns, the analysis of network dynamics, and the extraction of relevant information from large datasets [117].

II.7 Approaches for cell loading in 3D arrays

II.7.1 Spontaneous cell aggregation techniques

Spontaneous cell aggregation techniques aim to promote the self-assembly of cells into 3D structures within the MEAs. These methods leverage the inherent cell-cell interactions and adhesive properties of cells to drive their clustering and organization. Various techniques have been developed to facilitate the autonomous organization of cells into three-dimensional (3D) structures within MEAs. Highlighting the potential applications of these methods, Eke et al. (2022) and Gallego-Perez et al. (2010) emphasized their relevance in regenerative medicine and drug discovery,

respectively [118,119]. In particular, Eke et al. (2022) highlighted the importance of controlled architecture and heterogeneity in steering cell differentiation and proliferation. Using specific methodologies, Napolitano et al. (2007) introduced a scaffold-free approach using micromolded non-adhesive hydrogels, while Brisson et al. (2002) demonstrated the creation of two-dimensional cellular arrays through electrophoretic deposition [120,121].

The hanging drop method, a widely employed technique in cell culture, has seen recent advancements at the microscale, resulting in a more user-friendly platform [122]. This method, known for its simplicity and reproducibility, has proven valuable in generating multicellular tumor spheroids [123]. Additionally, it has demonstrated success in stem cell differentiation and cytotoxicity studies, offering a cost-effective and efficient alternative [124]. Furthermore, the hanging drop method has been applied in the three-dimensional cultivation of germ cell cancer cell lines, serving as a valuable tool for studying cancer cell biology [125]. The hanging drop method utilizes tiny droplets containing cells suspended upside down from the lid of the culture dish. Owing to gravity, the cells settle at the bottom of the droplet, forming 3D aggregates. These aggregates can then be transferred onto the MEA surface for culture and recording.

Various studies have explored the utilization of microwells and micropatterned substrates to regulate the size and arrangement of cell aggregates. Tekin et al. (2010) devised stimuli-responsive microwells capable of thermal regulation to facilitate the retrieval of cell aggregates, rendering them adaptable for diverse applications [126]. Selimović et al. (2011) introduced a fast and cost-effective method for crafting microwells through laser ablation, showcasing their potential for high-throughput analysis of cell behavior[127]. Forget et al. (2017) proposed a swift fabrication technique for functionalized PDMS microwells that promotes the formation of insulin-producing cell aggregates and provides a platform for screening biological factors [128]. Ochsner et al. (2007) engineered micro-well arrays that afford 3D shape control for individual cells, expanding the toolkit available for fundamental biological studies and high-throughput cell screening assays [129].

Spontaneous cell aggregation techniques offer simplicity and versatility, enabling the formation of complex neuronal networks in 3D MEAs. However, they often lack control over individual cells' precise positioning and organization within aggregates.

II.7.2 Scaffold-based methods: Hydrogels and biodegradable scaffolds

Scaffold-based methods involve physical frameworks or support structures that guide cell growth and organization within 3D MEA arrays. Hydrogels and

biodegradable scaffolds are commonly used as scaffold materials because of their biocompatibility and ability to mimic the extracellular matrix (ECM).

Hydrogels are three-dimensional networks of crosslinked hydrophilic polymers that absorb and retain large amounts of water [130]. They provide a hydrated and biologically friendly environment for cell growth and offer tunable mechanical properties and degradation rates. On the other hand, biodegradable scaffolds are typically fabricated from natural or synthetic materials that can be degraded over time by enzymatic or chemical processes [131]. These scaffolds can provide structural support during cell culture and then gradually degrade, allowing cells to replace the scaffold material with their ECM.

Scaffold-based methods offer enhanced control over cell positioning, organization, and network formation within 3D MEA arrays. Cell behavior and differentiation can be modulated by incorporating specific biochemical cues, such as growth factors or adhesion molecules, into the scaffolds.

II.7.3 Bioprinting techniques for precise cell placement

Bioprinting techniques have emerged as powerful tools for precise and controlled cell placement within 3D MEAs. Bioprinting enables layer-by-layer deposition of cells, biomaterials, and other bioactive components to create complex 3D structures [132]. Bioprinting enables the incorporation of multiple cell types, such as neurons, astrocytes, and supporting cells, in a spatially defined manner to mimic the cellular complexity of native tissues. It also offers the potential to create patient-specific models using cells derived from individuals with specific diseases or genetic backgrounds. However, challenges remain in obtaining appropriate bio-ink formulations, ensuring high cell viability and functionality after printing, and optimizing the integration of printed structures with MEA platforms.

II.7.4 Cell encapsulation strategies: Microcapsules and hydrogel beads

Cell encapsulation strategies involve confining individual cells or cell clusters within protective microcapsules or hydrogel beads [133]. These encapsulation structures provide a controlled microenvironment for cells, protecting them from mechanical- and immune-related stresses. Microcapsules are typically spherical structures composed of biocompatible polymers, such as alginate or agarose, which can be easily fabricated using droplet-based techniques [134]. These capsules allow for the encapsulation of single cells or small aggregates and provide a physical barrier that isolates cells from the surrounding environment.

Hydrogel beads, such as those made from alginate or hyaluronic acid, are promising for cell encapsulation in tissue engineering and regenerative medicine [135,136]. These beads provide a supportive matrix for cells, allowing nutrient and

oxygen diffusion to support cell viability [137]. Using sacrificial porogens such as gelatin beads can further enhance the porosity and permeability of the hydrogel, leading to improved cell proliferation and function [135]. Microfluidic channels made from cell-laden hydrogels, such as agarose, can also facilitate the exchange of nutrients and waste products, thereby maintaining cell viability [138].

Cell encapsulation strategies offer advantages in terms of cell protection, uniform distribution, and controlled cell-cell interactions within 3D MEA arrays. They also facilitate the isolation and retrieval of specific cells for downstream analysis.

II.8 Recording electrophysiological activities in 3D arrays

II.8.1 Signal-to-noise ratio optimization

Recording electrophysiological activities in 3D MEAs requires careful signal-to-noise ratio (SNR) optimization. The SNR is a critical factor in the accurate detection and analysis of neural signals and is influenced by several factors, including electrode design, amplifier characteristics, and noise sources.

Electrode designs with reduced noise and improved signal detection capabilities are employed to optimize SNR, including minimizing the electrode impedance and noise contributions from the electrode materials and optimizing the electrode size, shape, and spacing to ensure optimal electrode-neuron interfacing [139,140]. Additionally, electrode configurations, such as multi-site electrodes and high-density arrays, can provide spatially distributed recordings to improve the SNR [107].

The significance of amplifiers in enhancing the SNR in neural recording applications has been well established in the literature. Lee et al. (2017) contributed to this field by developing a neural recording amplifier with adaptive configuration changes designed to optimize SNR in dynamic environments [85]. To address the importance of minimizing noise contributions, Ruiz-Amaya et al. (2010) emphasized the use of low-noise amplifiers with high common-mode rejection ratios (CMRR) [141]. Additionally, signal conditioning techniques, including filtering, grounding, and shielding, have been implemented to further enhance the SNR [142]. In the realm of wideband amplifiers, Taghavi et al. (2012) demonstrated the simultaneous optimization of SNR and jitter, showing that these parameters can be fine-tuned at the expense of the bandwidth [143].

II.8.2 Electrode-tissue interface: Impedance matching and biofunctionalization

The electrode-tissue interface is critical for recording electrophysiological activity in 3D MEA arrays. Achieving a low-impedance interface between the

electrodes and the surrounding tissue is essential for maximizing signal quality and minimizing signal distortion [144]. Impedance-matching techniques reduce the impedance mismatch between the electrode and tissue, including modifying the electrode geometry, using conductive coatings, or incorporating impedance-matching elements in the electrode design [106].

Another critical aspect of the electrode-tissue interface is the biofunctionalization of the electrode surface. Surface modifications with bioactive molecules such as adhesion peptides can promote cell attachment, enhance neuronal network formation, and improve signal quality. Functionalization can also involve using biomimetic coatings or extracellular matrix components to create a more favorable environment for cell adhesion and growth [145].

II.8.3 Stimulation modalities: Electrical and optogenetic

In addition to recording electrophysiological activity, 3D MEAs enable the stimulation of neuronal networks to investigate their functional properties. Electrical and optogenetic stimulation modalities are commonly employed in 3D MEA systems.

Electrical stimulation involves the application of controlled electrical currents or pulses to induce neuronal response. This can be achieved by integrating the stimulation electrodes within the array. Electrical stimulation can be used to study network connectivity, synaptic plasticity, and the effects of external stimuli on neuronal activity [146].

Optogenetic stimulation utilizes light-sensitive proteins such as channelrhodopsins to modulate neuronal activity with high spatial and temporal precision [147]. Light can be delivered to specific regions of a 3D MEA array using optically transparent materials or fiber optic systems. Optogenetic stimulation allows for precise control over the activation and inhibition of specific neuronal populations, offering insights into neural circuitry and behavior.

II.8.4 Recording modalities: Extracellular and intracellular Approaches

Electrophysiological activities in 3D MEA arrays can involve extracellular or intracellular recording modalities depending on the desired spatial and temporal resolution levels. Extracellular recordings involve using microelectrodes to measure the electrical signals generated by neurons in the extracellular space. This approach provides a noninvasive and high-throughput method for simultaneously monitoring multiple neurons' spiking activity and network dynamics [117]. Extracellular recordings can provide insights into the network behavior and communication patterns within 3D neuronal cultures.

On the other hand, intracellular recordings involve the insertion of microelectrodes into individual neurons to measure their membrane potential and

intracellular activity directly. Intracellular recordings offer higher-resolution information on individual neuron properties, such as membrane potential changes, action potentials, and synaptic potentials [148]. However, intracellular recordings are more invasive and generally allow simultaneous recording of fewer neurons.

II.9 Applications of 3D microelectrode arrays

II.9.1 Drug screening and toxicity testing

Recent advances in pharmacology have introduced 3D MEAs as influential tools for drug screening and toxicity testing. These arrays facilitate the evaluation of drug effects in 3D neuronal cultures, offering more physiologically relevant models than traditional 2D cell cultures. By recording electrophysiological activities in 3D MEA arrays, researchers can assess the functional responses of neuronal networks to various drug treatments and examine changes in network connectivity, synaptic transmission, and neuronal excitability in the presence of different drug compounds.

Moreover, 3D MEA arrays allow long-term monitoring of drug effects, enabling the assessment of chronic drug exposure and exploration of drug-induced changes in network dynamics over time. These capabilities provide valuable insights into pharmaceutical compounds' efficacy, toxicity, and potential side effects. Various studies have demonstrated the versatility of 3D MEAs, showcasing developments such as thin films, 3D flexible MEA accommodating 256 channels of recording or stimulation [25], microfluidic MEA platforms for spatially localized drug delivery and electrical recordings of primary neuronal cultures [149], and 3D MEA for recording dissociated neuronal cultures [32]. Additionally, the functional characterization of human pluripotent stem cell-derived models of the brain with MEAs has indicated their potential as valid disease models [150].

II.9.2 Disease modeling: Neurodegenerative disorders, epilepsy, and brain tumors

3D MEA arrays have significant applications in disease modeling, particularly in the study of neurodegenerative disorders, epilepsy, and brain tumors. By using patient-derived cells or genetically modified cells, 3D MEA arrays can replicate the pathological features of these diseases and enable the investigation of disease mechanisms and evaluation of potential therapeutic interventions.

In neurodegenerative disorder modeling, such as in Alzheimer's disease or Parkinson's disease, recent advances have concentrated on leveraging 3D culture systems and MEAs to gain a more profound understanding of disease progression and potential treatment options. 3D MEA arrays, in particular, offer a platform for analyzing neuronal dysfunction, network disruptions, and the effects of potential disease-modifying drugs. These arrays facilitate monitoring disease-related

biomarkers, such as aberrant neuronal firing patterns or pathological protein aggregates, in a more physiologically relevant context.

Researchers have explored the advantages of 3D culture systems, including cerebral organoids and a 3D human neuron-astrocyte-microglia culture model for modeling neurodegenerative diseases, as highlighted by Venkataraman et al. (2022) and Park et al. (2018) [151,152]. These models successfully replicated key disease features such as beta-amyloid aggregation and neuroinflammatory activity. Krokidis et al. (2021) underscored the significance of computational omics approaches in identifying disease progression and treatment response biomarkers [153]. Xiao et al. (2019) also introduced a novel MEA modified with nanocomposites for real-time monitoring of dopamine concentrations and neural spike firing in a rat model of Parkinson's disease [107]. This innovation demonstrates the potential of MEAs to elucidate disease mechanisms and evaluate treatment effects in the context of neurodegenerative disorders.

For epilepsy research, 3D MEA arrays provide a platform for studying seizure generation, propagation, and dynamics in 3D neuronal culture. They offer insights into the mechanisms underlying epileptogenesis, seizure initiation, and interictal activity. In addition, these arrays can be used to evaluate the efficacy of antiepileptic drugs and novel therapeutic approaches. Hsiao et al. (2015) and Dossi et al. (2014) demonstrated these arrays' ability to induce and record epileptiform discharges in human hippocampal slices, providing a platform for studying seizure generation and propagation [154,155]. Hill et al. (2010) demonstrated using MEAs to screen potential anticonvulsants in acute rat brain slices, enhancing the depth and quality of the data derived from these preparations [156]. Finally, Engel et al. (2001) highlighted the potential of invasive *in vivo* research using microelectrode techniques in patients with mesial temporal lobe epilepsy, underscoring the importance of these advanced technologies in advancing our understanding of epilepsy [157].

In brain tumors, 3D MEA arrays facilitate the investigation of tumor growth and invasion and the effects of anticancer therapies [97]. By integrating tumor cells with surrounding healthy neuronal networks, these arrays provide a unique opportunity to study the interactions between tumor cells and their microenvironment and the impact of tumor-related changes on network activity.

II.9.3 Fundamental neuroscientific research: Network dynamics and synaptic plasticity

3D MEA arrays have revolutionized fundamental neuroscientific research by offering unprecedented capabilities for studying network dynamics and synaptic plasticity. These arrays provide a means to investigate the complex interactions between neurons and emergent properties of neural networks.

By recording electrophysiological activity in 3D neuronal cultures, 3D MEA arrays enable the analysis of network dynamics, including spontaneous activity, synchronization, and oscillatory patterns [6]. These arrays help unravel the underlying mechanisms of information processing, neural coding, and the functional connectivity of neuronal circuits.

Moreover, 3D MEA arrays enable the study of synaptic plasticity, which is crucial for the learning and memory processes. Long-term potentiation (LTP) and long-term depression (LTD), the two primary forms of synaptic plasticity, can be investigated in 3D neuronal cultures using these arrays [158]. Such investigations provide insights into the cellular and molecular mechanisms underlying synaptic plasticity and can aid in developing novel therapeutic strategies for neurological disorders.

II.10 Challenges and future directions

II.10.1 Standardization and reproducibility

One of the critical challenges in 3D MEAs is the standardization and reproducibility of the array fabrication and experimental protocols. As the field advances, there is a growing need for standardized procedures and guidelines to ensure consistent and reliable results across different research groups and institutions. Standardization efforts should focus on key aspects such as array design, material selection, electrode configuration, and cell loading methods. Establishing standardized protocols for array fabrication, surface functionalization, and cell culture techniques will facilitate the comparison and replication of experimental results [159].

Reproducibility can be enhanced by sharing data, methodologies, and validated protocols within the scientific community. Open-access repositories and collaborative platforms can promote transparency and facilitate the exchange of knowledge and best practices among researchers [160].

II.10.2 Biocompatibility and long-term stability of 3D arrays

The biocompatibility and long-term stability of 3D MEA arrays are critical for their successful implementation in various applications. Biocompatibility refers to the compatibility of the array materials and their interactions with the surrounding biological environment. Selecting biocompatible materials is crucial to minimize adverse effects on cell viability, functionality, and long-term stability. Materials with appropriate mechanical properties, low cytotoxicity, and the ability to support neuronal growth and maturation are desirable [161].

The long-term stability of the arrays is essential to ensure the integrity of the recorded signals and to preserve the electrode-tissue interface over extended periods. Challenges, such as material degradation, signal drift, and electrode fouling, must be addressed. Developing novel materials and surface modifications that enhance long-

term stability and minimize electrode-tissue interactions are active research areas [109].

II.10.3 Miniaturization and integration of electronics

Advancements in miniaturization and integration of electronics are vital for enhancing the functionality and portability of 3D MEAs. Miniaturization enables higher electrode density and improved spatial and temporal resolution. Integrating electronics within the array platform allows for on-chip signal processing, amplification, and multiplexing, thus minimizing the need for external components and reducing the system's overall footprint. Integrated electronics also facilitates real-time data acquisition, on-site data analysis, and closed-loop experiments.

The challenges in miniaturization and integration include heat dissipation, power management, and signal integrity maintenance in densely packed arrays. Advances in microfabrication techniques, such as thin-film and flexible electronics, could contribute to overcoming these challenges [162].

II.10.4 Advance data analysis techniques for high-dimensional data

The increasing complexity and volume of data generated by 3D MEA arrays require advanced data analysis techniques to extract meaningful information and insights. High-dimensional data obtained from multiple electrodes and time series recordings necessitate the development of sophisticated data processing and analysis algorithms.

Machine learning techniques such as dimensionality reduction, clustering, and classification algorithms are valuable tools for extracting patterns and features from large-scale electrophysiological datasets [163]. These techniques enable the identification of network dynamics, neuronal subpopulations, and correlations among recorded signals.

Furthermore, integrating multimodal data, such as electrophysiological recordings and imaging data, provides a more comprehensive understanding of neuronal activity and network behavior. Co-registration of electrophysiological signals with calcium imaging or optogenetic data allows for investigating functional connectivity and information flow within 3D neuronal cultures [164].

II.10.5 Multi-modal recording approaches: simultaneous electrophysiology and imaging

Simultaneous recording of electrophysiological activity and imaging data is an emerging approach that offers a more comprehensive view of neuronal function and network dynamics. Combining 3D MEA arrays with imaging modalities, such as

calcium imaging or voltage-sensitive dyes, enables simultaneous capture of neuronal electrical activity and cellular imaging.

Simultaneous electrophysiology and imaging provide complementary information about network activity, cell types, and spatiotemporal dynamics. They allow the investigation of the relationship between neuronal electrical signals and calcium transients, enabling the study of cellular excitability, synaptic transmission, and network synchronization [116].

Integrating multi-modal approaches faces challenges in terms of data synchronization, compatibility of recording systems, and the need for advanced data fusion and analysis techniques. However, the synergy between electrophysiology and imaging holds great promise in understanding the complex dynamics of 3D neuronal cultures.

Chapter III: Platform design and methodology

III.1 Design concept

The concept and design philosophy is motivated by the need for an innovative technological platform capable of manufacturing a diverse spectrum of microelectrode arrays (MEAs), ranging from planar to three-dimensional (3D) configurations (refer to Figure III-1). With a strategic emphasis on enhancing cost-effectiveness and customization, the platform employs a bottom-up approach for fabricating 3D MEA devices. The platform establishes the initial planar architecture, leveraging the merits of conventional photolithography-based micromachining and exploiting the precision and scalability inherent in the photolithography process. Notably, to transition from planar to 3D structures, a pioneering template-assisted electrodeposition process for 3D electrode fabrication was conceived.

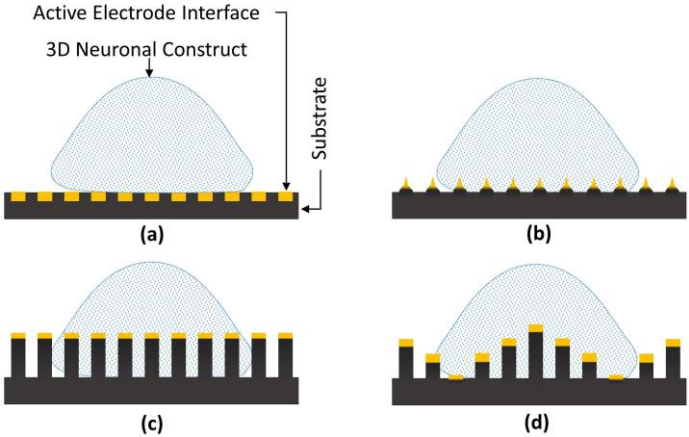

Figure III - 2. Schematic representation of different types of MEAs interacting with 3D neuronal constructs: (a) Planar MEA, (b) Protruding tip-based 3D MEA, (c) constant electrode height 3D MEA, and (d) Variable electrode height 3D MEA.

The rationale behind choosing electrodeposition as the preferred method is its capability to introduce substantial surface roughness, effectively addressing the interface rigidity concerns associated with conventional metal electrodes manufactured using Physical Vapor Deposition (PVD) techniques [165]. Furthermore, a bespoke circuitry system is introduced to ensure electrode selectivity during the electrodeposition process, affording meticulous control over the deposition thickness or height of the electrodes. The synergy of these three fabrication approaches unfolds

a myriad of MEA types, including planar MEAs (refer to Figure III-1a), protruding-tip-based 3D MEAs (refer to Figure III-1b), constant electrode height 3D MEAs (refer to Figure III-1c), and variable electrode height MEAs (refer to Figure III-1d). This comprehensive and integrated approach to MEA fabrication is the cornerstone for subsequent discussions on each fabrication process's specific methodologies and outcomes.

III.1.1 Definition of device architecture

Photolithography emerges as the cornerstone of the platform's design, forming the initial and crucial step in fabricating 3D MEAs. Precision at the microscale is a paramount characteristic of photolithography. The method relies on light exposure through a photomask to transfer intricate patterns onto a substrate, ensuring high accuracy and resolution at the micro-level. This precision is especially crucial in MEAs, where electrode dimensions and placements are paramount for effective neural interfacing.

Scalability is another crucial attribute of photolithography. The technique is inherently suited for large-scale production, allowing for the consistent replication of intricate patterns across numerous devices. In 3D MEA fabrication, scalability is vital for generating batches of devices with consistent and reproducible features, facilitating research and potential commercial applications.

Compatibility with various materials is a noteworthy advantage offered by photolithography. Photolithography is versatile in its applicability to a wide range of substrate materials. This versatility is critical in developing 3D MEAs, where the choice of materials can impact biocompatibility, electrical properties, and overall device performance.

III.1.2 Planar to 3D transformation approach

The transformation of the MEA from a two-dimensional planar structure to a three-dimensional configuration is a critical facet of its design philosophy, focusing on advancing MEAs. At the heart of this transformation is a template-assisted electrodeposition process tailored explicitly for fabricating intricate three-dimensional electrodes. The process involves the controlled deposition of metal ions onto a substrate, guided by a template that shapes the final structure.

Electrodeposition is a rational choice for neural interfaces due to its ability to increase surface roughness, a critical factor in mitigating rigidity issues associated with metal electrodes [166]. This method allows for the tailoring of surface properties, making it a versatile option for various applications [167]. The importance of surface roughness in creating a conducive interface for neural communication is further emphasized by the need for microtechnology fabrication in achieving selective electrical interfacing with the nervous system [168]. The potential of electrodeposition

is also highlighted in the development of high surface area platinum electrodes, which show enhanced performance in chronic neural stimulation [169].

Electrodeposition offers several advantages over PVD methods in the development of 3D MEAs. It is cost-effective, scalable, and repeatable, making it a suitable technique for precisely fabricating nanoelectrodes [170]. Electrodeposition's high deposition rate, resolution, and shape fidelity further enhance its applicability in microsystems. Electrodeposition can produce high-quality materials for electronic devices, including MEAs, at a lower cost and over a larger area than PVD methods [171]. These features make electrodeposition a favorable choice for the development of 3D MEAs.

III.1.3 Approach towards electrode selectivity and array customization

Precision in electrodeposition is indispensable for achieving the intended topographical variations in the electrode height, which, in turn, directly influences the functionality and performance of the MEAs. In the context of the overarching design philosophy, where control and customization are paramount, developing custom circuitry emerges as a strategic and innovative solution to enhance the precision of the 3D features inherent in MEAs.

A custom circuitry system is conceptualized and designed to operate in tandem with the electrodeposition process, where metal ions are selectively deposited onto a substrate guided by a template. The primary goal is to impart a high degree of selectivity, allowing to exert meticulous control over the growth of the 3D electrodes. This level of precision is instrumental in achieving a diverse range of heights for the electrodes, contributing to the adaptability and versatility of the fabricated MEAs.

The bespoke circuitry system is a testament to the commitment to tailoring the platform to meet specific experimental requirements and pushing the boundaries of customization in microelectrode array fabrication. Furthermore, the design philosophy underscores the need for adaptability in the fabrication process, accommodating a spectrum of MEAs ranging from planar to 3D. The custom circuitry becomes a linchpin in achieving this adaptability, allowing the controlled deposition of materials to form intricate 3D structures. This adaptability is crucial for addressing the diverse requirements of different experimental setups and research objectives.

III.2 Methodology

The primary consideration for developing MEAs is the compatibility of MEAs with the widely used existing *in vitro* readout platforms such as MEA2100-Systems (Multi Channel Systems MCS Gmb). These readout platforms can handle microelectrode arrays with 60, 120, or 256 electrodes/channels. Considering this, a 60-channel planar MEA is designed. The commercially available MEAs also inspired the electrode dimensions and pitch. The layout of electrodes in the array is customized

to optimize the distribution and trace routing, which will be discussed further in the following chapters.

III.2.1 Device layout

To evaluate the potential of the platform to develop customizable 3D MEAs, a standard 60-channel MEA layout was chosen. The standard layout consists of 60 circular electrodes in the center of a square chip traced to the contact/readout pads arranged on the periphery of the MEA chip via internal routing, as shown in the unshaded region in Figure III - 2. Further, a custom circuit is introduced in the layout to support electrodeposition, as shown in the red-shaded region in Figure III - 2. This circuit is placed outside the periphery (shown as a dashed black line in Figure III - 2) of the actual MEA chip layout to discard the circuitry easily upon realizing the desired MEA.

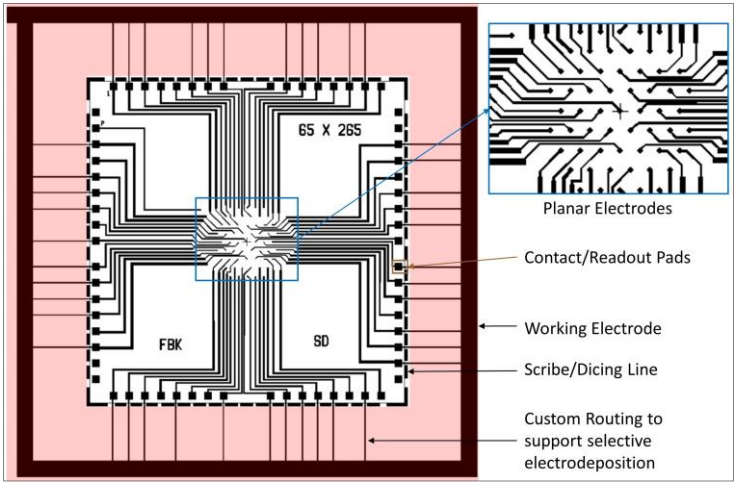

Figure III - 2. Schematic representation of MEA device layout with customized external circuitry.

III.2.2 Development of planar device architecture

Based on the platform design, a photolithography-based microfabrication process for developing the planar device architecture is defined. The substrate material selected is a double-polished borosilicate glass wafer, 600 µm thick, chosen for its high optical transparency and biocompatibility. Gold is selected as the material for the electrode layout in MEAs due to its biocompatibility, low impedance, and stability. Silicon dioxide (SiO_2) is the commonly chosen passivation layer for MEAs due to its biocompatibility, electrical insulation capability, and stability in physiological

environments. It provides a protective barrier for the underlying conducting tracks and microelectronic structures crucial for electrophysiological investigations.

To fabricate planar MEA devices, the glass wafers are cleaned for 20 seconds in a buffered hydrofluoric acid (HF) solution bath to ensure the cleanliness of the wafer surface. Subsequently, the glass wafer is rinsed using DI water and dried in a controlled environment (refer to Figure III-3a). A 10 nm thick chrome (Cr) layer is deposited on the clean glass wafer using an ultra-low vacuum thermal evaporator, followed by the deposition of a 200 nm thick gold (Au) layer (refer to Figure III-3b). The chrome layer acts as an intermediate layer to promote adhesion between the glass wafer and the gold layer. The Cr/Au-coated glass wafer is then primed with a Hexamethyldisilazane (HMDS) layer at 150 ˚C, an essential process step promoting uniform coating of the photoresist over the wafer. The primed wafer then undergoes the spin coating of a 2-µm thick colored positive-tone photoresist over the metallic layer (refer to Figure III-3c). The resist-coated wafer is subjected to a soft-bake at 100 ˚C for 1 min to evaporate excess solvent from the layer of the photoresist and prepare the wafer for patterning.

The photoresist-coated wafer is exposed to UV radiation through a bright field mask, consisting of a positive image layout of the device architecture using an i-line mask aligner (KARL SÜSS MA6) (refer to Figure III-3d). This step transfers a positive pattern image on the photoresist by dissolving the UV-exposed region of the photoresist. The exposed photoresist is then developed using a generic developer solution, generating a positive image photoresist mask on the metal layers (refer to Figure III-3e). A multi-step wet chemical etching process transforms the pattern from the photoresist to the metal layers. Initially, the exposed gold layer is etched by placing the wafer inside an aqua regia solution bath for a few seconds while shaking the bath gently. Upon successfully etching the Au layer, the wafer is placed in a chrome etch bath and shaken gently until the chrome is etched completely. The wafer is rinsed thoroughly upon etching the Cr/Au layer to remove any residual etching solution. Finally, the wafer is subjected to a resist strip process to remove the photoresist mask by placing the wafer in an acetone bath. Upon stripping the photoresist mask, a glass wafer consisting of the planar device architecture is realized refer to Figure III-3f).

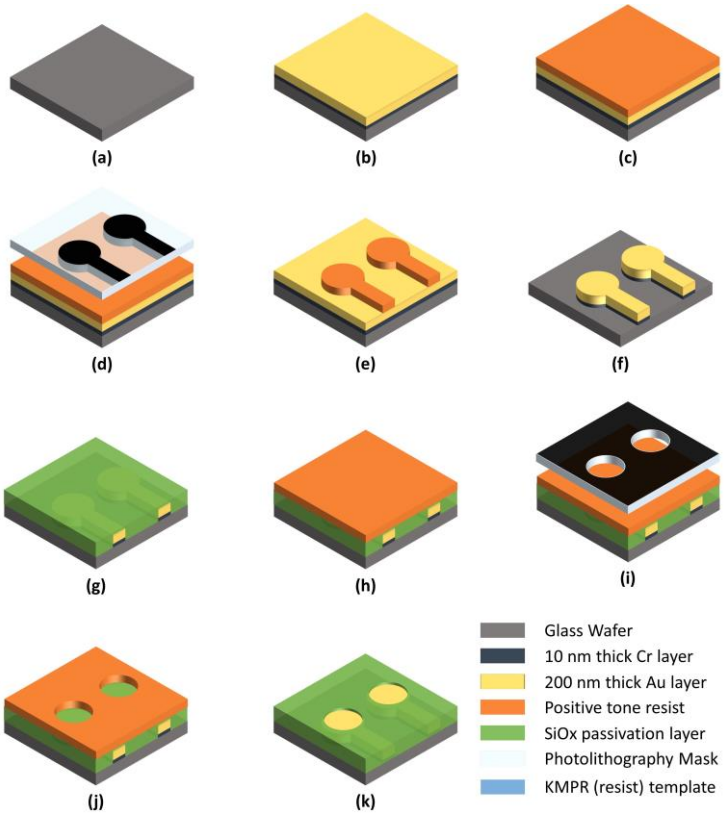

Figure III - 3. Schematic representation of process flow for the fabrication of planar device architecture. (a) Substrate, (b) Cr/Au layer deposited thermally over the substrate. (c) Application of photoresist over the Cr/Au layer. (d) A bright-field photolithography mask is aligned over the wafer stack to pattern the photoresist through UV radiation. (e) Patterned photoresist. (f) Photoresist pattern transferred to the Cr/Au layer through wet chemical etching. (g) Deposition of a passivation layer over the patterned substrate. (h) Photoresist layer coated over the passivated substrate stack. (i) A dark-field photolithography mask aligned over the substrate stack to pattern the photoresist. (j) Patterned photoresist. (k) Photoresist pattern transferred to the passivation layer through reactive ion etching, yielding partially passivated planar device architecture.

To transform the planar device into a 3D MEA, the partial passivation of the planar architecture plays an essential role. A few hundred nanometers thick silicon dioxide layer is deposited over the planar architecture of the wafer (refer to Figure III-3g). Further, the passivated wafer undergoes an HMDS priming step, followed by coating a colored photoresist, as described earlier (refer to Figure III-3h). The photoresist-coated wafer is subjected to a soft-bake step to remove any excess solvent from the resist layer. The wafer is then subjected to the second exposure to UV radiation through a dark field mask, consisting of a layout for unmasking the

electrodes and the contact pads from the passivation layer using an i-line mask aligner (KARL SÜSS MA6) (refer to Figure III-3i). This step transfers a positive pattern image on the photoresist by dissolving the UV-exposed region of the photoresist. The exposed photoresist is then developed using a generic developer solution, generating a positive image photoresist mask on the passivation layer (refer to Figure III-3j). The photoresist mask is then subjected to a resist hardening step by baking the photoresist mask in an oven at 120 ˚C for 1 hour to create a resist hard mask over the passivation layer. The exposed passivation layer is subjected to reactive ion etching using a plasma etching tool (AW-903ER Plasma Etch RIE, Allwin21 Corp.). Upon completion of the SiO2 etching, the resist hard mask is stripped away using an acetone bath, leaving behind a partially passivated planar MEA architecture (refer to Figure III-3k).

III.2.3 Development of the template

To transform planar MEA into 3D counterparts, a thick photoresist-based template is fabricated over the partially passivated MEA (refer to Figure III-4a). For the development of this template, a thick chemically amplified negative photoresist, specifically KMPR-1035 from Kayaku Advanced Materials, Inc, is selected due to its compatibility with cleanroom processes.

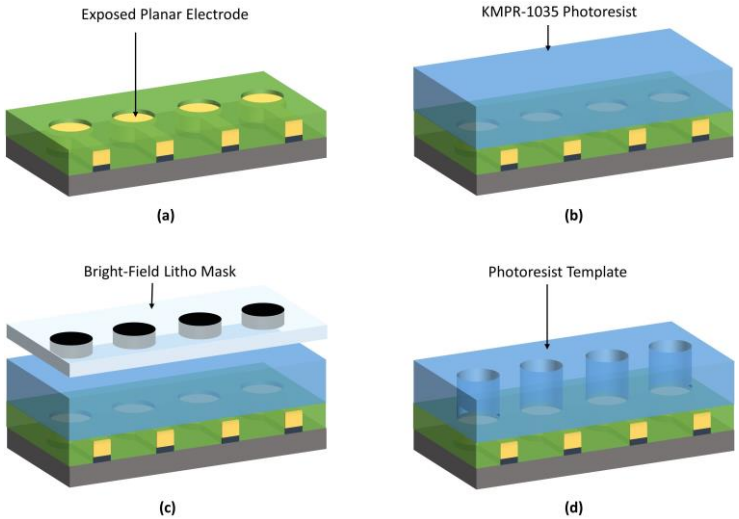

Figure III - 4. Schematic representation of template development process. (a) Partially passivated planar MEA substrate. (b) A negative tone photoresist coated over the MEA substrate. (c) A bright-field photolithography mask aligned over the substrate stack to pattern the photoresist through UV radiation. (d) Planar MEA consisting of the photoresist template.

Initially, the wafer containing planar MEAs undergoes a coating process with a thick layer of KMPR photoresist (refer to Figure III-4b). A 30-minute soft-bake succeeds this at 100 °C to ensure proper adhesion and stability of the photoresist layer. Subsequently, the photoresist layer is exposed to UV light through a bright-field mask, facilitated by an i-line mask aligner setup (refer to Figure III-4c). The exposure to UV radiation initiates a cross-linking process, solidifying the photoresist. To complete the curing process, a post-exposure bake is executed at 100 °C for 6 minutes, ensuring the comprehensive curing of the exposed area of the photoresist. Following this, the unexposed region of the photoresist is developed using the SU-8 developer solution for 20 minutes, aided by a shaker plate and mild agitation. This meticulous process creates a template featuring cylindrical holes atop the exposed planar electrodes (refer to Figure III-4d).

III.2.4 Selective electrodeposition mechanism

The custom circuitry, seamlessly integrated along the periphery of the planar Microelectrode Array (MEA) architecture, facilitates the electrode selectivity during electrodeposition. This circuitry serves the purpose of dividing the planar electrodes into distinct groups through contact pads. These electrode groups denoted as G1, G2, and G3, are then individually connected to a common working electrode (W.E.) to support the electrodeposition process. Multiple strategies exist for grouping the electrodes, each presenting unique advantages and disadvantages, and these methodologies are explained in the subsequent chapters. Before initiating the electrodeposition process, a crucial step involves subjecting the planar MEA and the photoresist template to an oxygen plasma treatment. This treatment enhances the wettability of the template.

Figure III-5 schematically illustrates the concept of the selective electrodeposition mechanism, where the custom circuit is visually depicted by a colored solid trace line connected to a working electrode (W.E.) (refer to Figure III-5a). In the initial stage of the electrodeposition process, all electrode groups (G1, G2, and G3) are concurrently linked to the common working electrode. This connection is maintained throughout the electrodeposition process by applying current through the common working electrode facilitated by a galvanostat. The MEA undergoes template-assisted electrodeposition until the desired thickness/height of the first group of electrodes is achieved (refer to Figure III-5b).

Before transitioning to the second stage of electrodeposition, the G1 electrodes are deliberately disconnected (indicated by a red cross in Figure III-5c) from the working electrode. Subsequently, the remaining electrodes undergo electrodeposition until reaching the desired height for the second group of electrodes (refer to Figure III-5c). The final stage involves disconnecting the second group (G2) electrodes from the working electrode (indicated by a red cross in Figure III-5d), allowing the remaining

electrodes to undergo electrodeposition until achieving the desired height of G3 electrodes (refer to Figure III-5d).

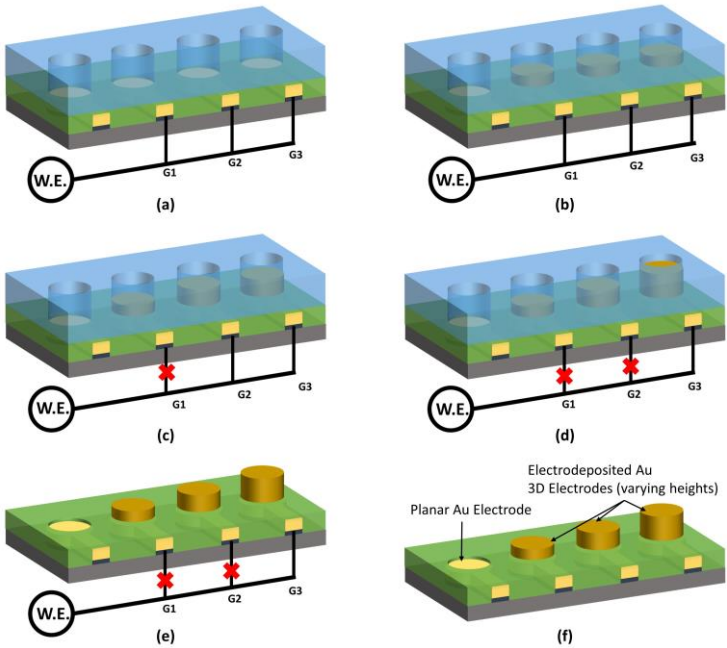

Figure III - 5. Schematic representation of selective electrodeposition mechanism. (a) Planar MEA substrate with a photoresist template and custom external circuitry dividing the planar electrodes into three groups denoted by G1, G2, and G3. (b) Stage-I electrodeposition: All three electrode groups subjected to electrodeposition through the common working electrode(W.E.). (c) Stage-II electrodeposition: G1 electrodes disconnected from the working electrode, and the remaining electrodes (G2 and G3) are subjected to electrodeposition. (d) Stage-III electrodeposition: G2 electrodes disconnected from the working electrode, and the remaining electrodes (G3) are subjected to electrodeposition. (e) Variable electrode height 3D MEA upon removal of photoresist template. (f) Final 3D MEA realized upon removal of the external circuitry via dicing.

Upon the completion of the electrodeposition process, the photoresist template is removed using a PG-Remover strip solution, resulting in the realization of the 3D MEA (refer to Figure III-5e). To remove the custom circuitry from the MEA, the 3D MEA device is precisely diced along the scribe line (indicated by a dashed black line in Figure III-2). This dicing process yields an MEA featuring multiple individual channels and microelectrodes of varying heights (refer to Figure III-5f).

III.2.5 Partial passivation of the 3D electrodes

To enable the 3D electrodes to target specific regions of the cell culture, a partial/sidewall passivation of the 3D microstructures plays a crucial role. Parylene-C is a promising material for 3D microelectrode arrays for this application due to its conformal coating abilities, chemical resistance, and biocompatibility [172]. It has been used as an encapsulation material for medical implants, demonstrating its potential for biocompatible applications. The material's chemical inertness and mechanical strength make it suitable for use in wet environments.

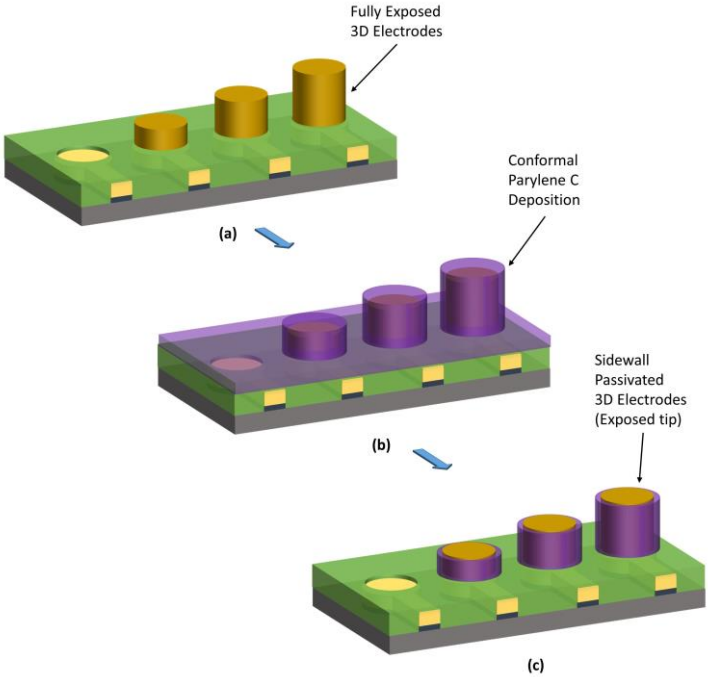

Figure III - 6. Schematic representation of partial passivation of the 3D electrodes. (a) 3D MEA with fully exposed 3D electrodes. (b) Deposition of Parylene C passivation layer. (c) Selective removal of Parylene C from the horizontal surface via reactive ion etching.

The varying height 3D MEA (refer to Figure III-6a) is initially treated with a short oxygen plasma treatment to clean and activate the MEA surface. A few micron thick Parylene C layer is then deposited on the MEA using a low-pressure chemical vapor deposition (LP-CVD) technique (refer to Figure III-6b). After the deposition, the Parylene C layer is removed selectively using an anisotropic oxygen plasma etching technique. The process results in the complete removal of Parylene C from the lateral

surface while etching less than 50 % from the vertical surface, yielding sidewall passivated 3D microelectrodes exposed from the top (refer to Figure III-6c).

III.2.6 Device integration and packaging

A meticulous device packaging strategy complements the finalization of the Microelectrode Array (MEA) fabrication process. After the sidewall passivation process, the individual MEA chips are delicately separated along the scribe lines. For integration into the MEA2100 readout system, a custom Printed Circuit Board (PCB) compatible with the readout adaptor is crafted with precision. The MEA chips find their secured position on the PCB using a minute quantity of epoxy glue, ensuring stability and alignment. Gold wire bonding is employed to connect the contact pads on the MEA chip to the corresponding routing on the PCB to establish electrical connectivity (refer to Figure III-7a). A layer of epoxy resin shields this intricate wiring, strategically applied to prevent any potential short-circuiting. Further, a glass ring is bonded to the PCB, incircling the 3D MEA to accommodate cell culture well (refer to Figure III-7b).

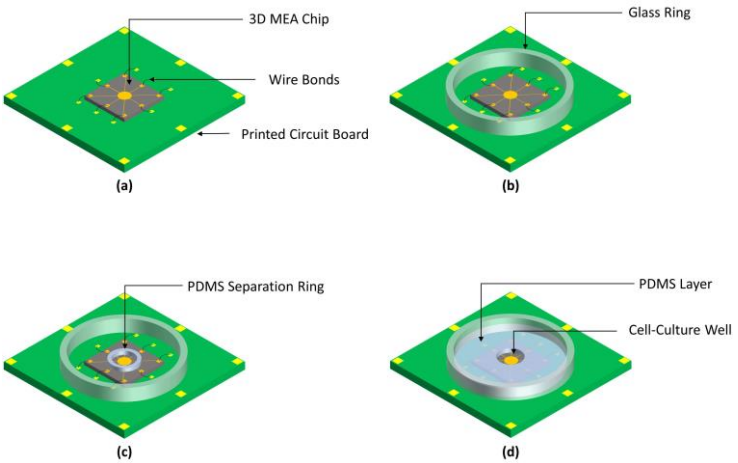

Figure III - 7. Schematic representation of device packaging. (a) 3D MEA chip mounted on a customized printed-circuit board (PCB) and interconnected using gold wire bonds. (b) A glass containment ring bonded to the PCB confining the 3D MEA chip and wire bonds. (c) A PDMS ring mounted on the 3D MEA chip to define the cell culture area. (d) Fully package device consisting of well defined and isolated cell culture area.

Considering the necessity of an isolated environment for cell culture, a Polydimethylsiloxane (PDMS) ring is fixed on the 3D MEA chip (refer to Figure III-7c). This ring serves as a containment well on the MEA chip. The gap between the PDMS ring and the glass ring is filled by pouring liquid PDMS (solvent + curing agent). The

liquid PDMS is finally cured to yield a fully integrated 3D MEA with a cell-culture well (refer to Figure III-7d).

This configuration, illustrated in Figure III-7, provides structural support and delineates the boundary for subsequent cell culture procedures. The amalgamation of these packaging components ensures the robustness, functionality, and suitability of the MEA device for its intended applications.

III.3 Device characterization: Tools and techniques

III.3.1 Optical profilometry

Utilizing a 3D optical profilometer, specifically the Zygo NewView™ 6000, has been instrumental in advancing the methodologies employed in this study. This optical profilometer stands as a sophisticated instrument for capturing intricate height and surface data, leveraging the capabilities of Scanning White Light Interferometry. Its application in this research has proven invaluable, offering a fast and non-contact means for obtaining precise 3D measurements. This technology has played a pivotal role in monitoring the heights of 3D electrodes at critical stages of the fabrication process, ensuring meticulous control and validation of the developed structures. The optical profilometer has also been pivotal in conducting comprehensive template shape analyses, contributing to a nuanced understanding of the fabricated structures. The efficiency and precision afforded by this tool have significantly enhanced the quality of data acquisition, allowing for a more thorough and accurate investigation into the intricacies of the template-assisted electrodeposition process and the resultant microelectrode array configurations.

III.3.2 Scanning electron microscopy

Scanning Electron Microscopy (SEM) has emerged as an indispensable tool throughout this study, playing a pivotal role in elucidating intricate details essential for advancing Microelectrode Array (MEA) technology. SEM has proven instrumental in providing high-resolution images of the fabricated MEA chips, enabling a comprehensive inspection of the surface morphology and structural integrity at the micro and nanoscales. The capability of SEM to delve into the intricate features of the electrode surfaces, sidewall passivation, and the template-assisted electrodeposition process has been particularly invaluable. This microscopic scrutiny has facilitated a meticulous evaluation of the effectiveness of various fabrication techniques and allowed for the identification and rectification of potential irregularities. SEM imaging has, therefore, been integral in ensuring the precision and reliability of the developed MEA devices.

III.3.3 Electrode resistance measurements

The Keithley Series 2400 Sourcemeter has played a crucial role in this study, particularly in the precise measurement of the resistance of 3D electrodes. This sophisticated instrument from Keithley Instruments is a powerful tool for sourcing and measuring electrical signals with high precision. Its versatility and accuracy make it essential to characterizing fabricated 3D microelectrode arrays (MEAs). The Sourcemeter's capability to provide controlled voltage and measure resulting currents has been instrumental in assessing the resistance properties of the intricate 3D electrode configurations.

III.3.4 Electrode impedance characterization

The HP4192 LF Impedance Analyzer has proven indispensable in this study, serving as a critical tool for thoroughly characterizing 3D microelectrode arrays (MEAs). This sophisticated instrument, part of the HP Precision LCR Meter series, specializes in low-frequency impedance analysis, providing invaluable insights into the electrical properties of the fabricated 3D MEAs. The analyzer's capacity to measure impedance over a range of frequencies is particularly advantageous for understanding the electrochemical behavior of intricate 3D electrode structures. Its precision and sensitivity make it well-suited for capturing subtle variations in impedance that are crucial for evaluating the performance of the MEAs. The HP4192's ability to discern changes in impedance at low frequencies aligns with the requirements of this study, offering detailed information on the electrical characteristics of the developed MEAs. The instrument's contribution extends beyond basic impedance measurements; it plays a pivotal role in elucidating the nuanced electrical responses of the 3D MEAs, thereby enhancing the overall comprehension of their behavior and functionality in neuroscientific applications.

III.3.5 Device performance validation

The MEA 2100 System (MEA 2100-System, MCS) has played a pivotal role in this study by being an indispensable tool for performing electrode background noise measurements and recording electrophysiological activity. Engineered by Multi Channel Systems (MCS), this advanced electrophysiology platform has demonstrated unparalleled efficacy in capturing and analyzing neural signals with high precision. Its significance lies in its ability to conduct meticulous electrode background noise measurements, providing crucial insights into the baseline noise characteristics associated with the fabricated 3D microelectrode arrays (MEAs). This capability is essential for assessing the signal-to-noise ratio, a critical metric in electrophysiological studies, ensuring the reliability and clarity of recorded neuronal signals. Moreover, the MEA 2100 System excels in recording electrophysiological activity, enabling the

comprehensive examination of neuronal responses and network dynamics. Its sophisticated data acquisition and signal processing features have facilitated detailed investigations into the performance of the 3D MEAs under various experimental conditions. The reliability and versatility of the MEA 2100 System have thus contributed significantly to the success of this study, providing a robust platform for acquiring and interpreting electrophysiological data from the developed 3D MEAs.

Chapter IV: Platform validation through the development of multi-level 3D MEAs

Part of this chapter has been published in:

Neeraj Yadav, Leandro Lorenzelli, and Flavio Giacomozzi,
"A Novel Additive Manufacturing Approach towards Fabrication of Multi-Level Three-Dimensional Microelectrode Array for Electrophysiological Investigations",
Proceedings of the 2021 23rd European Microelectronics and Packaging Conference & Exhibition (EMPC), Gothenburg, Sweden, 13–16 September 2021; IEEE: Piscataway, NJ, USA, 2021; pp. 1–5.

IV.1 Introduction

Chapter 4 represents a pivotal phase in our exploration, transitioning from conceptualization to concrete realization. Following the blueprint laid out in Chapter 3, this chapter seeks to test the efficacy of the proposed platform by translating theoretical frameworks into practical applications. The primary objective is to establish a proof of concept that validates the conceptualized platform and propels it into tangible technological advancement.

A robust 60-channel MEA layout is engineered and intricately intertwined with custom external circuitry to substantiate the conceptualized platform. This intentional design choice aims to generate a device compatible with existing readout platforms. The 60-channel MEA layout becomes the foundation for developing a 3D MEA structure, where electrodes extend across three distinct height levels. This strategic design is motivated by the pursuit of capturing neural activity across multiple spatial dimensions, an essential factor in decoding the complexity of neural networks.

In the subsequent sections, we embark on a detailed journey through the developmental process. From the adaptation of the 60-channel MEA layout to accommodate multi-level features to the nuanced electrodeposition processes, every step is a testament to the precision and innovation required to usher in a new era of neural interface technologies. The platform's validation extends beyond fabrication, encompassing a comprehensive topographical characterization process, which will be unveiled in subsequent sections.

IV.2 Design and layout

In the pursuit of optimizing functionality and practicality, the design and layout of the devised MEAs stand as a testament to meticulous planning and innovative engineering. Beyond ensuring device compatibility with existing readout platforms, the orchestration of a seamless batch-processing system has emerged as a cornerstone of our design philosophy. This aspect not only simplifies the manufacturing procedures but also enhances the scalability of the complete production process. The design

consists of three mask layers. The first mask (M1) defines the planar device architecture in a metal layer on the wafer. The second mask (M2) defines the windows in the passivation layer over the metal electrodes and other regions of interest. Finally, the third mask (M3) defines the photoresist template for the electrodeposition of the 3D electrodes.

IV.2.1 MEA batch layout

Examining the batch layout unveils a meticulously designed arrangement consisting of eight 60-channel Microelectrode Arrays (MEAs). This setup is skillfully accompanied by external circuitry, interconnected with precision through a single trace. The integration of these components serves a two-fold objective: firstly, to optimize the spatial utilization of the wafer, and secondly, to leverage the combined capabilities of the external circuitry, converging towards a shared working electrode during the intricate process of electrodeposition.

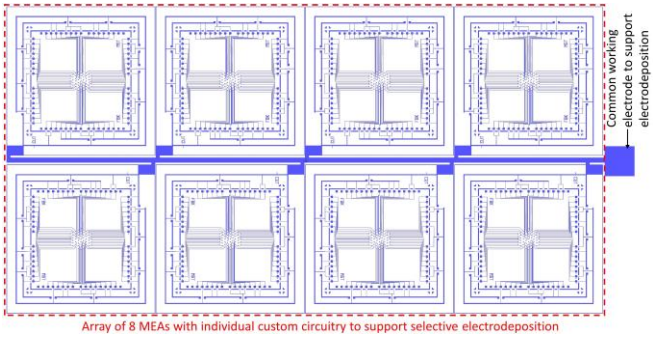

Figure IV - 3. MEA batch layout illustrating a batch of eight planar MEA devices connected to a single working electrode.

Along with the device compatibility with the existing readout platforms, the batch processing of devices has been a key design consideration. At the wafer scale, the layout consists of eight 60-channel MEAs with external circuitry connected to a single trace intended to act as a common working electrode during electrodeposition (refer to Figure IV-4). The use of the minimum photolithography mask iterations to define the device architecture in metal layers has been another key design consideration, as every iteration in lithography masks significantly increases the fabrication cost. The current layout consists of a single lithography mask to define the device's planar architecture.

IV.2.2 Individual device layout

IV.2.2.1 Mask 1: Device architecture layout

The first mask, designated as M1, outlines the planar device architecture to be etched into a metal layer on the wafer. This bright-field photolithography mask adopts a positive image of the layout, meaning that the pattern image on the mask is transferred onto the photoresist. Each device layout spans a 15 x 15 mm2 area, featuring a central 60-channel Microelectrode Array (MEA) layout within a 10 x 10 mm^2 space. Additionally, custom circuitry is seamlessly integrated along the periphery of the MEA layout (refer to Figure IV-2).

Within the MEA layout are 60 circular electrodes, each with a diameter of 70 µm. These electrodes are strategically arranged in a hexagonal array with a pitch of 265 µm. The hexagonal array pattern is deliberately chosen to enhance the spacing between traces connecting the electrodes to the contact pads at the MEA layout's periphery. The contact pads, each measuring 220 µm x 220 µm, are positioned inside the scribe/dicing line, facilitating the integration process with the PCB during the device packaging phase.

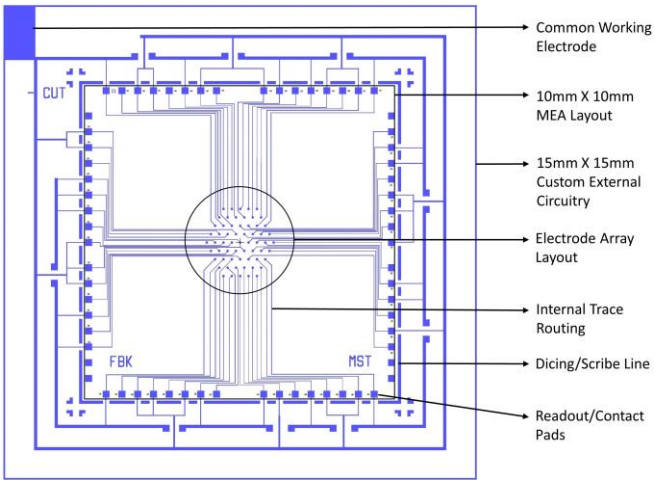

Figure IV - 2. The individual device architecture layout is defined through the photolithography mask M1.

IV.2.2.2 Mask 2: Device passivation layout

The second mask, denoted as M2, delineates the configuration for establishing the passivation layer on the planar device architecture. This photolithography mask adopts a dark-field polarity, signifying that the layout is transparent in the reticle. It

encompasses a negative representation of the intended layout to be etched onto the photoresist. Specifically, the mask incorporates 65 µm circular patterns precisely positioned over the metal electrodes (refer to Figure IV-3). This placement serves the purpose of removing the passivation layer for the electrode pads and defining the active region of the electrodes. Furthermore, the mask integrates 200 µm square windows aligned over the contact pads, strategically exposing the metal through the passivation layer.

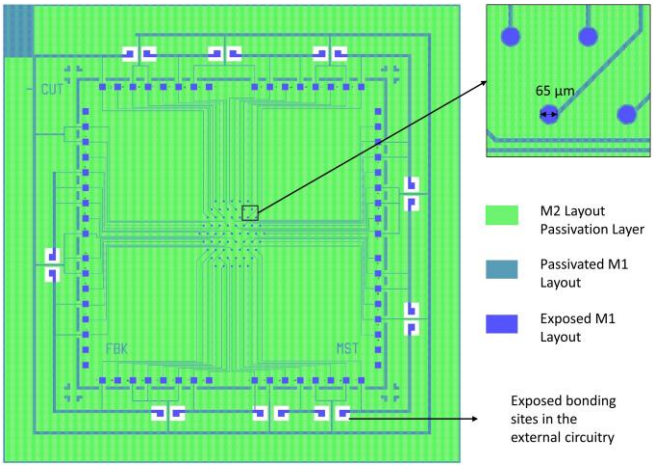

Figure IV - 3. Overlay of the M2 layout on top of the M1 layout.

Figure IV – 3 presents the overlay of the second mask (M2) layout, defined in green, on top of the M1 layout, defined in blue.

IV.2.2.3 Mask 3: Photoresist template layout

The third mask, referred to as M3, delineates the arrangement for creating the template supporting electrodeposition over the planar electrodes. This photolithography mask employs a bright-field polarity, indicating that the layout appears dark in the reticle. The bright-field nature of the mask aligns with the selected negative-tone development resist used for the template's formation. In this context, the negative-tone resist reacts to UV radiation by undergoing crosslinking, preserving itself on the substrate. Consequently, the photoresist captures a negative reproduction of the layout depicted on the mask.

M3 incorporates circular pads positioned in alignment with the planar electrodes specified in M1 (refer to Figure IV-4). These elements are designed to generate the cylindrical template essential for the electrodeposition process of 3D electrodes. Additionally, M3 includes a design for the external circuitry's manipulation, facilitating

the creation of multi-level 3D MEAs by exposing the circuit bonding sites within the external circuitry.

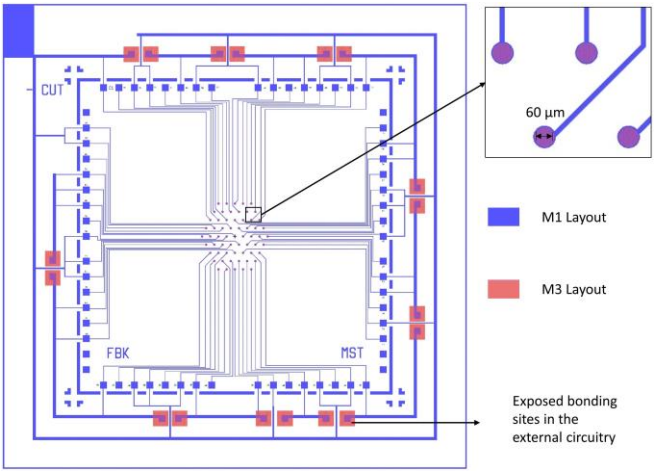

Figure IV - 4. Overlay of the M3 layout on top of the M1 layout.

Figure IV – 4 presents the overlay of the third mask (M3) layout, defined in red, on top of the M1 layout, defined in blue.

IV.3 Custom circuitry for selective electrodeposition: Layout and operation

IV.3.1 Circuit layout

The circuitry for selective electrodeposition is designed along the periphery of the primary MEA layout defined inside the scribe/dicing line. A dashed scribe line is adapted to facilitate traces connecting contact pads to the external circuitry. The external circuitry divides the 60 planar electrodes into three groups distributed uniformly in the array (refer to Figure IV-5). The electrodes which are not connected to the external circuitry are represented as Group 1 electrodes. The Group 1 electrodes are presented in blue color in the layout (refer to Figure IV-5); these electrodes are intended not to undergo electrodeposition and remain planar.

The external circuitry for selective electrodeposition is divided into a primary and secondary circuit. The primary circuit remains permanently connected to the working electrode and can only be removed through wafer dicing upon completion of the electrodeposition process. On the other hand, the secondary circuitry is designed to switch on demand and is an essential development to achieve selective electrodeposition while using a single photolithography mask to define the device

architecture. The secondary circuit is designed in multiple parts featuring pads for wire bonding to complete the circuit.

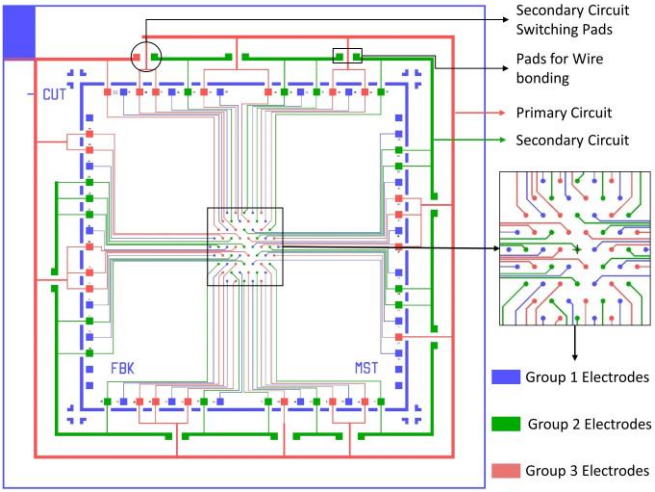

Figure IV - 5. Layout of custom circuitry for selective electrodeposition dividing the electrodes into separate groups.

Figure IV-5 represents the layout of the custom circuitry designed to support selective electrodeposition. The layout is color-coded to represent the association of the electrodes to the external circuitry. The blue color represents the Group 1 electrodes, which are designed to remain separate from the external circuit. The Group 2 electrodes are represented by green color and are directly associated with the secondary circuit. The secondary circuit can be connected or disconnected from the working electrode through the secondary circuit switching pads. The electrodes presented in red color are the Group 3 electrodes and are associated with the primary circuit. The primary circuit is permanently connected to the working electrode.

IV.3.2 Circuit operation for selective electrodeposition

The external circuitry is developed to allow for a two-stage electrodeposition process by manipulating the secondary circuit. For the first stage of the electrodeposition, the secondary circuit is completed using gold wire bonds, and the circuit is activated by connecting the secondary circuit with the primary circuit using wire bonding through the secondary circuit switching pads (refer to Figure IV-6a). This circuit configuration integrates the primary and the secondary circuit, allowing for simultaneous electrodeposition of Group 2 and Group 3 electrodes. This configuration obtains the second level (Level II) electrode.

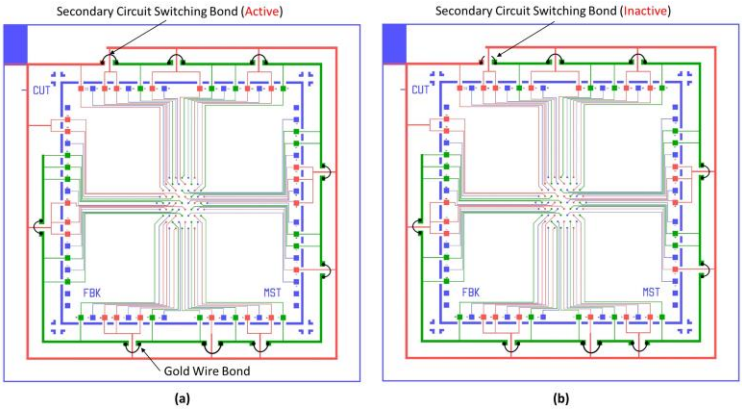

Figure IV - 6. Layout describing the various operational modes of the external circuitry. (a) Circuit layout for Stage I electrodeposition. (b) Circuit layout for Stage II electrodeposition.

The secondary circuit is shorted with the primary circuit to initiate the first stage of the electrodeposition process, where Group 2 and Group 3 electrodes are subjected to the electrodeposition simultaneously (refer to Figure IV-6a). For the second stage of electrodeposition, the secondary circuit is disconnected from the primary circuit by removing the secondary circuit switching bond (refer to Figure IV-6b). This circuit configuration disconnects the Group 2 electrodes from the working electrode, allowing for further electrodeposition of Group 3 electrodes. The Stage II electrodeposition results in the development of third-level (Level III) electrodes.

IV.4 Development of multi-level 3D MEA

IV.4.1 Fabrication of planar device architecture

A batch of 8 planar gold MEAs (refer to layout described in Figure IV-5), each MEA consisting of 60 planar electrodes with a diameter and pitch of 70 µm and 265 µm, respectively, is fabricated on a glass substrate utilizing a standard lithography procedure (refer to Figure III-3a-f). Initially, a clean glass substrate underwent a 20 nm chromium layer deposition, succeeded by a 100 nm gold layer. Subsequently, to actualize the Microelectrode Array (MEA) layout, the gold-coated substrate is coated with a positive tone photoresist, followed by exposure to Ultraviolet (UV) radiation through mask M1 using the MA6 mask aligner by Karl Suss. Following exposure, a standard recipe is employed for development, resulting in a positive rendition of the layout pattern on the photoresist. Next, a gold and chromium etch process transfers the pattern into the Cr/Au layer, thereby realizing a planar MEA configuration. To

provide passivation for the MEA chip, a 200 nm silicon dioxide film is grown utilizing Plasma-Enhanced Chemical Vapor Deposition (PECVD).

Furthermore, the wafer undergoes a second photolithography process to define the passivation layer (refer to Figure III-3g-k). The second mask (M2) is utilized to define the layout of the photoresist coating over the passivation layer. The pattern transfer from the photoresist to the passivation layer is carried out using a reactive ion etch. Finally, the photoresist is stripped away to realize partially passivated planar MEAs as described earlier in the layout.

IV.4.2 Development of photoresist template

The photoresist template is developed using the protocol described in the methodology section of Chapter III (refer to Figure III-4). The wafer containing planar MEAs is subjected to a coating process involving an 80 µm thick layer of KMPR photoresist. A 30-minute soft-bake at 100 °C follows this to ensure optimal adhesion and stability of the photoresist layer. Subsequently, the photoresist layer undergoes exposure to UV light through a bright-field mask (M3), facilitated by an i-line mask aligner setup. The exposure to UV radiation triggers a crosslinking process, effectively solidifying the photoresist.

To finalize the curing process, a post-exposure bake is conducted at 100 °C for 4 minutes, ensuring thorough curing of the exposed area of the photoresist. Following this step, the unexposed region of the photoresist is meticulously developed using the SU-8 developer solution for 20 minutes, with the assistance of a shaker plate and gentle agitation. This precise procedure creates a template featuring cylindrical holes, each measuring 60 µm in width and 80 µm in diameter, meticulously positioned atop the exposed planar electrodes.

IV.4.3 Template-assisted selective electrodeposition of multi-level 3D microelectrodes.

IV.4.3.1 Experimental setup

The setup for electrodeposition of gold 3D Microelectrode Arrays (MEAs) involves several vital components and meticulous procedures to ensure precise and uniform deposition (refer to Figure IV-7). A hot water bath placed on a hotplate with a magnetic stirrer is the primary heating source, maintaining the bath temperature at a constant 55°C. A specialized additive-free electroplating solution (AUROLYTE CN200, Atotech Deutschland GmbH & Co. KG) is transferred into a glass or plastic beaker. The beaker is placed inside the hot water bath, exposing the solution to the controlled temperature environment for uniform heating. Within the beaker, a magnetic stirring bead is added to stir the electroplating solution continuously at 275 rpm. Before initiating the electrodeposition process, the plating solution and the hot water bath are preconditioned for approximately 1 hour at 55°C to ensure thermal equilibrium.

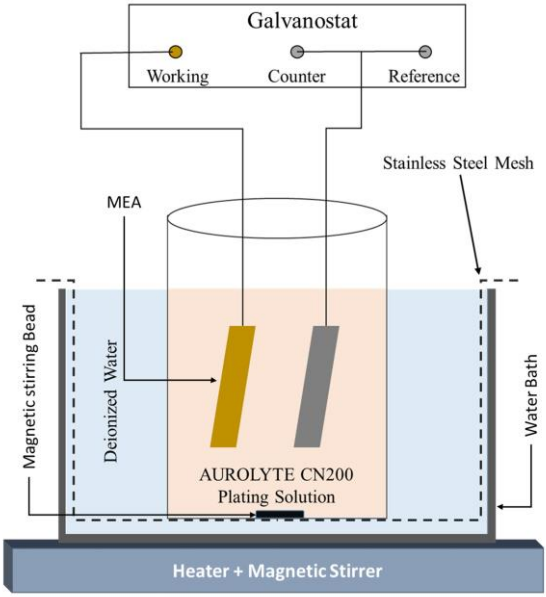

Figure IV - 7. Schematic representation of the setup for electrodeposition of multi-level gold microelectrodes.

A galvanostat is utilized to apply the deposition current required for electrodeposition, providing precise control over the flow of electrical current during the process. The MEA is connected to the galvanostat's working electrode, and a titanium mesh is used as a counter/reference electrode. The desired deposition rate and thickness of gold microstructures onto the MEAs is achieved by adjusting current density and duration parameters. This setup facilitates reproducible and high-quality electrodeposition, enabling the fabrication of precise and reliable microelectrode arrays for various biomedical and research applications.

IV.4.3.2 Multi-stage selective electrodeposition

Before starting with the multi-stage electrodeposition process, the wafer is diced to remove four of the eight MEAs from the working electrodes, and the remaining MEAs are subjected to a gold wire bonding process to complete the secondary circuit and switch it to active mode by completing the connection with the primary circuit. The wire bonds are then covered and insulated using epoxy glue. The MEA is then subjected to a short exposure to the oxygen plasma to improve the wettability of the template. The O_2 plasma-treated MEA is finally connected with the working electrode of the galvanostat and placed inside the electroplating solution bath against a titanium

counter electrode. The Stage I electrodeposition is then initiated by applying a deposition current density of 8 mA/cm^2 across the electrochemical cell using the galvanostat. The deposition rate is monitored hourly using an optical profilometer. The stage I electrodeposition is terminated upon achieving the desired height for Level II (i.e., Group 2) electrodes.

To begin with Stage II of the electrodeposition process, the secondary circuit is disconnected from the primary circuit by removing the wire bond that shortens the secondary circuit switching pads. The MEA is again subjected to a short O_2 plasma treatment and is placed inside the electrochemical cell. Stage II electrodeposition is then initiated by applying a deposition current density of 8 mA/cm^2 to maintain the deposition rate. The electrodeposition process is monitored hourly and terminated upon realizing the desired height for Level III (i.e., Group 3) electrodes.

After achieving the desired heights for the electrodes, the KMPR mold removal process commenced. This involves gently stripping away the photoresist template layer, which uses the specialized mr-Rem 700 solution from MicroResist Technology. Under mild agitation, the solution effectively dissolves the photoresist template, allowing for easy removal while preserving the integrity of the fabricated structures. This meticulous step successfully unveiled the meticulously crafted 3D electrode array.

IV.5 Results and discussions

IV.5.1 Planar MEA device

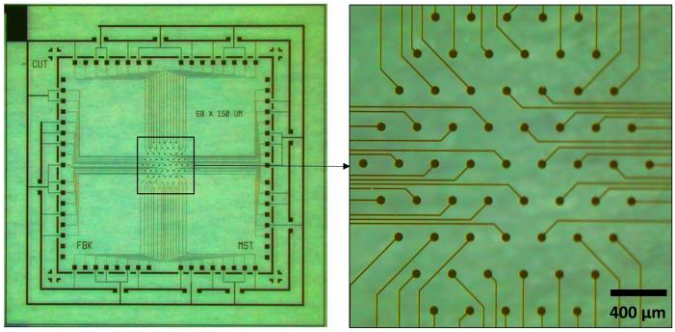

Figure IV - 8. Optical image of planar MEA device with external circuitry (Left) and a close-up image of the electrode array (right).

The fabrication process described previously resulted in the successful realization of planar gold microelectrodes arranged in an array formation on a glass substrate. Each microelectrode exhibited precise dimensions, with a diameter of 70 µm and a pitch of 265 µm, showcasing uniformity and accuracy in the layout. The

process yielded a positive rendition of the M1 mask layout pattern on chromium and gold layers on a pristine glass substrate (refer to Figure IV-8).

The second mask, M2, defined the passivation layer over the MEA chip, followed by pattern transfer using reactive ion etching, creating a robust passivation layer. Finally, the removal of the photoresist revealed partially passivated planar MEAs.

IV.5.2 Photoresist template characteristics

The photoresist template utilized in the fabrication process successfully meets all the key requirements essential for its effective functioning. With meticulous attention to detail, the template ensures dimensional precision, accurately defining the electrodes' diameter, and spacing across the array. This precision guarantees uniformity, enabling consistent electrode dimensions and spacing throughout the substrate. Structural integrity is maintained, as the template exhibits robustness against handling and subsequent processing steps such as electrodeposition and etching. Moreover, the template demonstrates excellent adhesion to the substrate, remaining securely in place throughout the fabrication process. Its compatibility with various chemicals and solvents used in fabrication ensures seamless processing without compromising structural integrity or performance. Overall, the photoresist template fulfills all requirements with excellence, serving as a reliable and precise mask for defining the electrode array's structure and facilitating the fabrication of high-quality microelectrode arrays.

The characterization of the generated photoresist template involved a comprehensive assessment using advanced optical microscopy and profilometry techniques to ensure accuracy and precision in the template's layout and dimensions. Optical microscopy was employed to capture high-resolution images of the template layout. This technique enabled the visualization of the entire array, verifying the uniformity and consistency of the well pattern across the substrate (refer to Figure IV-9a-b).

Optical profilometry was utilized to characterize the dimensions of the cylindrical wells, including their diameter and pitch(refer to Figure IV-9c-f). By scanning the surface of the template with a laser, profilometry generated precise topographical maps, allowing for the measurement of well dimensions with sub-micron resolution. This detailed analysis facilitated the assessment of dimensional accuracy and uniformity, ensuring that the wells met the desired width, depth, and spacing specifications.

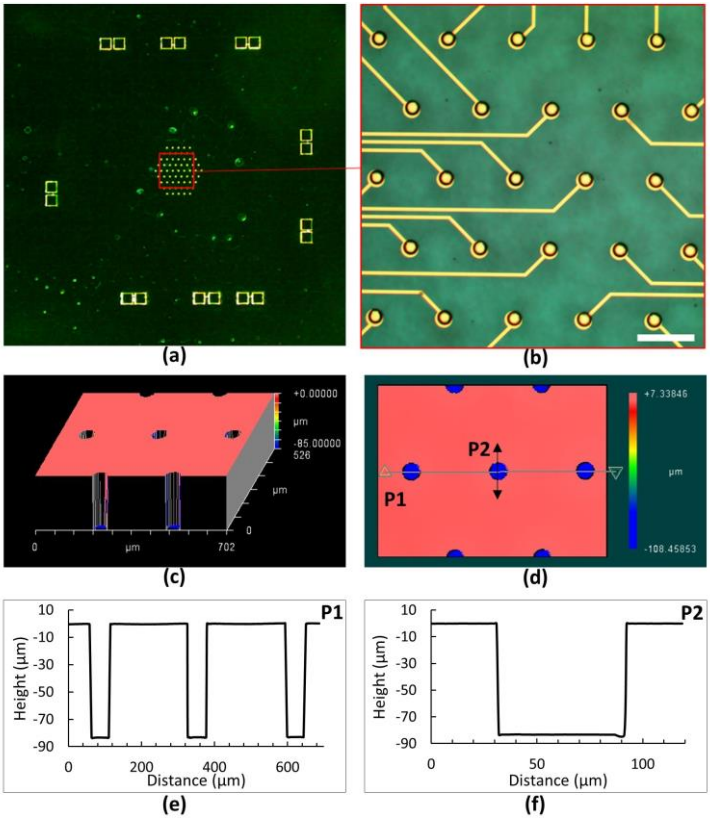

Figure IV - 9. Photoresist template characteristics. (a) Optical microscope image showcasing the layout of the photoresist template for an individual MEA device. (b) Optical image highlighting the array of cylindrical wells atop the planar electrodes (Scale bar: 200 µm). (c) A three-dimensional map representing a section of the cylindrical well array acquired using an optical profilometer. (d) The surface profile plot of the photoresist template featuring a color gradient indicating surface depth and profile extraction line segments P1 and P2. (e) Surface profile plot extracted along marker P1, providing insights into well depth, pitch, and profile characteristics. (f) Surface profile plot extracted along marker P2, offering detailed measurements of individual well dimensions.

The precise procedure resulted in the creation of a template featuring cylindrical wells, each measuring 60 µm in width and 83 µm deep, meticulously positioned atop the exposed planar electrodes with a center-to-center pitch of 265 µm (refer to Figure IV-9e-f).

IV.5.3 Multi-level 3D MEA characteristics

The characterization of the developed multi-level 3D MEA involves comprehensively assessing its structural features and topographical properties. Scanning Electron Microscopy (SEM) is employed to visualize the developed MEA, providing high-resolution images of the electrode array. These SEM images offer insights into the morphology and spatial arrangement of the multi-level electrodes across the array. The optical profilometer is utilized to characterize the 3D electrode heights, array topography, and the uniform distribution of multi-level electrodes across the array surface. This analysis involves obtaining surface profile maps of the MEA, which facilitates the measurement of electrode heights and the assessment of their distribution uniformity. Combining SEM imaging with optical profilometry, we thoroughly understand multi-level electrodes' topographical features and spatial distribution within the developed MEA.

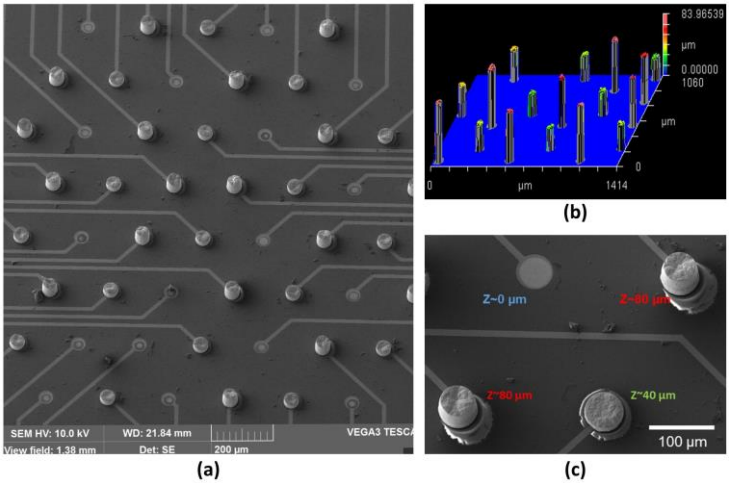

Figure IV - 10. Multi-level 3D MEA characteristics. (a) SEM image of the 3D MEA showing the uniform distribution of the multi-level electrodes across the array. (b) A 3D topographical plot of the 3D MEA presenting the multi-level electrodes' height distribution obtained using the optical profilometer. (c) SEM image from a section of the 3D MEA representing the three levels of the electrodes and their corresponding heights (Z).

Figure IV-10 presents the distribution of the multi-level electrodes across the MEA and the topographical distribution of the multi-level electrodes. It is evident from the SEM image that the fabricated multi-level 3D MEA consists of electrodes with three distinct height levels; the Group 1 electrodes remain planar as intended and are

present at flat circular pads on the substrate surface (refer to Figure IV-10a), and present the first Level (Level I) of the multi-level electrodes. The Group 2 electrodes, subjected only to Stage I electrodeposition, obtained a mean height of 39 µm while the Group 3 electrodes obtained a mean height of 79 µm (refer to Figure IV-10b). The electrode heights are represented by Z: the Level I electrodes have a height of ~0 µm, the Level II electrodes have a height of ~40 µm, and the Level III electrodes have a height of ~80 µm (refer to Figure IV-10c).

IV.5.4 Resistance characteristics of 3D gold electrodes

The resistance measurements were conducted on the gold 3D electrodes to investigate the change in resistance (ΔR) resulting from the transformation of planar electrodes to 3D configurations by performing double linear I-V sweeps. The measurement setup involved establishing electrical connections between the contact pad or readout pad and the apex of the 3D gold electrode and their planar counterparts. Specifically, five 3D electrodes with similar heights were carefully selected from each group for analysis. For instance, five electrodes from Group 2, characterized by a height of 40 ± 1 µm, were chosen, along with five electrodes from Group 3, which exhibited a height of 80 ± 1 µm. This selection process ensured consistency and enabled a reliable analysis between different electrode configurations.

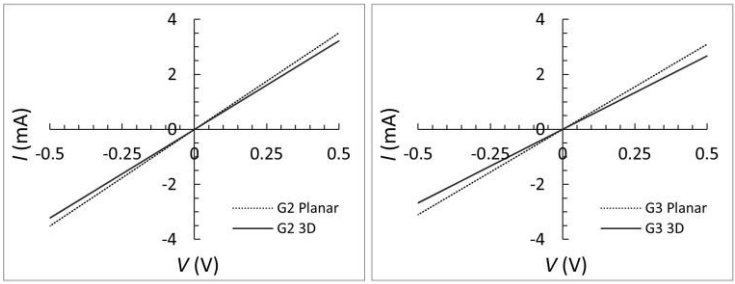

Figure IV - 11. IV characteristics of the 3D gold electrodes plotted against their planar counterparts. (a) IV characteristics of the Group 2 (G2) 3D gold electrodes plotted against its planar electrode IV characteristics measured before electrodeposition. (b) IV characteristics of the Group 3 (G2) 3D gold electrodes plotted against its planar electrode IV characteristics measured before electrodeposition.

The measurements were conducted between the contact pad and the top of the respective electrode. No significant change in resistance was observed for Group 1 (Level I) electrodes, which did not undergo electrodeposition. This outcome is consistent with expectations, as the electrodes remained in their planar configuration

throughout. The Group 2 (Level II) 3D electrodes exhibited an average increase in resistance of 12.7 Ω following electrodeposition. Similarly, Group 3 (Level III) 3D electrodes demonstrated an average increase in resistance, measuring 25.6 Ω post-electrodeposition. Notably, the change in resistance displayed a clear correlation with the height of the 3D gold electrodes, as expected.

IV.5.5 Platform's performance evaluation

As previously outlined, a batch comprising four planar MEAs connected to a single working electrode underwent the multi-stage electrodeposition process. The objective was to assess the technological platform's capacity for batch production of Multi-level 3D MEAs. The heights of all electrodeposited 3D electrodes across the four MEAs were measured using an optical profilometer to accomplish this goal. These measurements were systematically organized into groups for each MEA, enabling a thorough evaluation of the height distribution of the electrodes across the arrays (refer to Figure IV-12). The uniformity of the electrodeposited 3D electrode heights is also investigated by employing the percentage of standard deviation as a quantification parameter. This analysis provided valuable insights into the platform's capability for batch production, shedding light on the consistency and uniformity of electrode height distribution within and across the arrays.

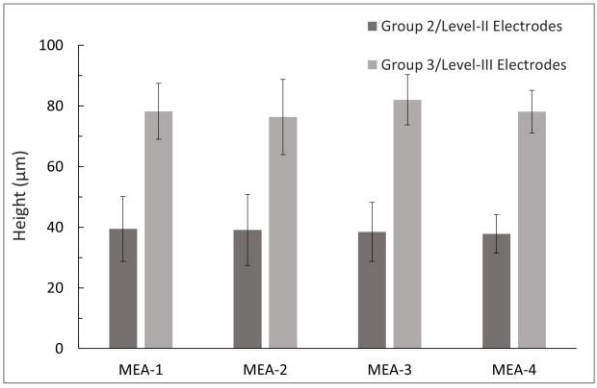

Figure IV - 12. Bar graph presenting the mean height of Level II and Level III 3D electrodes with percentage standard deviation across the mean height as the error bars.

Within the batch of four MEA devices, 72 Level II electrodes were subjected to electrodeposition solely through Stage I processes. The resulting 3D electrodes exhibited an average height of 38.69 µm, with a standard deviation of ±3.80 µm. Similarly, employing Stage II electrodeposition, 84 Level III electrodes were

electrodeposited. These Level III electrodes displayed an average height of 78.66 µm and a standard deviation of ±7.55 µm. This detailed characterization provides valuable insights into the electrodeposited structures' dimensional attributes, highlighting the batch's consistency and variability.

The mean heights recorded for the 3D electrodes corresponding to Level II and III across all four 3D MEAs align closely with the targeted heights of 40 µm and 80 µm, respectively. Despite this alignment, the uniformity assessment reveals a notable observation: the percentage standard deviation, employed as a measure of height uniformity, exhibits significant variability. This deviation extends up to 12% of the mean electrode height for both sets of electrodes. While precise control over individual electrode heights is achieved, the observed variation underscores the importance of enhancing uniformity across the array and batch of MEAs. Such uniformity is pivotal for developing customizable 3D MEAs, ensuring consistency and reliability in their performance across diverse experimental scenarios.

IV.6 Chapter highlights

- Introduction to Validation Process: Chapter 4 represents a crucial phase in the thesis, transitioning from conceptualization to tangible realization. The aim is to validate the proposed platform by translating theoretical frameworks into practical applications.
- Design and Layout: Meticulous planning and innovative engineering are evident in the design and layout of the MEAs. The layout encompasses eight 60-channel MEAs skillfully accompanied by external circuitry, demonstrating optimization for functionality, practicality, and scalability.
- Batch Processing Consideration: The layout emphasizes batch processing, with a single trace connecting external circuitry to optimize spatial utilization and manufacturing procedures. This design facilitates compatibility with existing readout platforms and enhances scalability.
- Individual Device Layout: Detailed descriptions of the layout for each mask layer are provided, outlining the arrangement of planar device architecture, passivation layer, and photoresist template. The layout design ensures precision and functionality while simplifying fabrication processes.
- Selective Electrodeposition Circuitry: The development and operation of custom circuitry for selective electrodeposition are elaborated. The circuitry layout enables multi-stage electrodeposition, allowing precise control over electrode configuration.
- Characterization of Photoresist Template: The photoresist template's characteristics are thoroughly analyzed, focusing on dimensional precision, structural integrity, and adhesion to the substrate. Optical microscopy and profilometry techniques are employed for accurate assessment.

- Characterization of Multi-level 3D MEA: SEM imaging and optical profilometry are utilized to assess the structural features and topographical properties of the developed multi-level 3D MEA. Detailed analyses reveal the uniform distribution and precise electrode dimensions.
- Resistance Characteristics of 3D Gold Electrodes: Resistance measurements are conducted to investigate the change in resistance resulting from electrodeposition. The results demonstrate a clear correlation between electrode height and resistance change.
- Platform's Performance Evaluation: The platform's capacity for batch production of multi-level 3D MEAs is evaluated, focusing on height distribution and uniformity. Despite achieving targeted heights, variability in height uniformity is observed, emphasizing the need for enhanced uniformity across arrays.

Chapter V: Optimizing platform performance by enhancing the deposition rate and uniformity in 3D MEAs

Part of this chapter has been published in:

Neeraj Yadav, Flavio Giacomozzi, Alessandro Cian, Damiano Giubertoni, and Leandro Lorenzelli,

"Enhancing the Deposition Rate and Uniformity in 3D Gold Microelectrode Arrays via Ultrasonic-Enhanced Template-Assisted Electrodeposition",
Sensors, 24 (2024) 1251.

V.1 Introduction

The development of advanced 3D microelectrode arrays necessitates the achievement of high electrodeposition rates to facilitate rapid prototyping and cost-effectiveness. In contrast, the uniformity of the thickness of the electrodeposited microstructures plays a pivotal role in defining the array's topography. However, conventional processes, particularly those involving template-assisted electrode processes, suffer from low deposition rates due to the localized depletion of ions in the electroplating solution, resulting in non-uniform deposition. Using ultrasonic baths, which employ high-frequency pressure waves to accelerate chemical reactions within liquid media, appears to be a promising solution to overcome the limitations of conventional electrodeposition processes. These baths are widely used in various industrial and laboratory applications, including cleaning, degreasing, and electroplating [173,174]. In recent years, ultrasonic baths have been proposed as a potential solution for accelerating the electrodeposition process, which is often limited by their low deposition rate. Sound waves generate microscopic cavitation bubbles in the liquid medium when an ultrasonic bath is employed for electrodeposition. These bubbles are subjected to intense pressure and temperature changes, forming highly reactive sites on their surface. These sites can then act as catalysts, accelerating the electrodeposition process [175,176]. Ultrasonic baths show great potential for application in electrodeposition. These baths can produce precise and uniform gold microstructures with high accuracy. Moreover, they can increase the deposition rate without requiring additional catalytic agents, reducing costs. Although the impact of ultrasonic agitation on the electrodeposition of two-dimensional structures has been widely investigated, its influence on template-assisted electrodeposition of three-dimensional microstructures is still not well understood [177–182].

In this chapter, we examine the impact of ultrasonic vibrations on the deposition rate and uniformity of microelectrode arrays created through template-assisted electrodeposition. Various characterization techniques, scanning electron microscopy (SEM), optical profilometry, and X-ray diffraction (XRD) analysis, were employed to evaluate the quality of the fabricated structures. The adhesion strength of the electrodeposited micropillars on a planar substrate was tested using a mechanical shear-strength testing tool. The results of this study contribute to a better understanding of the optimization of ultrasonic parameters for template-assisted electrodeposition and offer insights into improving the 3D MEA prototyping process. Additionally, this research has broader implications for applying ultrasonic agitation in other electrodeposition techniques used for micro- and nanofabrication.

V.2 Materials and methods

V.2.1 Materials

The experiments utilized an additive-free electroplating solution (AUROLYTE CN200, Atotech Deutschland GmbH & Co. KG, Berlin, Germany) for the electrodeposition process. A thick negative-type photoresist (KMPR-1035, Kayaku Advanced Materials, Inc., Westborough, MA, USA) was used for template fabrication. An ultrasonic bath (Sonorex Digitec DT 514 BH-RC, BANDELIN Electronic GmbH & Co. KG, Berlin, Germany) operating at a peak power of 640 W and 35 kHz was used for the experiments. A general-purpose galvanostat (GENERAL-PURPOSE POTENTIOSTAT MODEL: 2051, AMEL INSTRUMENTS, Milan, Italy) was utilized in this study. Remover PG (Kayaku Advanced Materials, Inc., Westborough, MA, USA) was used to remove the photoresist template after the electrodeposition. Three types of MEA substrates were developed: S1, S2, and S3.

V.2.2 Substrate layouts

V.2.2.1 S1 layout

The substrate S1 layout was a modification of the planar device architecture discussed previously in Chapter IV, with minor adjustments to the dimensions of the electrode pads. It comprised a hexagonal arrangement of 60 electrodes, each with a diameter of 65 µm and a pitch of 265 µm to ensure even distribution across the substrate. The active electrode count was twenty-one, and these were connected to a custom external circuitry designed outside the scribe line, designed explicitly for the electrodeposition experiments.

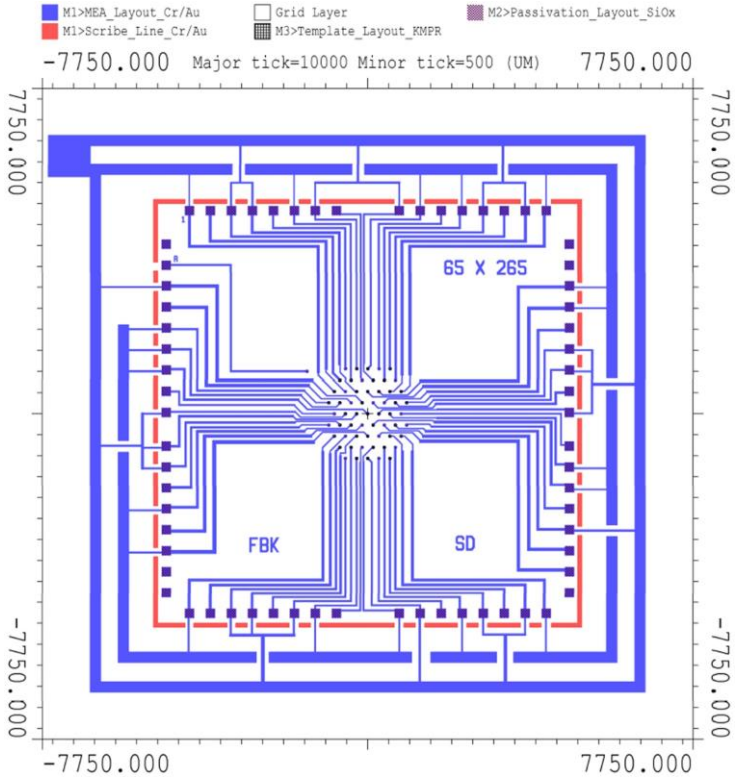

Figure V - 6. The scaled layout of the S1 MEA substrate.

Figure V-1 presents the three-layer design of the S1 substrate layout, which features a standard 60-channel MEA layout situated within the scribe line and an additional custom circuitry that connects 21 electrodes to the working electrode via the custom circuitry defined beyond the scribe line to facilitate electrodeposition. The layout comprises three mask layers: M1 shapes the planar architecture of the metal layer, M2 establishes the passivation layer for planar devices, and M3 creates the photoresist template.

V.2.2.2 S2 layout

The second substrate (S2) was designed with a MEA layout similar to that of the first substrate (S1), featuring a hexagonal arrangement of 60 electrodes with a diameter of 65 µm. However, S2 was modified to enhance its versatility for electrodeposition experiments. In particular, 41 of the 60 electrodes were connected to a custom routing system designed for electrodeposition applications. This modification enabled the

simultaneous electrodeposition of a greater number of electrodes, aiming to improve the uniformity and statistical analysis of the results.

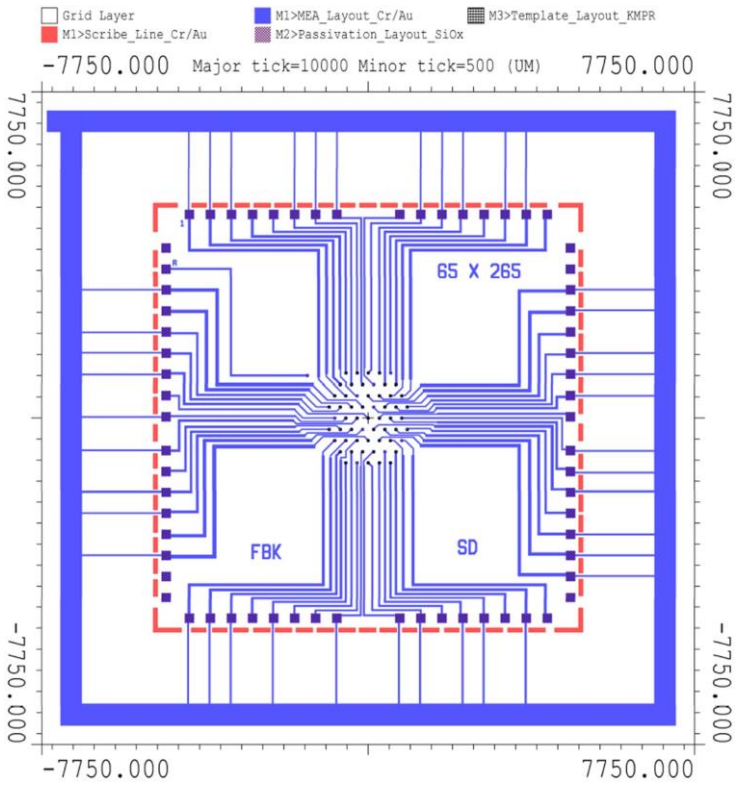

Figure V - 2. Scaled layout of S2 MEA substrate.

Figure V-2 presents the three-layer layout of the S2 substrate layout, featuring a three-layer configuration. The core component of this design was a standard 60-channel MEA layout located within the scribe line. Additionally, custom circuitry was incorporated to connect 41 electrodes to the working electrode, which was located outside the scribe line. This custom circuit is essential to enable successful electrodeposition.

V.2.2.3 S3 layout

Substrate S3 was specifically developed to evaluate the scalability and reproducibility of the optimal electrodeposition process using a precise and detailed design. It consisted of a hexagonal array of 60 electrodes that were carefully arranged for high-resolution electrodeposition. Each electrode had a smaller diameter of 35 µm and a

narrower pitch of 195 µm to achieve improved spatial resolution and fine detail in the resulting microstructures. It is worth mentioning that out of the 60 electrodes, 44 are connected to the working electrode via an external routing system.

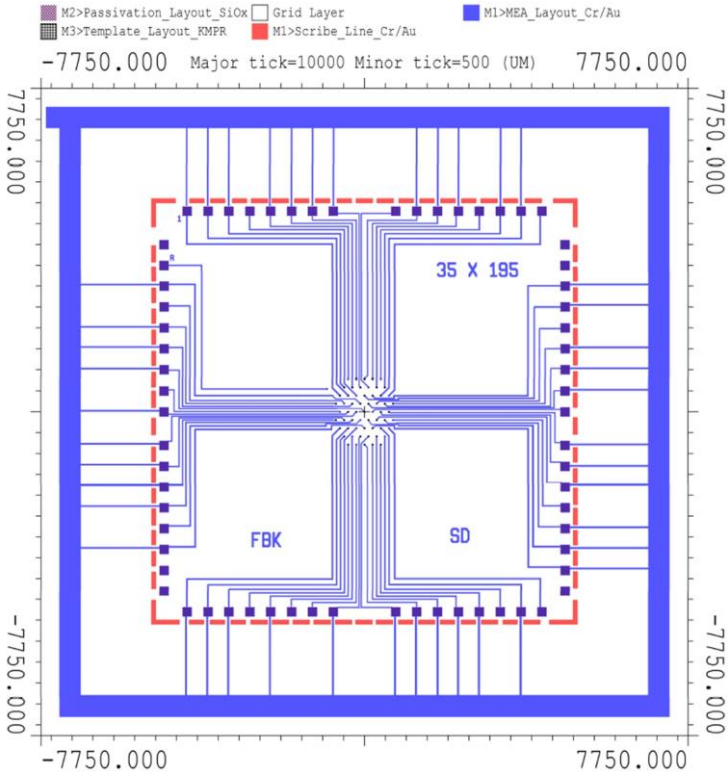

Figure V - 3. Scaled layout of S2 MEA substrate.

As depicted in Figure V-3, the S3 substrate comprises a three-layer arrangement featuring a conventional 60-channel MEA layout within the scribe line and an exclusive circuitry system that connects 44 electrodes to the working electrode through custom circuitry situated beyond the scribe line. This custom circuit was designed to facilitate the electrodeposition.

V.2.3 Substrate preparation

Custom-designed planar MEA substrates were developed for this study, and the design and fabrication protocols are outlined previously in Chapter III. The substrates were fabricated in a Class 1000 cleanroom using polished borosilicate

glass wafers (MicroChemicals GmbH, Ulm, Germany) as the base material. To initiate the fabrication process, a 10/200 nm thick Cr/Au layer was deposited onto a pristine glass wafer using an ultralow vacuum (ULVAC) metal evaporator. The wafer was primed through HMDS (Hexamethyldisilazane, MicroChemicals GmbH, Ulm, Germany) at 150 °C, followed by the application of a positive-tone photoresist (AZ® 1518 from MicroChemicals GmbH, Ulm, Germany) through spin coating and a pre-exposure bake at 100 °C.

The first photolithography step involved transferring the M1 pattern to the photoresist using an i-line mask aligner setup, followed by a standard post-exposure bake and subsequent photoresist development process. Pattern transfer from the photoresist to the metal layers was achieved through wet chemical etching of gold and chrome. The photoresist was removed using acetone, followed by a deionized (DI) rinse and drying cycle. The Cr/Au-patterned wafer was sintered at 200 °C for 60 min after the gold sintering. Subsequently, a 200 nm-thick passivation layer of SiO^2 was deposited using plasma-enhanced chemical vapor deposition (PECVD) technique.

The wafer was subjected to further lithography using the second mask (M2) to define the pattern on the photoresist, following a procedure similar to that previously described. Pattern transfer from the photoresist to the passivation layer was accomplished through a dry etching technique (AW-903ER Plasma Etch RIE, Allwin21 Corp., Morgan Hill, CA, USA), followed by a resist stripping process. The photoresist was removed, and the wafer was prepared for the final lithography step.

To create the template for the electrodeposition process, a wafer with planar MEAs was first coated with a layer of chemically amplified negative photoresist (KMPR-1035, Kayaku Advanced Materials, Inc., Westborough, MA, USA) measuring 110 µm in thickness. This was followed by a 30-minute soft-bake at 100 °C. The photoresist was then exposed to UV light through a third mask (M3) using an i-line mask aligner setup. Subsequently, the exposed area of the photoresist was cured completely through post-exposure baking at 100 °C for 6 min. Finally, the photoresist was developed using the SU-8 developer solution for 20 min, with the assistance of a shaker plate and mild agitation, to create a template with 110 µm deep cylindrical holes on top of the planar. This process resulted in forming an array of 110 µm deep, 65 µm diameter cylindrical holes strategically aligned over the planar electrodes for the S1- and S2-type MEAs. For the S3 MEA, the cylindrical wells had an internal diameter of 35 µm and a depth of 110 µm.

V.2.4 Experimental setup

All electrodeposition experiments were conducted in an ultrasonic bath maintained at 55 °C, as depicted in Figure V-4. Before initiating the gold electrodeposition for each experiment, the electroplating solution bath was conditioned for 1 h. The experiments were conducted in four phases. Experiment 1:

Electrodeposition of gold MEAs with a high current density (i.e., 8 mA/cm^2) for 1 h (H1) and various operational modes of the ultrasonic bath (i.e., no sonication mode (NS), pulsed sonication (PS) mode with a duty cycle of 50%, and continuous sonication (CS) mode) to investigate the influence of the ultrasonic bath operation mode on the deposition rate and electrode height uniformity across the array (refer to Figure V-4).

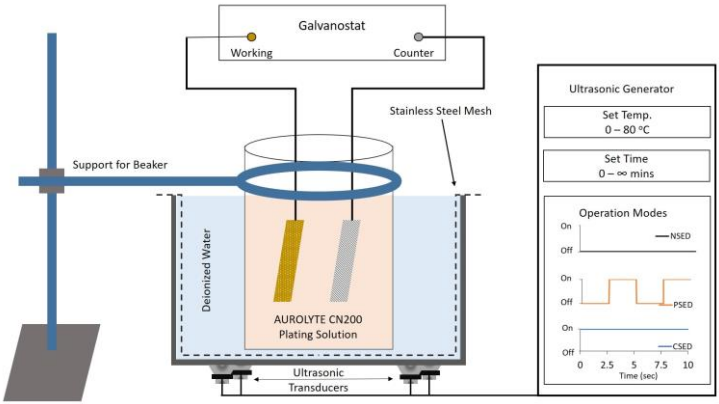

Figure V - 4. Schematic representation of the experimental setup including the various operational modes of the ultrasonic bath, i.e., NSED (electrodeposition without the ultrasonic vibrations), PSED (electrodeposition with ultrasonic vibrations in pulsed mode with a duty cycle of 50%), and CSED (electrodeposition with continuous ultrasonic vibrations).

Experiment 2 (L1): This was a repeat of Experiment 1 with a lower current density (4 mA/cm^2) to determine the influence of the deposition current density on the deposition rate and the uniformity of the electrode height. Experiment 3: The best electrodeposition parameters were selected from the previous experiments (i.e., CS-L1, based on the optimal deposition rate and the highest uniformity). In this case, the tests were repeated for longer durations of 2 and 3 h (i.e., CS-L2 and CS-L3, respectively) to verify the consistency of the process. Finally, a fourth experiment was conducted to verify the scalability of the process for the deposition of high-density (HD) MEAs for long durations. For the first two experiments, the S1 MEAs with 21 active electrodes were subjected to template-assisted electrodeposition for 1 h. For the third experiment, the S2 MEAs with 41 active electrodes were subjected to template-assisted electrodeposition for 2 and 3 h, and the experiment was repeated to ensure reproducibility. S3 MEAs were used in the fourth experiment by subjecting them to template-assisted electrodeposition for 4 h. The experimental details are listed in **Table V-1**.

Table V-1. Design of experiments. List of experiments performed under various conditions.

Experiment No.	Sample Name	MEA Type	No. of Active Electrodes	Electrode Diameter (µm)	Deposition Current Density (mA/cm²)	Electrodeposition Duration (minutes)	Ultrasonic Bath Mode *
Experiment 1	NS-H1	S1	21	65	8	60	NS
	PS-H1	S1	21	65	8	60	PS
	CS-H1	S1	21	65	8	60	CS
Experiment 2	NS-L1	S1	21	65	4	60	NS
	PS-L1	S1	21	65	4	60	PS
	CS-L1	S1	21	65	4	60	CS
Experiment 3	CS-L2	S2	41	65	4	120	CS
	CS-L3	S2	41	65	4	180	CS
	CS-L2 r **	S2	41	65	4	120	CS
	CS-L3 r	S2	41	65	4	180	CS
Experiment 4	CS-L4 (HD)	S3	44	65	4	240	CS

* Ultrasonic bath modes: NS—ultrasonic vibrations OFF, PS—ultrasonic vibrations ON in pulsed mode, and CS—ultrasonic vibrations ON continuously. ** Repeated.

V.2.5 Analysis

A scanning electron microscope (SEM) was used to assess the process yield, which refers to the number of electrodeposited micro-pillars divided by the number of electrodes subjected to electrodeposition for each MEA. A two-step process was employed to determine the electrodeposition rate and uniformity. Initially, an optical profilometer was used to measure the height of the electrodeposited micro-pillars, which were then subjected to electrodeposition for one hour. The heights of multiple micro-pillars sourced from different regions of the MEA were comparatively analyzed to evaluate the height uniformity of the electrodeposited micro-pillars.

To evaluate the mechanical properties of the electrodeposited micro-pillars, particularly their shear strength, a destructive die shear strength test was performed using the Condor Ez Pull&Shear test tool from XYZtec (refer to Figure V-5a). In the first experiment, five micro-pillars were randomly chosen from each experimental condition and subjected to a shear test at room temperature. A constant-velocity shear tool, moving at a speed of 2 µm/s, was placed in contact with the side of the micro-pillar until either fracture or splitting occurred (refer to Figure V-5b). To obtain a reliable measure of the adhesion strength at the pillar-substrate interface, it was ensured that failure occurred at the pillar-substrate interface by positioning the shear tool 1 µm above the substrate surface. The maximum force exerted by the tool at the point of failure was recorded for all five measurements from each MEA. From the mean

maximum shear force and its standard deviation, the maximum shear strength τ_{max} was calculated from the maximum shear force F_{max} using the following equation[183]:

$$F_{\max} = \tau_{\max} \cdot A \quad (1)$$

where A is the cross-sectional area of the pillar, obtained from the measured pillar diameter.

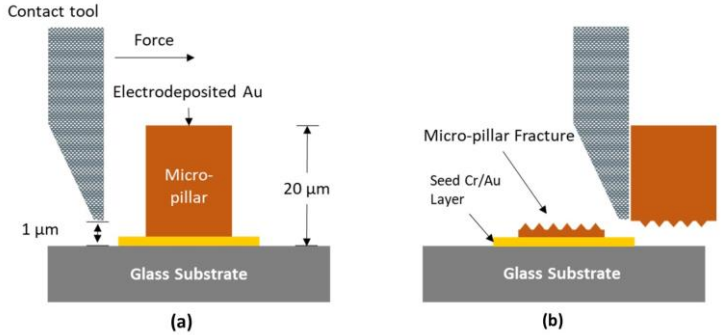

Figure V - 5. Illustration of the shear test setup. (a) Initial position of the contact tool, (b) final position of the contact tool.

To investigate the impact of ultrasonic vibrations on the morphological features of the electrodeposited gold microstructures, three distinct samples were prepared. Glass wafer pieces (17 × 17 mm^2) that had been coated with a 5 nm layer of chromium (Cr) and 200 nm of gold (Au) deposited via the thermal evaporation process were employed as substrates (refer to Figure V-6). The substrates were covered with 70 µm-thick Kapton tape, which had a circular opening with a diameter of 6 mm. The masked substrates were subjected to electrodeposition using parameters from the first experiment. The first substrate was subjected to electrodeposition for 1 h without ultrasonic vibrations, that is, in the absence of ultrasonic vibrations (NSED). The second substrate was subjected to electrodeposition with an ultrasonic bath operating in pulsed sonication mode for one hour, that is, PSED. Finally, the third substrate was subjected to electrodeposition for 1 h under continuous sonication mode, that is, CSED. The effect of ultrasonic vibrations on the morphology of the electrodeposited gold films was determined by measuring the surface roughness using atomic force microscopy (AFM; PX, NT-MDT SI, Moscow, Russia).

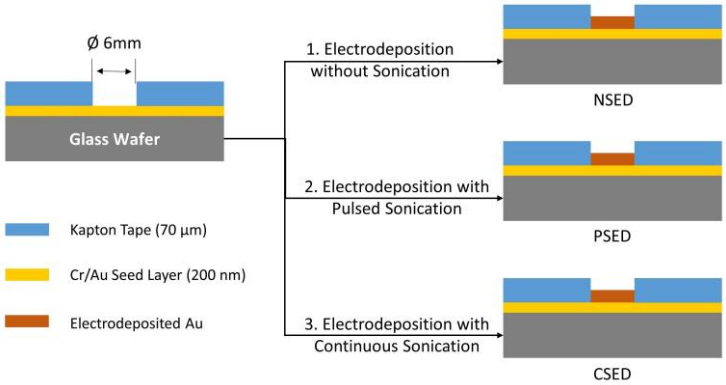

Figure V - 6. Schematic representation for preparation of the samples for the structural and morphological characterizations.

The impact of ultrasonic vibrations on the structural characteristics of the electrodeposited samples was investigated via X-ray diffraction (XRD) analysis using a high-resolution XRD instrument (ITALSTRUCTURES APD2000, Austin AI, Austin, TX, USA). The NSED, PSED, and CSED samples and the substrate with the seed layer were examined to evaluate the effect of ultrasonic vibrations on the crystal phase of the electrodeposited structures. The average grain size *D* was determined via XRD for multiple crystallographic planes, including (111), (311), (220), and (200), via Scherrer equation:

$$D = K \cdot \lambda / (\beta \cdot cos(\theta)) \quad (2)$$

where the Scherrer constant *K* is typically taken as 0.94 [183], λ = 1.5418 Å is the wavelength of the Cu Kalpha radiation employed for the XRD, β is the full-width at half-maximum (FWHM) of the measured peak in radians, and theta is the Bragg angle at which the peak occurs.

V.3 Results and discussions

V.3.1 Deposition rate and uniformity

The deposition rate and uniformity are critical attributes in the template-assisted electrodeposition process. An optical profilometer was utilized to measure the height of the electrodeposited micro-pillars across each array to derive the deposition rate and assess the uniformity of the height of the electrodeposited micro-pillars. The uniformity in electrode heights across the array was calculated by normalizing the electrode heights and comparing the distribution for each case (refer to Figure V-7). In the first experiment, the S1 MEAs were subjected to electrodeposition for 1 h at a high current density of 8 mA/cm^2 (H1) under different operational modes of the ultrasonic bath. The MEA subjected to electrodeposition without ultrasonic vibrations (i.e., NS-

H1) displayed a deposition rate of 0.10 µm/min and a standard deviation of 35.8%. This indicated a low deposition rate compared to standard electrodeposition without using a template under similar experimental conditions (i.e., ~0.45 µm/min) and a considerable variation in micro-pillar heights across the array, revealing a lack of uniformity. The MEA subjected to electrodeposition with pulsed ultrasonic vibrations (i.e., PS-H1) showed an improved deposition rate of 0.24 µm/min, with a standard deviation of 16.19%, suggesting an improved uniformity compared to that of NS-H1. Finally, the MEA subjected to electrodeposition with continuous ultrasonic vibrations (i.e., CS-H1) demonstrated the highest deposition rate of 0.55 µm/min, with a standard deviation of 13.52%, indicating greater consistency in the micropillar heights and enhanced uniformity.

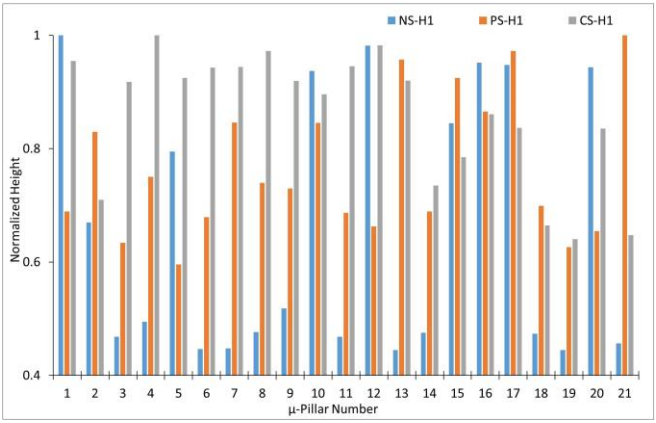

Figure V - 7. Normalized height distribution of electrodes/micro-pillars for each MEA from Experiment 1. The bar graph clearly indicates that the use of ultrasonic vibrations during electrodeposition (i.e., PS-H1 and CS-H1) significantly improves the uniformity in the height distribution of the micro-pillars compared to the MEA subjected to electrodeposition without ultrasonic vibrations (i.e., NS-H1).

In the second experiment, the S1 MEAs were subjected to electrodeposition for 1 h with a lower current density of 4 mA/cm^2 (L1) under different operational modes of the ultrasonic bath. To evaluate the rate of deposition and uniformity, an optical profilometer was used to measure the height of the electrodeposited micro-pillars across each array, which allowed for the calculation of the deposition rate and assessment of the uniformity of the electrode heights (refer to Figure V-8). The MEA subjected to electrodeposition without ultrasonic vibrations (i.e., NS-L1) showed a deposition rate of 0.06 µm/min proportional to NS-H1 and a percentage standard deviation of 14.77%, indicating a considerable improvement in the uniformity. The MEA subjected to electrodeposition with pulsed ultrasonic vibrations (i.e., PS-L1) showed an improved deposition rate of 0.13 µm/min compared to NS-L1. However,

the experiment revealed a slight increase in the percentage standard deviation (i.e., 16.15%) with respect to NS-L1. Finally, the MEA subjected to electrodeposition with continuous ultrasonic vibrations and lower deposition current (i.e., CS-L1) showed a deposition rate of 0.24 μm/min and also a further decrease in the percentage standard deviation to 9.63%, indicating more consistency in the micro-pillar heights, and therefore an improved uniformity.

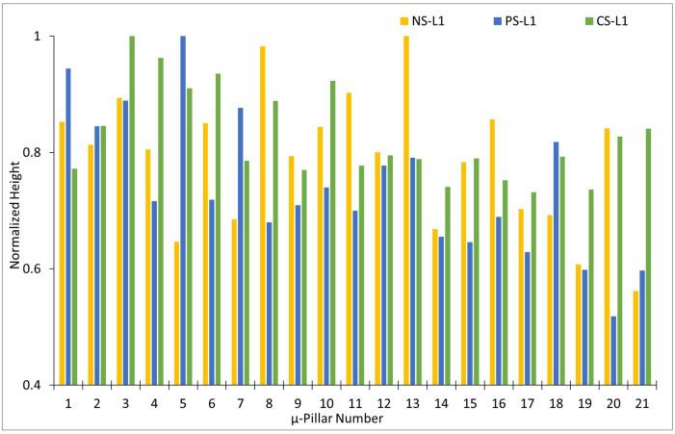

Figure V - 8. Normalized height distribution of electrodes/micro-pillars for each MEA from Experiment 2. The bar graph indicates that using the lower current density for electrodeposition leads to a slight improvement in the uniformity even without the use of ultrasonic vibrations (i.e., NS-L1), and the use of ultrasonic vibrations further enhances the uniformity (i.e., PS-L1 and CS-L1).

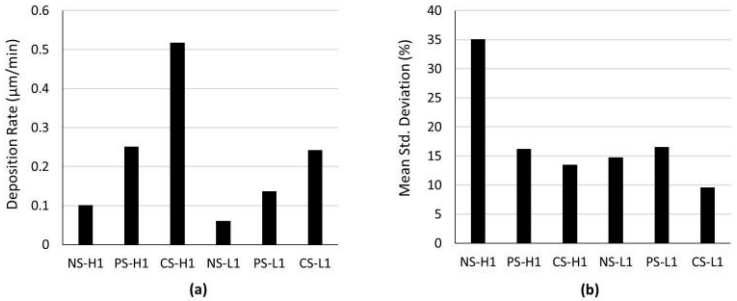

Figure V - 9. Bar graphs comparing the deposition rate and the percentage mean standard deviation across the height of the electrodeposited micro-pillar array (as a measure of uniformity) for the various experiments. (a) Comparison of the deposition rate of the different microelectrode arrays (MEAs) from the first (H1) and the second (L1) experiment. (b) Comparison of the percentage mean standard deviation in the thickness of 21 electrodeposited micro-pillars for each MEA in the first and second experiment.

The first experiment confirmed that the incorporation of ultrasonic vibrations significantly enhanced the deposition rate and promoted uniformity. A high deposition rate is generally considered advantageous; however, uniformity is essential for the development of MEAs. The second experiment illustrated a decrease in the deposition rate compared to the first experiment; this reduction was proportional to the applied deposition current density across all three cases (refer to Figure V-9a). The CS-L1 sample exhibited the lowest percentage standard deviation, signifying the highest uniformity when compared with all the other samples from the first and second experiments (refer to Figure V-9b). In light of these results, continuous sonication with a low current density was deemed the optimal combination for additional investigations.

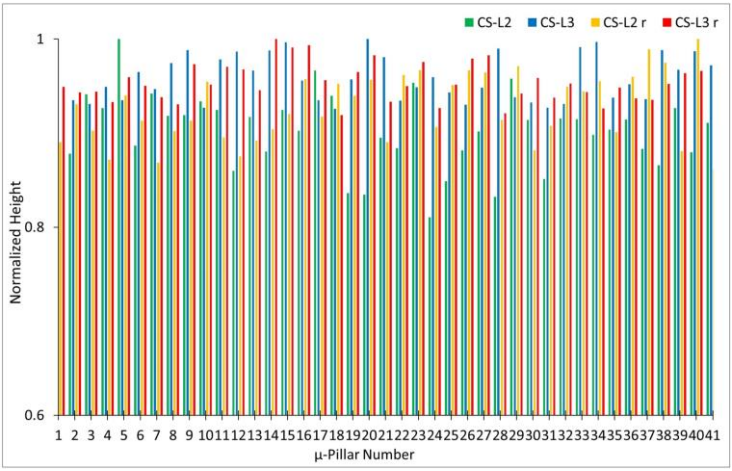

Figure V - 10. Normalized height distribution of electrodes/micro-pillars for each MEA from Experiment 3. The bar graph indicates that the longer electrodeposition durations with the use of continuous ultrasonic vibrations also contribute to an enhancement in uniformity.

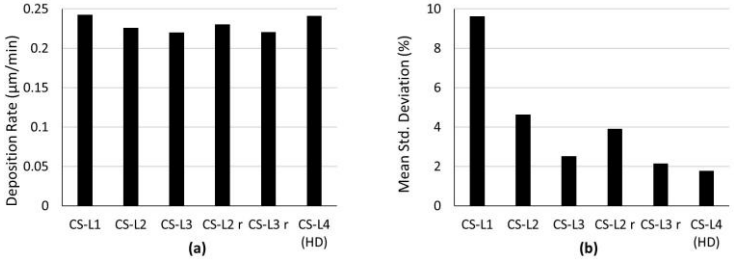

Figure V - 11. Bar graphs comparing the deposition rate and the percentage mean standard deviation across the height of the electrodeposited micro-pillar array (as a measure of uniformity) for the various experiments. (a) Comparison of the deposition rate of the various microelectrode arrays (MEAs) from the second (CS-L1), third (CS-L2, CS-L3, CS-L2 r, and CS-L3 r), and fourth (CS-L4 (HD)) experiments. (b) Percentage mean standard deviation pertaining to each sample

from the second (CS-L1), third (CS-L2, CS-L3, CS-L2 r, and CS-L3 r), and fourth (CS-L4 (HD)) experiments.

In the third experiment, two sets of S2 MEAs comprising 41 active electrodes each underwent template-assisted electrodeposition for 2 h and 3 h using continuous sonication with a low current density. These were labeled as CS-L2 and C3-L3, respectively. To ensure reproducibility, the same procedure was repeated, resulting in repetition of the experiment, which was then referred to as CS-L2 r and C3-L3 r. The height of the electrodeposited micro-pillars across each array were measure using an optical profilometer, which allowed the assessment of the uniformity of the electrode heights (refer to Figure V-10). The deposition rates achieved in CS-L2 and C3-L3 were comparable to those of CS-L1 but slightly lower, with C3-L3 having the lowest deposition rate. These trends were confirmed by repeating the experiment (refer to Figure V-11a).

The decrease in the deposition rate observed for longer deposition times could be attributed to the depletion of gold ions in the electroplating solution. However, this conclusion is based on the experimental setup, and further studies are required to fully understand this phenomenon. Conversely, the percentage standard deviation for the CS-L3 experiment decreased significantly to 2.13% as the electrodeposition duration increased (refer to Figure V-11b).

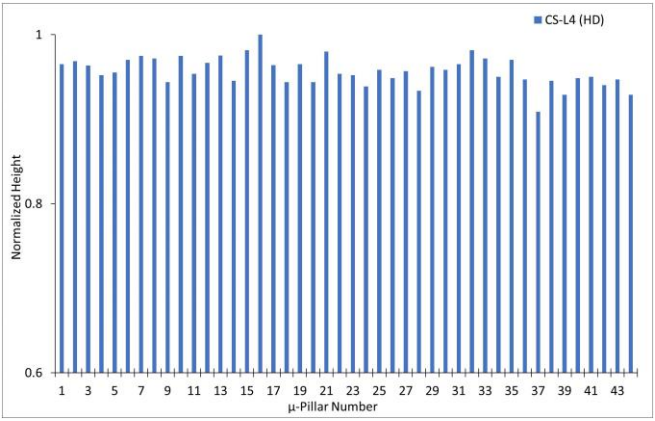

Figure V - 12. Normalized height distribution of electrodes/micro-pillars for each MEA from Experiment 4. The experiment was conducted to check the scalability (in terms of higher aspect ratios of the micro-pillars/template) of the process using a high-density MEA subjected to ultrasonic-vibration-assisted electrodeposition for a long duration (i.e., CS-L4 (HD)). The bar graph demonstrates the scalability of the process.

Finally, the fourth experiment was carried out by subjecting an HD MEA (S3) to template-assisted electrodeposition for 4 h (i.e., CS-L4 (HD)) with continuous ultrasonic vibrations and a current density of 4 mA/cm2. The hSeights of the electrodeposited micro-pillars were measured and analyzed (refer to Figure V-12). The

experiment yielded a deposition rate of 0.24 µm/min comparable to the results of previous experiments (refer to Figure V-11a). Additionally, the experiment demonstrated the lowest standard deviation of 1.76%, indicating exceptional uniformity (refer to Figure V-11b).

These results indicate that incorporating ultrasonic assistance, particularly in the continuous mode, significantly increases the deposition rates in template-assisted electrodeposition. Additionally, a lower deposition current density enhances the uniformity of the electrode height across the array (refer to Figure V-13). The empty circular sites in the SEM images represent the planar electrodes that were not subjected to electrodeposition (refer to Figure V-13). All MEAs that underwent electrodeposition exhibited a 100% deposition yield (i.e., the number of micro-pillars deposited divided by the number of electrodes subjected to electrodeposition). This finding could be a critical strategy for optimizing the deposition parameters when precise control over micro-pillar dimensions and uniformity is essential.

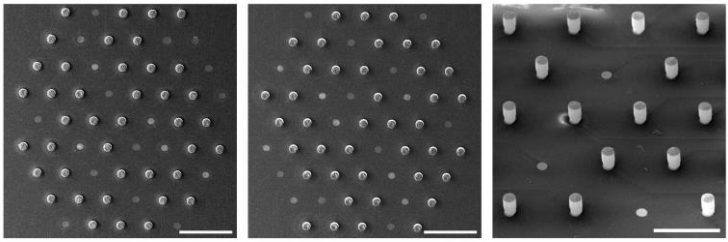

Figure V - 13. SEM images of the MEAs. (a) CS-L2 with a tilt of 10 degrees (scale: 500 µm). (b) CS-L3 with a tilt of 10 degrees (scale: 500 µm). (c) CS-L4 (HD) with a tilt of 25 degrees (scale: 200 µm).

V.3.2 Mechanical strength

This study evaluated the crucial parameters of the mechanical strength of electrodeposited micro-pillars to investigate the impact of ultrasonic vibrations on their shear strength. A destructive shear stress test was conducted to determine the maximum shear force the micro-pillars could withstand before failure (refer to Figure V-2). The test was conducted on three MEAs from the first experiment and the HD MEA from the fourth experiment.

For the NS-H1 MEA, the highest shear force recorded was 0.610 N, with a standard deviation of 6.58%. The PS-H1 MEA showed slightly greater resistance, reaching a maximum shear force of 0.707 N, and displayed a lower standard deviation of 3.57%, indicating a slightly superior and more consistent shear strength compared to NS-H1. The CS-H1 MEA exhibited a similar mean maximum shear force to that of

the NS-H1 MEA at 0.636 N, but with a reduced standard deviation of 3.38%, suggesting greater uniformity in shear strength during this process.

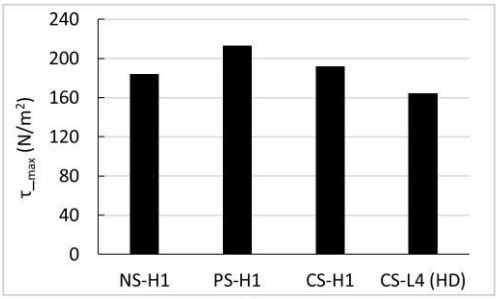

(a)

(b)

Figure V - 14. Shear strength analysis. (a) Bar chart presenting the average (n = 5) of the maximum shear strength τ_{max} faced by the micro-pillars before failure for each MEA subjected to the test. (b) A microscopic image of the CS-L4 (HD) MEA undergoing the shear test with the contact tool at the initial position.

The shear force resistance of the CS-L4 (HD) MEA was significantly lower at 0.158 N, with a standard deviation of 3.62%. However, it should be noted that the cross-sectional area of the micro-pillars in the CS-L4 (HD) MEA was 3.5 times smaller than that of the other three methods. Given that the shear strength is directly proportional to the cross-sectional area, the seemingly weaker shear strength in the CS-L4 (HD) MEA is not indicative of poor shear resistance but rather a consequence of a smaller cross-sectional area. When adjusting for the reduced cross-sectional area, the actual shear strength of the CS-L4 (HD) MEA was comparable to that of the CS-H1 MEA (refer to Figure V-14a). This suggests that a lower current density in continuous ultrasonic bath-assisted electrodeposition with a lower deposition rate does not necessarily compromise the shear strength. The findings of this research have important implications for the design of electrodeposition processes for gold

microstructures that require strong resistance to shear forces on the substrate. Figure V-14b shows an optical image of the shear strength measurement setup with the contact tool at the initial measurement position for the CS-L4 (HD) MEA.

V.3.3 Structural and morphological Analysis

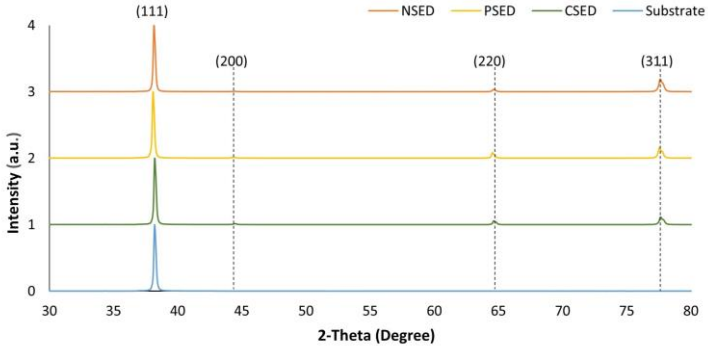

Figure V - 15. Measured XRD patterns of the electrodeposited gold (without template) under different ultrasonic vibration modes and the thermally evaporated gold seed layer (i.e., substrate).

Figure V-15 shows a Y-stacked plot of the X-ray diffraction (XRD) spectra for the three electrodeposited gold samples (i.e., NSED, PSED, and CSED) and the substrate with the gold seed layer (substrate) deposited using the thermal evaporation technique. As expected, the seed layer exhibits a crystalline structure with a single peak at 38.2 degrees (i.e., the (111) plane). In the case of the electrodeposited samples, strong peaks were observed in the (111) plane, and weaker peaks were observed in the (311), (220), and (200) planes, indicating a polycrystalline structure. No significant shift in the 2theta locations in the XRD spectra was observed for the various electrodeposited gold samples. As shown in Table V-2, the full width at half maximum (FWHM) of the (111), (311), (220), and (200) planes is highest for the NSED sample and lowest for the PSED sample, indicating a lower surface roughness and average grain size compared to those of the PSED and CSED samples, which can also be observed in the atomic force microscopy (AFM) images (refer to Figure V-16).

Table V-2. Full width at half maximum (FWHM) of 111, 311, 220, and 200 peaks of electrodeposited gold.

Sample	(111) [1]	(311)	(220)	(200)	Average Grain
	FWHM	FWHM	FWHM	FWHM	Size (nm)
Substrate	0.20524	-	-	-	40.96
NSED	0.15433	0.25735	0.21134	0.23835	43.63

PSED	0.14565	0.2244	0.1736	0.23286	48.51
CSED	0.14751	0.23751	0.18359	0.2303	47.01

[1] Crystallographic plane.

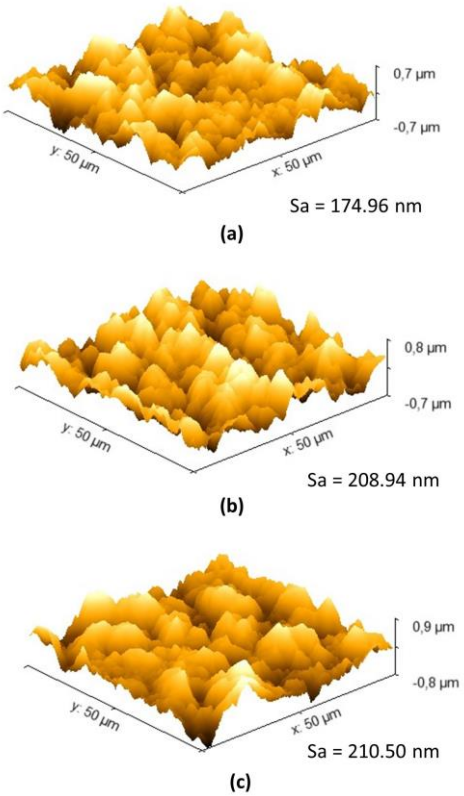

Figure V - 16. AFM 3D image and average surface roughness (Sa) of (a) NSED, (b) PSED, and (c) CSED.

V.3.4 Implications for 3D MEAs

This research indicates that using ultrasonic bath-assisted electrodeposition, particularly under continuous operation (CSED and LC-CSED), significantly enhances the performance of template-assisted electrodeposition. This could potentially lead to higher quality three-dimensional micro-electrode arrays (3D MEAs), resulting in an increased deposition rate, improved uniformity, and stronger adhesion of gold micro-pillars. These findings may also contribute to optimizing ultrasonic parameters in electrodeposition processes, which could advance the field of microfabrication and

nanofabrication. Our results emphasize the promising potential of ultrasonic bath-assisted electrodeposition for fabricating 3D MEAs. Future studies could further validate these findings by exploring other factors that impact the electrodeposition process and optimizing them to achieve superior MEA performance.

V.4 Chapter highlights

- Effects of Ultrasonic Vibrations: This study investigates the effects of ultrasonic vibrations on template-assisted electrodeposition of gold micro-pillars for constructing 3D microelectrode arrays (MEAs) for *in vitro* electrophysiological studies.
- Increased Deposition Rate: Continuous ultrasonic bath-assisted electrodeposition led to a significant increase in the deposition rate, enhancing the efficiency of the fabrication process for 3D MEAs.
- Improved Uniformity: Ultrasonic vibrations improved the uniformity of the micro-pillar height across the array, ensuring consistency and reliability in the fabricated MEAs.
- Role of Deposition Parameters: The study highlighted the critical role of deposition time and current density in achieving uniformity, providing insights into optimizing deposition parameters for enhanced MEA fabrication.
- Guidance for Optimization: The findings offer valuable guidance for optimizing the parameters of ultrasonic bath-assisted electrodeposition, facilitating advancements in micro- and nanofabrication techniques.

Chapter VI: Design development and performance evaluation of variable height 3D MEAs

Part of this chapter has been published in:

Neeraj Yadav, Donatella Di Lisa, Flavio Giacomozzi, Alessandro Cian, Damiano Giubertoni, Sergio Martinoia, and Leandro Lorenzelli,

"Development of multi-depth probing 3D microelectrode array to record electrophysiological activity within neural cultures",
J. Micromech. Microeng., 33 (2023) 115002.

VI.1 Introduction

This chapter presents the development and functional characterization of 3D MEAs with four distinct electrode heights. Four distinct electrode heights were achieved by reengineering the device layout to accommodate the optimized layout of the circuitry, enabling a three-stage electrodeposition process. An ultrasonic-enhanced template-assisted electrodeposition process was utilized to attain precise control over the height of the 3D electrodes. Moreover, the overall technological platform was optimized by eliminating the use of wire bonding for circuit manipulation and reconfiguring the device layout to utilize wet chemical etching for this purpose. The fabricated 3D MEA devices were characterized using optical profilometry and scanning electron microscopy (SEM) to evaluate the height and distribution of the microelectrodes within the array. Additionally, electrochemical impedance spectroscopy provides valuable information about the performance of the individual electrodes.

Based on the varying heights of the microelectrodes, the sensing electrodes were categorized into four distinct groups (G1, G2, G3, and G4). To assess the device's functionality, bare electrode noise measurements were taken using the MEA2100 System from MultiChannel Systems (MCS), and spontaneous electrophysiological activity was recorded. Moreover, we evaluated the device's performance by recording spontaneous electrophysiological activity from a three-dimensional human neurospheroid derived from the differentiation of human Induced Pluripotent Stem Cells (h-iPSCs), utilizing the MCS commercial setup.

Furthermore, a comparative analysis was conducted between the developed multi-height 3D MEA (designated as MH-MEA) and a state-of-the-art 3D MEA (referred to as 3D MC) comprising 60 titanium nitride microelectrodes, each with a single-level height of 100 µm and pitch of 250 µm, supplied by MCS. The comparison was conducted under similar experimental conditions to ensure consistency.

The technology presented in this work enables the development of 3D MEAs compatible with the most commonly used *in vitro* recording system (MEA2100-System from MultiChannel Systems). Customizing electrode arrays makes these devices suitable for various applications, such as studying neuronal network dysfunction, neurotoxicity, drug screening, or other electrical measurements with organoids based on electroactive cells.

VI.2 Design and layout optimizations

VI.2.1 MEA batch layout

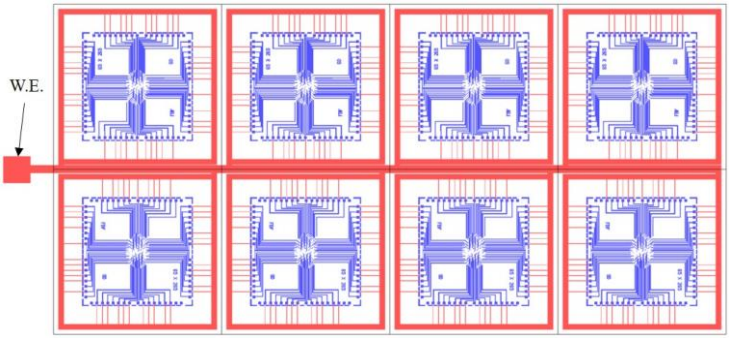

Figure VI - 7. Wafer-scale layout illustrating a batch of eight planar MEA devices (layout colored blue) with custom circuitry to support electrodeposition connected to a single working electrode (layout colored red).

At the wafer scale, the layout of the device comprises eight 60-channel MEAs, each connected to external circuitry via a single trace designed to serve as a common working electrode during electrodeposition (refer to Figure VI-1). The overall MEA layout is similar to that described in Chapter III. However, the circuitry has been re-engineered to facilitate the multi-stage electrodeposition process and manipulate the circuit accordingly.

VI.2.2 Individual device layout

Each device consisted of an array of 60 planar electrodes, measuring 65 µm in diameter and arranged in a hexagonal pattern with a 265 µm pitch. The electrodes were connected to contact pads via internal routing (refer to Figure VI-2a), and the contact pads were connected to an outer metal ring through custom routing, which served as the working electrode for the selective application of the electrodeposition current (refer to Figure VI-5b). The planar electrodes were divided into four distinct groups through external circuitry routing: group G1, which comprises electrodes not

connected to external circuitry, and groups G2, G3, and G4, which are connected to external circuitry to support multi-stage electrodeposition.

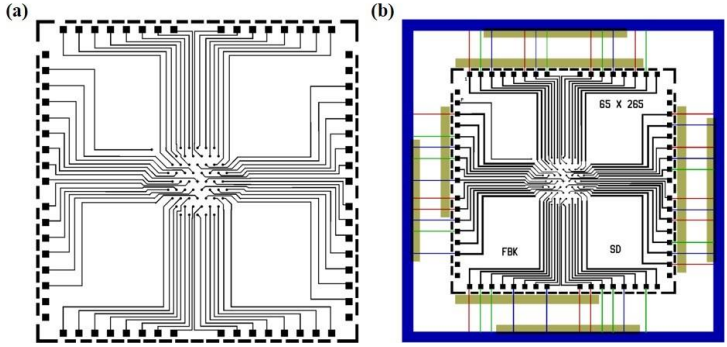

Figure V - 2. Individual device design and layout. (a) 10 X 10 mm^2 60-channel MEA device layout consisting of sensing electrode pads in the center and contact pads for the readout system on the periphery of the device connected through internal routing. (b) Contact pads connected to an outer metal ring (colored blue) outside the MEA device periphery via custom external routing to support selective electrodeposition using a single working electrode, the dark yellow rectangles represent the etching windows in the photoresist template.

The layout consists of three mask layers. The first mask (M1) transfers the MEA layout onto a gold metal layer on the wafer. The second mask (M2) defines openings in the passivation layer, exposing the electrodes and contact pads. This mask also incorporated etching windows on the external routing to facilitate disconnection from the metal ring during electrodeposition. The final mask(M3) defines the layout to form a photoresist template for the electrodeposition of gold micro-pillars onto the G2, G3, and G4 electrodes, which is achieved by creating cylindrical wells in the photoresist.

VI.3 Materials and methods

VI.3.1 Fabrication of multi-height 3D MEA

VI.3.1.1 Definition of planar device architecture

The fabrication process was carried out in a Class 1000 cleanroom, utilizing 150 mm polished borosilicate glass wafers sourced from Plan Optik AG, Germany. The wafers were coated with a 10/200 nm thick Cr/Au layer using an ultralow vacuum electron beam evaporator (ULVAC). Subsequently, the wafers were primed with hexamethyldisilazane (HMDS) at 150 °C to enhance photoresist adhesion. Following this process, a positive-tone photoresist (OIR 305-20HC from Fujifilm) was spin-coated onto the wafer and baked at 100 °C. The pattern was then transferred from photolithography mask M1 to the photoresist using an i-line mask aligner (KARL SUSS MA6), followed by standard post-exposure bake and photoresist development. Subsequently, the unmasked gold and chrome layers were etched using wet chemical

etching, thereby completing pattern transfer. The photoresist was then stripped using acetone, and the wafer was sintered at 200 °C for 60 minutes. Finally, a 200 nm thick silicon dioxide passivation layer was deposited using PECVD. The opening on the oxide layer was defined using the photolithography mask M2, and the electrode and contact pads were exposed via dry etching (TEGAL 903) (refer to Figure VI-3a).

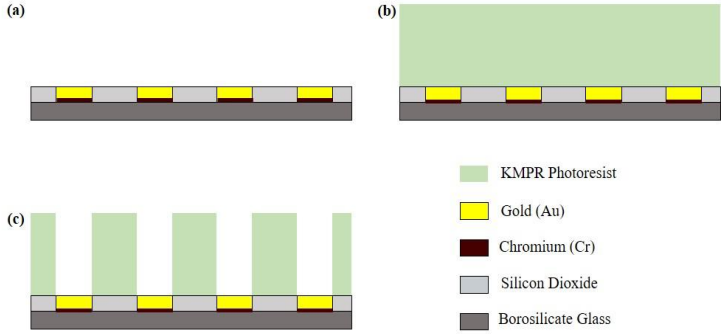

Figure V - 3. (a) Schematic representation planar MEA cross-section. (b) Coating 110 µm thick KMPR photoresist coated on the planar MEA. (c) Photoresist template for electrodeposition of gold micro-pillars over the planar electrodes.

VI.3.1.2 Template development

A photoresist mold was fabricated to support the electrodeposition of gold micro-pillars by coating the planar MEAs with a 110 µm thick layer of chemically amplified negative photoresist (KMPR-1035, Kayaku Advanced Materials, Inc.), followed by a 30-minute soft-bake at 100 °C (refer to Figure 3b). The photoresist was then exposed to UV light using Mask 3 with the mask aligner. A post-exposure bake was then performed at 100 °C for 6 min to ensure complete curing of the exposed area. Finally, the photoresist was developed using an SU-8 developer solution (MicroChemicals GmbH) for 20 min, using a shaker plate and mild agitation. This step created a photoresist template featuring 110 µm deep cylindrical wells aligned over planar electrodes (refer to Figure VI-3c).

VI.3.1.3 Selective electrodeposition of 3D electrodes

The electrodeposition process began with applying Kapton tape to the etch windows in the template. This was followed by a brief oxygen plasma treatment to eliminate any potential lithographic process residue that could interfere with the material deposition. In the initial stage of the process, all electrodes, except for G1, were connected to the external metal ring through external routing (refer to Figure VI-4a). Gold electrodeposition was performed using a current density of 4 mA/cm^2 under continuous ultrasonic vibrations and a temperature of 55 °C. The first stage of

electrodeposition was terminated upon realizing the desired height for the G2 electrodes (refer to Figure VI-4b).

The next step involves disconnecting the G2 electrodes from the outer metal ring. This was achieved by etching the external circuitry through the internal etch windows present in the photoresist template. The second stage electrodeposition process was initiated and continued for the G3 and G4 electrodes until the desired height for the G3 electrodes was realized (refer to Figure VI-4c). The G3 electrodes were then disconnected from the working electrode by etching the external circuitry through the external etch windows in the photoresist template. Finally, the G4 electrodes underwent third-stage electrodeposition until the desired height for G4 electrodes was realized (refer to Figure VI-4d). After the multi-stage electrodeposition process was completed, the KMPR mold was stripped using an mr-Rem 700 solution (MicroResist Technology) under mild agitation.

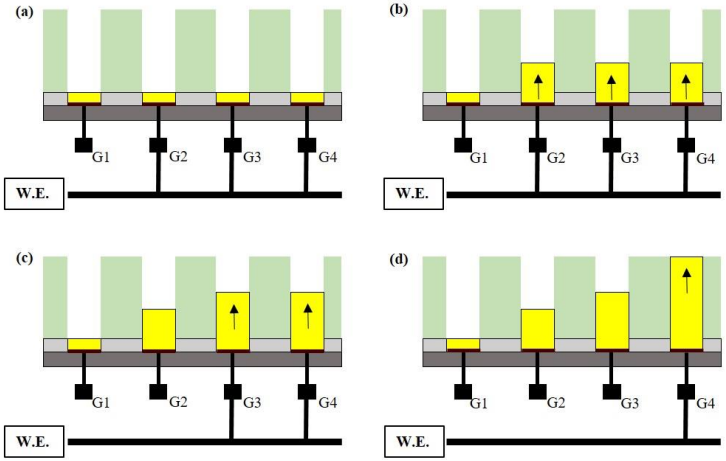

Figure V - 4. The mechanism for selective electrodeposition of gold micro-pillars. (a) Schematic representation of electrodes clubbed into different groups connected to the working electrode (W.E.). (b) First stage electrodeposition, G2, G3, and G4 electrodes are electrodeposited simultaneously (indicated by arrows), and the process is terminated upon realizing the desired height for G2 electrodes. (c) Second stage electrodeposition for G3 and G4 electrodes. (d) Final stage electrodeposition for G4 electrodes.

VI.3.1.4 Sidewall passivation of 3D gold electrodes

A Parylene-C layer of 900 nm thickness was deposited on the 3D MEA using chemical vapor deposition. This layer was necessary for recording electrophysiological activities solely from the top of the micro-pillars in the neuronal culture (refer to Figure VI-5a). To remove the parylene-C layer from the top of the electrodes, a 20 nm thick masking layer of chrome was applied over the parylene-C layer (refer to Figure VI-5b). The chrome layer served as a mask to selectively eliminate the parylene-C layer,

which was defined using a focused ion beam (FIB) assisted milling process with 35 keV gold ions (Au+) at a fluence of 1 mC/cm^2 (refer to Figure VI-5c). The chrome layer on the top of the micro-pillars was removed by milling with 35 keV gold ions. An oxygen-based reactive ion etching process was used to etch the unmasked parylene layer (refer to Figure VI-5d). Finally, the chrome mask layer was removed via wet chemical etching, resulting in sidewall-passivated 3D microelectrodes (refer to Figure 5e).

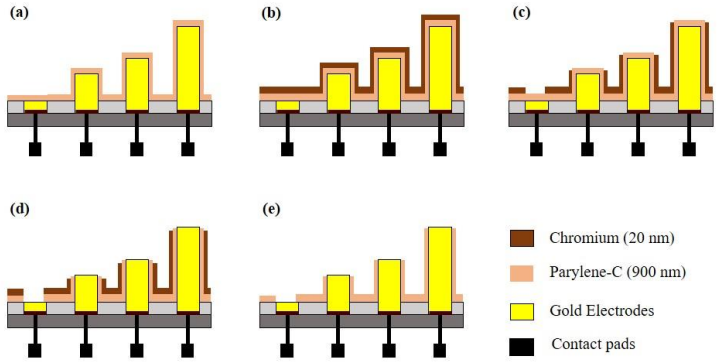

Figure V - 5. Schematic representation of the passivation process. a) The 3D MEA coated with a 900 nm thick Parylene-C layer. (b) 20 nm thick chrome layer deposited over the Parylene-C. (c) Removal of chrome layer from the top surface of the planar and 3D microelectrodes using a custom FIB milling, exposing the Parylene-C layer. (d) The unmasked Parylene-C removed using oxygen based RIE process to expose the electrode surface. (e) Removal of chrome layer using wet chemical etching.

VI.3.1.5 Sidewall passivation of 3D gold electrodes

After sidewall passivation, the 3D MEA devices measuring 10 × 10 mm^2 were sliced along the predefined scribe lines and subsequently mounted onto a custom-designed printed circuit board (PCB) compatible with the MEA2100 readout system using a small quantity of epoxy glue. Gold wire bonding connected the MEA contact pads to the PCB routing. To prevent short-circuiting, the bonding region was covered with an epoxy resin. A poly(dimethylsiloxane) (PDMS) ring with internal and external diameters of 4 and 8 mm, respectively, and a height of 5 mm was placed on the MEA device. This ring served as a well for cell culture. Furthermore, a glass ring with internal and external diameters of 20 and 22 mm, respectively, and a height of 11 mm was mounted on the PCB surrounding the MEA device. Finally, the space between the internal PDMS ring and the glass ring was filled by pouring PDMS and curing it at room temperature (refer to Figure VI-6).

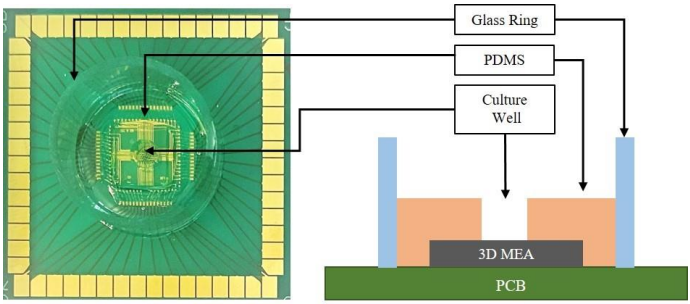

Figure V - 6. 3D MEA packaging scheme. Image of a fully assembled device (left), schematic representation of the cross-sectional view of the packaged device (right).

VI.3.2 Methods for device performance evaluation

VI.3.2.1 Electrode impedance and noise characterization

The impedance of the individual electrodes was assessed using a two-electrode configuration impedance analyzer, specifically the HP4192—LF impedance analyzer. The measurements were carried out within the 1-100 kHz frequency range, using a platinum counter electrode immersed in an electrolytic solution (Cryson) with a pH of 7.

Noise measurements were conducted by recording the electrical activity of the bare electrodes in a PBS buffer solution and medium culture (neurobasal medium) at a frequency of 10 kHz for 2 min using the ME2100-System (MEA 2100-System, MCS) for both MH-MEA and 3D MC MEAs. The noise was evaluated by measuring the amplitude of the raw signals for each MEA electrode. Data are presented as mean ± standard deviation.

VI.3.2.2 Neuronal differentiation and neurospheroids generation

The neuronal differentiation was carried out as described in Frega et al.[184]; briefly, h-iPSCs single-cell solution was plated onto matrigel pre-coated wells and cultured in E8F+dox medium (4 µg/m doxycycline (Day 0)). On Day 1, E8F+dox medium was replaced entirely by DMEM/F12 supplemented with 1% MEM non-essential amino acid solution, 1% N2-supplement, 1% pens/strep, 10 ng/ml human-NT-3 and 10 ng/ml human-BDNF. On Day 3, the cells (Early-stage neurons) were collected and re-suspended in the medium, ready to be counted and used in co-culture for the neurospheroids generation. Astrocytes were obtained from primary cortical embryos (E18) as described in Aprile et al.[185] Neurospheroids comprised 8 x10^4 early-stage neurons and astrocytes in a 1:1 ratio. Neurospheroids were generated by hanging drop method using a 5 cm petri dish as a 'moisture chamber'. The petri dish was half-filled with Dulbecco's phosphate-buffered saline (DPBS), and the inner part of the lid was used as sustain for the drops of the medium used as scaffold-free culture. Specifically, the lid was inverted, and a 15 µl drop of the neurobasal medium was

poured into the inner part of the lid; then, 10 µl of the mixed-cells solution was added into each medium drop previously placed. Finally, the lid was gently placed back on the petri dish to avoid the sliding of the drops and then stored in the incubator at 37 °C and 5.5 CO_2. This day was considered the DIV 0 of the neurospheroids. At DIV 10, the neurospheroids were moved into 24-well plates. The medium was supplemented with 2.5% of FBS and refreshed thrice weekly. At DIV 21, neurospheroids were transferred onto the 3D MEAs.

VI.3.2.3 Preparation of MEAs for cell loading

3D MC MEA (60-3DMEA250/12/100iR-Ti-gr) supplied by MCS was used as control. The 3D MC MEAs are glass devices with 60 titanium nitride electrodes embedded in the center of the culture well. They are arranged in an 8×8 grid without electrodes at the corner, spaced 250 µm among them, and are pyramidal with 100 µm height and 12 µm diameter tip. The 3D MH-MEA has a hexagonal spatial organization of the electrodes, with a cylindrical shape and circular tip having a diameter of 65 µm. Before plating neurospheroids, both 3D MEAs were cleaned and sterilized; 3D MC MEA were sterilized in an oven at 120 °C for two hours while 3D MH-MEA was filled with 70% Ethanol for 40 min. After that, the chambers were washed three times with $_{dd}H_2O$. Each chamber was filled with 2 ml DPBS, and the devices were stored in the incubator for two nights to improve the hydrophilicity of the substrate (conditioning phase). After this phase, all the devices were coated with a bi-layer composed of poly-L-ornithine (PLO, Sigma-Aldrich) and human-laminin (BioConnect). More specifically, 100 µl of PLO solution (100 µg/ml) was placed on the active area of MEAs and then incubated at 4 °C overnight. The day after, the PLO solution was removed from the active area, washed twice with $_{dd}H_2O$, and then replaced with 80 µl of laminin solution (20 µg/ml). Devices were then left overnight at 4 °C. The laminin solution was removed before plating the neurospheroids.

VI.3.2.4 Recording spontaneous electrophysiological activity

The spontaneous electrophysiological activity (15 min) was recorded at DIV 29 using the ME2100-System (MEA 2100-System, MCS). The data were sampled at 10 kHz. Incubator-like conditions were maintained during recording by keeping the culture at 37 °C and 5.5% CO^2 in sterile conditions.

VI.3.2.5 Data analysis

Data analysis was performed using a custom software package named SPYCODE, developed in MATLAB (MathWorks, Natick, MA, USA) [186–188]. Spike detection was performed using a precise timing spike detection algorithm [187]. The algorithm requires three parameters: a different threshold set to eight times the standard deviation of the baseline noise, peak lifetime period (set at 2 ms), and refractory period (set at 1 ms). The raster plots show an overview of the global activity recorded for each MEA electrode. The following main parameters were extracted to

characterize the electrophysiological activity: the mean firing rate (MFR), that is, the number of spikes per second of each channel, and the percentage of random spikes, that is, the fraction of spikes outside bursts. Burst detection was performed according to a previously described method [188]. A burst is a sequence of spikes with an inter-spike interval (i.e., time intervals between consecutive spikes) smaller than a reference value (set at 100 ms in our experiments) and containing at least a minimum number of consecutive spikes (set at five spikes). The parameters extracted from this analysis were the mean bursting rate (MBR) and the mean burst duration (MBD), which are the frequency and duration of the bursts at the single channel level, respectively.

VI.3.2.6 Morphological characterization

After the electrophysiological recordings, samples were fixed directly on the MEA at DIV 30 for immunofluorescence characterization. Samples were fixed using 4% paraformaldehyde solution (PFA, Sigma-Aldrich) for 20 min at room temperature and then washed thrice with Phosphate-buffered saline (PBS, Sigma-Aldrich) solution. Samples were permeabilized with 0.2% triton X-100 (Thermo Fisher Scientific) for 15 min. To block non-specific binding antibodies, samples were exposed to Blocking Buffer Solution (BBS, composed of 0.5% fetal bovine serum (Sigma-Aldrich), 0.3% bovine serum albumin (Sigma-Aldrich) in PBS) for 45 min at room temperature. GFAP (diluted 1:500, Sigma Aldrich) and MAP-2 (diluted 1:500, Chemicon Millipore) were used as primary antibodies to mark glial and neuronal cells, respectively, and Dapi (diluted 1:10000, Sigma) to label nuclei. Alexa Fluor 488 (diluted 1:700, Thermo Fisher Scientific) and Alexa Fluor 546 (diluted 1:1000, Invitrogen) Goat anti-mouse or Goat anti-rabbit were used as secondary antibodies.

VI.3.2.7 Statistical analysis

To analyze the data, a non-parametrical Wilcoxon signed-rank test was performed after evaluating the normality test with GraphPad Prism. Differences were considered significant when $p < 0.05$.

VI.4 Results and discussions

VI.4.1 Development of multi-height (MH) 3D MEAs

The research successfully yielded a new strategy for developing multi-height 3D MEA devices with 60 channels. During this experiment, an 8-device batch of MEA was fabricated on 150 mm glass wafers, using a single working electrode to facilitate the selective electrodeposition of gold micro-pillars. Each MEA device contained 60 electrodes with a 65 µm diameter and a 265 µm pitch, grouped into four categories (G1, G2, G3, and G4) according to the electrodes' height.

The G1 group represented the first level electrodes, showcasing a planar topology relative to the MEA's surface. Meanwhile, the G2, G3, and G4 groups denoted the second, third, and fourth level electrodes, respectively, each with varying

heights: G2 at 35 ± 2 µm, G3 at 65 ± 2 µm, and G4 at 120 ± 2 µm, throughout the batch of 8 devices. Throughout and following the fabrication process, the electrodes' height underwent monitoring and measurement via an optical profilometer. Figure VI-7a shows an optical scan of the final multi-height 3D MEA acquired using an optical profilometer. The height profiles for electrodes from different groups were acquired from a cross-section of the optical scan image (refer to Figure VI-7b). The MEA layout and the distribution of the multi-level electrodes across the array (refer to Figure VI-7c). Figure VI-7d presents a close-up view of a section of the 3D MEA highlighting different height electrodes, marked with their respective group names.

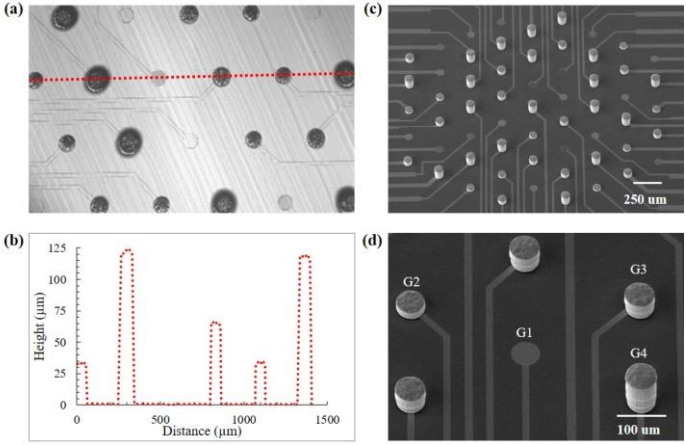

Figure V - 7. Multi-height 3D MEA. (a) Optical scan of the multi-level electrodes obtained using an optical profilometer. (b) Height profile of the multi-level electrodes extracted along the dashed line in Figure 7a. (c) SEM image of 3D MEA showing the uniform distribution of the multi-level electrodes across the array, (d) close-up SEM image of the array showing the different electrode heights and distribution.

VI.4.2 Device characterization

VI.4.2.1 Electrochemical impedance measurements

We measured the impedance of electrodes across all four groups and compared the results to assess electrode behavior over a 1– 100 kHz frequency range. As anticipated, every electrode demonstrated capacitive behavior, with the impedance modulus decreasing linearly as a function of frequency on a log-log scale (refer to Figure VI-8a). Meanwhile, the impedance phase maintained at around -80 degrees up to roughly 10 kHz, then decreased (refer to Figure VI-8b).

For a more detailed evaluation of the disparities among different groups, we took impedance measurements of the electrodes at 10 kHz (refer to Figure VI-8c). We

then used these impedance and phase values to compute the electrodes' double-layer capacitance (refer to Figure VI-8d).

The impedance measurements revealed that the active surface area of the G1 electrodes was significantly smaller than those from other groups due to the planar topology of the G1 electrodes.

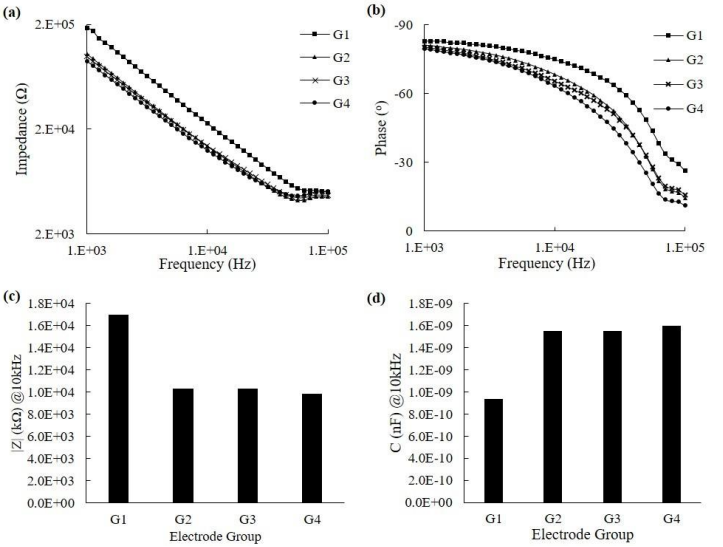

Figure V - 8. Electrochemical impedance measurements. (a) The magnitude of the impedance |Z| and b) the phase. c) The planar electrodes (G1) have a significantly higher magnitude of impedance |Z| measured at a frequency of 10 kHz and (d) lower double-layer capacitance compared to electrodeposited electrodes due to the planar topology.

Each electrode demonstrated capacitive behavior, with the impedance modulus decreasing linearly as a function of frequency on a log-log scale (refer to Figure VI-8a). Meanwhile, the impedance phase maintained at around -80 degrees up to roughly 10 kHz, then decreased (refer to Figure VI-8b). At 10 kHz, the planar electrodes (G1) had the highest impedance magnitude of 17 ± 1.64 kΩ, while the electrodeposited electrodes (G2, G3, and G4) had a much lower impedance magnitude ranging between 9.5 – 10.5 kΩ averaged over 10 number of electrodes from each group.

VI.4.2.2 Noise measurements

MEA noise measurements were performed by recording electrical activity from various devices using the MCS System. The experimental protocol involved a 2-minute recording at 10 kHz in both a PBS buffer solution and a medium culture solution (refer to Figure VI-9). We compared the noise of the 3D MH-MEA to that recorded from the commercial 3D MC MEA.

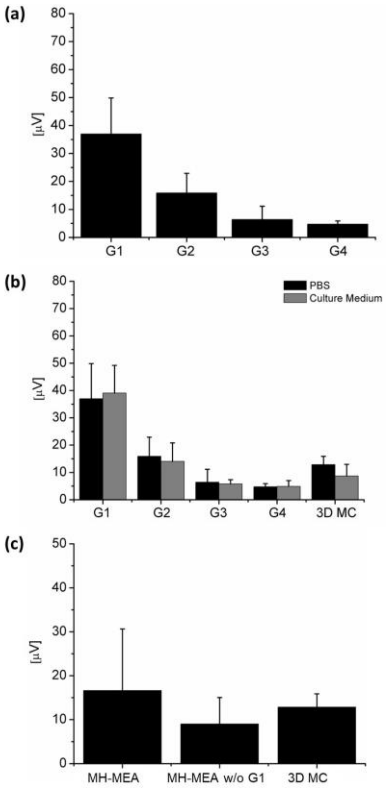

Figure V - 9. Noise characterization. Noise measurements for MH MEA were performed by recording the electrical activity of the electrodes in a PBS buffer solution at 10 kHz for 2 min and compared with the state-of-the-art commercial 3D MC MEA. (a) Comparison of mean noise of different electrode groups with all the active channels. (b) Comparison of mean noise of MH-MEA electrode groups and 3D MC with all the active channels in PBS and medium culture. (c) Comparison of mean noise of MH-MEA with and w/o G1 electrodes and 3D MC.

The amplitude of the raw signals for each electrode was recorded to evaluate the noise. Initially, the average noise for each electrode group, G1, G2, G3, and G4, was analyzed (refer to Figure VI-9a). The signals recorded by G1 electrodes exhibited the highest noise levels among all groups, and we observed a significant reduction in noise for the 3D electrodes.

Furthermore, the noise was measured in two buffer solutions, PBS and medium culture (refer to Figure VI-9b). There were no statistical differences when comparing these two different conditions. The measurements performed with the 3D MC MEA provided similar results.

Lastly, when comparing the mean noise of all electrode groups of the MH-MEA (G1, G2, G3, and G4) and the 3D MC MEA, with all 60 channels active, the noise values of the multi-level MEAs were significantly higher compared to the commercial ones. However, excluding the G1 electrodes of the 3D MH-MEA resulted in a substantial overall reduction in noise, rendering it more suitable for recording electrophysiological activities (refer to Figure VI-9c).

VI.4.3 MH-MEA performance evaluation

The neurospheroids were plated on both types of 3D MEAs at 21 Days *In Vitro* (DIV) after the complete formation of a three-dimensional structure when neuronal and glial cells created a dense network with a spherical shape (refer to Figure VI-10). Neurospheroids showed a mean diameter of around 500 µm. The recording was performed one week after the plating to allow adhesion onto the 3D MEA's surface and ensure good interaction between cells and electrodes. Over time, neuronal processes enveloped the 3D electrodes while maintaining functional connections. The spontaneous activity (raw signal) of 1s of a neurospheroid recorded from one microelectrode of 3D MC and MH-MEA is shown in Figure VI-10c and Figure VI-10d, respectively.

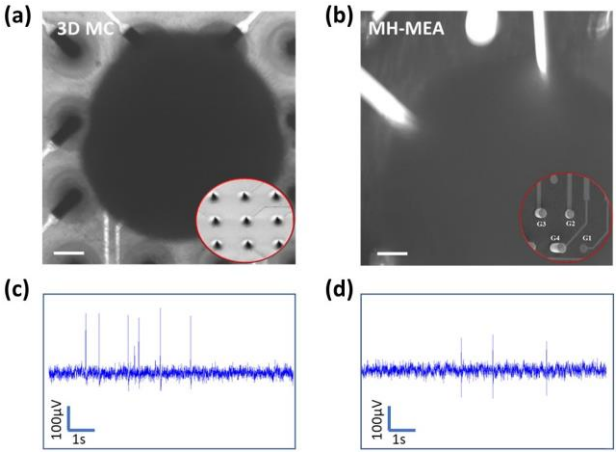

Figure VI - 10. Optical images showing neurospheroid at DIV 25 on, (a) 3D MC MEA with electrode profiles under the neurospheroid insert in red circle (scale: 50 µm) and (b) MH-MEA with electrode profiles under the neurospheroid insert in red circle (scale: 50 µm). Raw data trace recorded by one electrode placed below the neurospheroid plated on (c) 3D MC MEA, (d) MH-MEA.

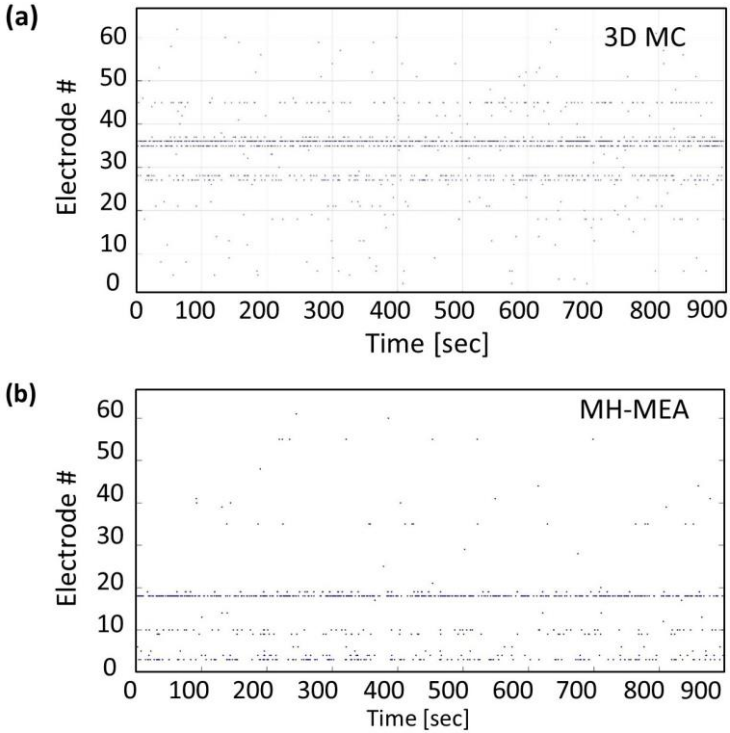

Figure VI - 11. Spontaneous activity recordings,raster plots showing 15 min of activity recorded by (a) 3D MC MEA, and (b) MH-MEA.

A suitable resolution of the MH-MEA permits to clearly identify the onset of network events similar to what was observed with 3D MC MEA. The global electrophysiological behavior of a representative 3D network is shown in the raster plots, where 15 min of spontaneous activities are displayed (refer to Figure VI-11). In both MEA configurations, the activity recorded was related to a specific small group of electrodes (~5-8). This was due to the dimension of the neurospheroid (500 μm) that involved a low number of electrodes. The parameters extracted from the spontaneous activity recordings were analyzed for spike data (refer to Figure VI-12). Neurospheroids of 3D MC MEA presented values of MFR (0.80 ± 0.06 spikes/s), different from the MH-MEA (0.47± 0.04 spikes/s; $p < 0.05$) (refer to Figure VI-12a). In both 3D MEA configurations, some electrodes were active even far away from the neurospheroids during the recording. For this reason, after the recordings, the 3D cultures were observed under the microscope, and we noticed that some cells moved out from the neurospheroids to other electrodes from which firing activity was detected. Both 3D experimental configurations detected high and comparable spiking activity values (refer to Figure VI-12a). Regarding the bursting behavior, the two MEA

configurations shared similar values of MBR (refer to Figure 12b) and MBD (refer to Figure VI-12c); in particular, 3D MC MEA showed an MBR of 2.4 ± 0.57 (bursts/min) and values of MBD around 234.60 ± 67.39 (ms); while the values of MBR and MBD obtained by the MH-MEA recordings were around 1.99 ± 0.22 (bursts/min) and 214.83 ± 13.19 (ms) respectively.

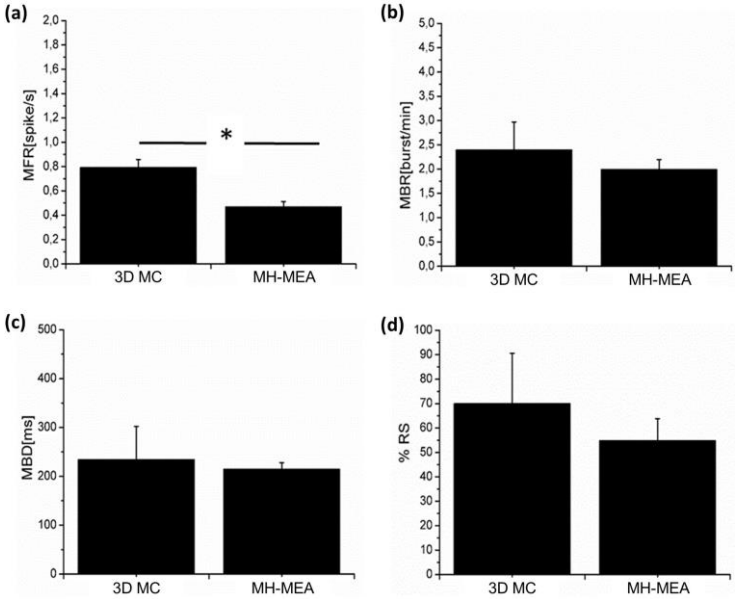

Figure VI - 12. Spike data analysis of recorded spontaneous activity. (a) Mean firing rate, (b) Mean bursting rate (MBR), (c) Mean burst duration (MBD), and (d) Percentual random spikes (%RS) (n = 5, where n is number of electrodes actively recording the electrophysiological signals for each MEA).

This characterization indicated that MH-MEA could record spontaneous electrophysiological activity from mature human-derived neurospheroids, like the commercial 3D MC MEA. An indirect immunofluorescence technique was used to characterize neurospheroids onto the MH-MEA (refer to Figure VI-13). To this purpose, the samples were prepared for indirect immunostaining at the end of the recording session. Morphological characterization confirmed and supported the results obtained by electrophysiological measures. In particular, 3D neurospheroids composed of human iPSC-derived cortical neurons and astrocytes have mostly retained their spherical shape, creating a packed network of neuronal and glial processes correctly plated onto the active area of 3D MEA. In fact, the position of the neurospheroids corresponded to the active electrodes from which the spontaneous activity was recorded (refer to Figure VI-13a).

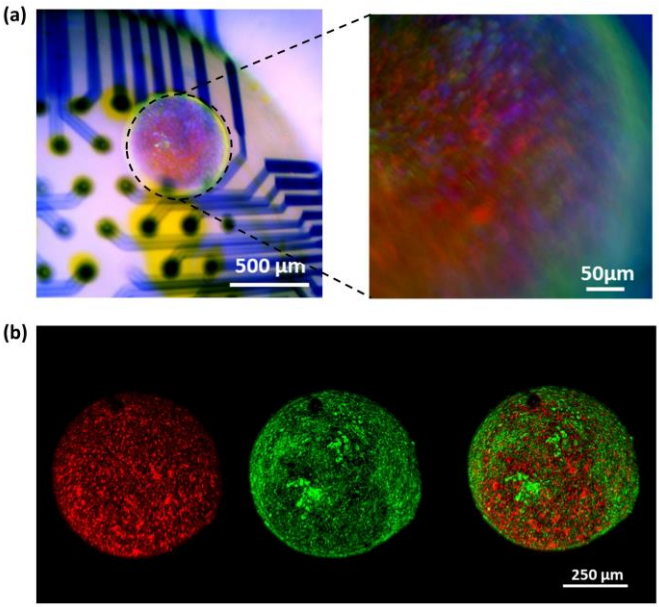

Figure VI - 13. Morphology of the neurospheroid plated on MH-MEA. (a) Fluorescence images of neurospheroid on MH-MEA and zoom of the same neurospheroid at DIV 30 marked for MAP-2 (green), GFAP (red), and DAPI (blue). Scale bar: 250 µm, 100 µm. (b) Confocal images; max projection of neurospheroid at DIV 30 labeled for GFAP (red), MAP-2 (green), and merge).

The presence of neurons and astrocytes was confirmed by positive staining with Microtubule-Associated Protein 2 (MAP-2), a protein highly expressed in neurons, and Glial Fibrillary Acidic Protein (GFAP), a protein expressed by astrocytes. Confocal microscopy characterization allowed us to gain information on the morphology of the 3D structure of mature neuronal distribution of neural cells on the surface and interior of the neurospheroids (refer to Figure VI-13b). Specifically, the max projection obtained by a 3D reconstruction of 240 µm z-stack of the human neurospheroids immunolabeled for the dendritic marker MAP-2 and GFAP gave us a comprehensive view of the 3D neural structure, indicating that the MH-MEA supported healthy neurospheroids cultures that were not affected by any materials present in the 3D MEA arrays.

VI.5 Chapter highlights

- Technological Platform Optimization: We introduced an optimized external circuitry layout tailored to support the three stages of selective

electrodeposition using 3D MEAs consisting of electrodes with four distinct height levels.

- Batch Fabrication: The fabrication process yielded a batch of eight 60-channel MH-MEA devices, with electrodes organized into four groups based on their heights. This organization enables the precise probing of neuronal activity across multiple spatial dimensions.
- Electrode Performance: Evaluation of the electrodes revealed low electrochemical impedance and noise measurement properties across all four groups, indicating the reliability and quality of the fabricated MH-MEAs.
- Insights from Measurement: Detailed measurements provided valuable insights into the behavior of the electrodes across a range of frequencies, elucidating their performance characteristics and potential applications in advanced electrophysiological studies.
- Efficacy in Electrophysiological Activity Monitoring: The multi-depth probing MH-MEA demonstrated efficacy in monitoring the electrophysiological activity of a 3D neuronal culture. This capability opens new avenues for studying complex neuronal activity in a three-dimensional setup.
- MH-MEA Performance Evaluation: Recording spontaneous electrophysiological activity from mature human-derived neurospheroids using the MH-MEA yielded results comparable to those obtained from a commercial 3D MC MEA, indicating the reliability and effectiveness of the developed platform.

Chapter VII: Final comments and scope for further development

VII.1 Accomplishments of the project

A novel technological platform for developing variable-height 3D MEAs was designed and developed. The platform utilizes photolithography and template-assisted electrodeposition to produce a batch of 3D MEAs. The initial platform design included a custom circuitry external to the MEA layout to support two-stage selective electrodeposition, yielding 3D MEAs with three distinct electrode heights [91]. The custom circuitry was completed and manipulated using gold wire bonding to allow for selectivity during electrodeposition. The process successfully produced 3D electrodes with the desired mean heights; however, the heights of the 3D electrodes had a percentage standard deviation of 12%, indicating a very high nonuniformity in the electrode heights across an individual MEA and a batch of four MEAs. This constitutes the results and discussion presented in Chapter IV.

An ultrasonic-enhanced template-assisted electrodeposition process was developed to achieve precise control over the height of the 3D electrodes and improve the uniformity of the heights of the electrodeposited 3D electrodes. This project investigated the effects of ultrasonic vibrations on the template-assisted electrodeposition of gold micropillars for constructing 3D MEAs. The research demonstrated that continuous ultrasonic bath-assisted electrodeposition led to a significant increase in the deposition rate, five times more than deposition without any agitation and more than double compared to agitated electrodeposition using a magnetic stirring bead. A significant improvement in the uniformity of the electrode heights was achieved using continuous ultrasonic vibrations throughout the template-assisted electrodeposition process, leading to a standard deviation of less than 2% [189]. These constitute the results and discussions presented in Chapter V.

The platform design was further optimized by reengineering the custom circuitry layout and manipulation mechanism to allow for three stages of the selective electrodeposition process. The circuit layout was engineered to allow reductive circuit manipulation using wet chemical etching instead of a time- and labor-intensive wire bonding approach. Using the optimized circuit layout and an ultrasonic-enhanced template-assisted electrodeposition process, variable-height 3D MEAs (MH-MEAs) were fabricated. The MH-MEAs consisted of electrodes with four distinct height levels, ranging between 0 and 120 μm, with a standard deviation of 2 μm. Rigorous testing and characterization of the 3D electrodes demonstrated low electrochemical impedance and noise across all electrode groups. This thorough analysis provided valuable insights into the electrode behavior across different frequencies, highlighting the potential of the fabricated MEAs for advanced electrophysiological studies. Electrophysiological activity recordings conducted using MH-MEAs showed efficacy in monitoring the electrophysiological activity of 3D neuronal cultures. To evaluate the

performance of the MH-MEA, a commercial 3D MEA (3D MC) consisting of uniform height 3D electrodes was used as a control since no commercial variable height 3D MEA was available. The ability to record spontaneous electrophysiological activity from mature human-derived neurospheroids is comparable to that of commercial 3D MEAs, validating the device's ability to perform electrophysiological investigations [190]. It is essential to highlight that the commercial 3D MEA recorded the activity from a single plane in the z-dimension within the neurospheroid. In contrast, the MH-MEA, consisting of electrodes with four distinct heights, recorded the electrophysiological activity from 4 different planes in the z-dimension, including the surface layer of the neurospheroid. These constitute the results and discussions presented in Chapter VI.

VII.2 Limitations of the proposed methodologies

The proposed technological platform offers advantages over other platforms, such as batch production of variable-height 3D MEAs and high precision and uniformity in the heights of the electrodeposited 3D electrodes. However, the proposed methodology has two critical limitations that must be addressed. The first and significant limitation pertains to the aspect ratio of the electrodeposited 3D electrodes. Thus far, 3D electrodes with aspect ratios of up to 1:4 (width to height) have been successfully developed using a template-assisted electrodeposition approach [40,189]. Further process optimizations could potentially improve the aspect ratios of the electrode to a certain limit, which still needs to be investigated thoroughly. Although the electrodeposited 3D electrodes cannot attain the high aspect ratios offered by state-of-the-art 3D-printed 3D MEAs [39], they successfully address the limitations of 3D electrodes concerning electrode conductivity and post-processing issues [49].

The second major limitation of the proposed methodology is electrode density. The platform uses an ultrasonic-enhanced template-assisted electrodeposition process to fabricate 3D electrodes, where the template bears long exposure to ultrasonication vibrations, leading to slow substrate-template adhesion failure. The smaller pitches required for high-density arrays could accelerate the substrate-template adhesion failure.

VII.3 Further development

To advance the capabilities of three-dimensional (3D) Microelectrode Arrays (MEAs), future developments may focus on several key areas to enhance their functionality and versatility further. First, researchers could aim to enhance the precision and control of the electrodeposition process by refining the circuitry design and integration to support additional stages of selective electrodeposition. This would enable the creation of more intricate and customizable 3D electrode structures, ultimately leading to improved spatial resolution and deeper penetration into the 3D neuronal constructs. Such advancements could significantly expand the application

range of 3D MEAs for studying complex neural networks and probing deeper layers of tissue.

Second, efforts should be directed toward developing electrodes with higher aspect ratios and electrode density for enhanced spatial resolution. By optimizing fabrication techniques and materials, researchers can strive to create electrodes with taller and narrower profiles, thus enhancing their ability to record neural activity from deeper tissue layers. This development could lead to a more comprehensive understanding of the neural circuitry and facilitate the development of targeted therapies for neurological disorders.

Furthermore, integrating 3D MEAs with complementary metal–oxide semiconductor (CMOS)-based chips and integrated electronics represents another promising avenue for future development. By directly integrating electrode arrays with CMOS circuitry, researchers can streamline data acquisition, processing, and analysis while reducing the device footprint and power consumption. This integration could pave the way for more compact and efficient neural recording systems suitable for various research and clinical applications [40].

References

1. Singer, H.S.; Chiu, A.Y.; Meiri, K.F.; Morell, P.; Nelson, P.G.; Tennekoon, G. Advances in Understanding the Development of the Nervous System. *Curr. Opin. Neurol.* **1994**, *7*, 153–159.
2. Oosting, P.H. Signal Transmission in the Nervous System. *Reports Prog. Phys.* **1979**, *42*, 1479–1532, doi:10.1088/0034-4885/42/9/001.
3. Flavell, S.W.; Greenberg, M.E. Signaling Mechanisms Linking Neuronal Activity to Gene Expression and Plasticity of the Nervous System. *Annu. Rev. Neurosci.* **2008**, *31*, 563–590, doi:10.1146/annurev.neuro.31.060407.125631.
4. Massobrio, P.; Tessadori, J.; Chiappalone, M.; Ghirardi, M. In Vitro Studies of Neuronal Networks and Synaptic Plasticity in Invertebrates and in Mammals Using Multielectrode Arrays. *Neural Plast.* **2015**, *2015*, 196195, doi:10.1155/2015/196195.
5. Petersen, O.; Petersen, C. The Patch-Clamp Technique: Recording Ionic Currents Through Single Pores in the Cell Membrane. *Physiology* **1986**, *1*, 5–8, doi:10.1152/physiologyonline.1986.1.1.5.
6. Obien, M.E.J.; Deligkaris, K.; Bullmann, T.; Bakkum, D.J.; Frey, U. Revealing Neuronal Function through Microelectrode Array Recordings. *Front. Neurosci.* **2015**, *8*, 423, doi:10.3389/fnins.2014.00423.
7. Kungl, A. Robust Learning Algorithms for Spiking and Rate-Based Neural Networks, 2020.
8. Centeno, E.G.Z.; Cimarosti, H.; Bithell, A. 2D versus 3D Human Induced Pluripotent Stem Cell-Derived Cultures for Neurodegenerative Disease Modelling. *Mol. Neurodegener.* **2018**, *13*, 27, doi:10.1186/s13024-018-0258-4.
9. Lancaster, M.A.; Knoblich, J.A. Organogenesis in a Dish: Modeling Development and Disease Using Organoid Technologies. *Science* **2014**, *345*, 1247125, doi:10.1126/science.1247125.
10. Pașca, S.P. The Rise of Three-Dimensional Human Brain Cultures. *Nature* **2018**, *553*, 437–445, doi:10.1038/nature25032.
11. Rabile, S. MEA Multelectrode Arrays | NMI TT Microdevices Available online: https://www.nmi-tt.de/microdevices/meas/ (accessed on 20 February 2024).
12. Cabrera-Garcia, D.; Warm, D.; de la Fuente, P.; Fernández-Sánchez, M.T.; Novelli, A.; Villanueva-Balsera, J.M. Early Prediction of Developing Spontaneous Activity in Cultured Neuronal Networks. *Sci. Rep.* **2021**, *11*, 20407, doi:10.1038/s41598-021-99538-9.
13. Frega, M.; Tedesco, M.; Massobrio, P.; Pesce, M.; Martinoia, S. Network Dynamics of 3D Engineered Neuronal Cultures: A New Experimental Model for in-Vitro Electrophysiology. *Sci. Rep.* **2014**, *4*, doi:10.1038/SREP05489.
14. Pine, J. A History of MEA Development. In *Advances in Network Electrophysiology*; Taketani, M., Baudry, M., Eds.; Springer US: Boston, MA, 2006; pp. 3–23.
15. Brofiga, M.; Pisano, M.; Raiteri, R.; Massobrio, P. On the Road to the Brain-on-a-Chip: A Review on Strategies, Methods, and Applications. *J. Neural*

Eng. **2021**, *18*, 041005, doi:10.1088/1741-2552/AC15E4.
16. Kacy Cullen, D.; Wolf, J.A.; Vernekar, V.N.; Vukasinovic, J.; la Placa, M.C. Neural Tissue Engineering and Biohybridized Microsystems for Neurobiological Investigation in Vitro (Part 1). *Crit. Rev. Biomed. Eng.* **2011**, *39*, 201–240, doi:10.1615/CRITREVBIOMEDENG.V39.I3.30.
17. Pautot, S.; Wyart, C.; Isacoff, E.Y. Colloid-Guided Assembly of Oriented 3D Neuronal Networks. *Nat. Methods* **2008**, *5*, 735, doi:10.1038/NMETH.1236.
18. Tedesco, M.; Frega, M.; Martinoia, S.; Pesce, M.; Massobrio, P. Interfacing 3D Engineered Neuronal Cultures to Micro-Electrode Arrays: An Innovative In Vitro Experimental Model. *J. Vis. Exp.* **2015**, *2015*, 53080, doi:10.3791/53080.
19. Yue, B. Biology of the Extracellular Matrix: An Overview. *J. Glaucoma* **2014**, *23*, S20-3, doi:10.1097/IJG.0000000000000108.
20. Chwalek, K.; Tang-Schomer, M.D.; Omenetto, F.G.; Kaplan, D.L. In Vitro Bioengineered Model of Cortical Brain Tissue. *Nat. Protoc.* **2015**, *10*, 1362–1373, doi:10.1038/nprot.2015.091.
21. Bosi, S.; Rauti, R.; Laishram, J.; Turco, A.; Lonardoni, D.; Nieus, T.; Prato, M.; Scaini, D.; Ballerini, L. From 2D to 3D: Novel Nanostructured Scaffolds to Investigate Signalling in Reconstructed Neuronal Networks. *Sci. Rep.* **2015**, *5*, 9562, doi:10.1038/srep09562.
22. Brofiga, M.; Pisano, M.; Tedesco, M.; Raiteri, R.; Massobrio, P. Three-Dimensionality Shapes the Dynamics of Cortical Interconnected to Hippocampal Networks. *J. Neural Eng.* **2020**, *17*, 056044, doi:10.1088/1741-2552/abc023.
23. Xu, T.; Molnar, P.; Gregory, C.; Das, M.; Boland, T.; Hickman, J.J. Electrophysiological Characterization of Embryonic Hippocampal Neurons Cultured in a 3D Collagen Hydrogel. *Biomaterials* **2009**, *30*, 4377–4383, doi:10.1016/j.biomaterials.2009.04.047.
24. Ulloa Severino, F.P.; Ban, J.; Song, Q.; Tang, M.; Bianconi, G.; Cheng, G.; Torre, V. The Role of Dimensionality in Neuronal Network Dynamics. *Sci. Rep.* **2016**, *6*, 29640, doi:10.1038/srep29640.
25. Soscia, D.A.; Lam, D.; Tooker, A.C.; Enright, H.A.; Triplett, M.; Karande, P.; Peters, S.K.G.; Sales, A.P.; Wheeler, E.K.; Fischer, N.O. A Flexible 3-Dimensional Microelectrode Array for in Vitro Brain Models. *Lab Chip* **2020**, *20*, 901–911, doi:10.1039/c9lc01148j.
26. Shin, H.; Jeong, S.; Lee, J.-H.; Sun, W.; Choi, N.; Cho, I.-J. 3D High-Density Microelectrode Array with Optical Stimulation and Drug Delivery for Investigating Neural Circuit Dynamics. *Nat. Commun.* **2021**, *12*, 492, doi:10.1038/s41467-020-20763-3.
27. Callegari, F.; Brofiga, M.; Massobrio, P. Modeling the Three-Dimensional Connectivity of in Vitro Cortical Ensembles Coupled to Micro-Electrode Arrays. *PLOS Comput. Biol.* **2023**, *19*, doi:10.1371/JOURNAL.PCBI.1010825.
28. Thiébaud, P.; de Rooij, N.F.; Koudelka-Hep, M.; Stoppini, L. Microelectrode Arrays for Electrophysiological Monitoring of Hippocampal Organotypic Slice Cultures. *IEEE Trans. Biomed. Eng.* **1997**, *44*, 1159–1163, doi:10.1109/10.641344.

29. Heuschkel, M.O.; Fejtl, M.; Raggenbass, M.; Bertrand, D.; Renaud, P. A Three-Dimensional Multi-Electrode Array for Multi-Site Stimulation and Recording in Acute Brain Slices. *J. Neurosci. Methods* **2002**, *114*, 135–148, doi:10.1016/S0165-0270(01)00514-3.
30. Nam, Y.; Wheeler, B.C.; Heuschkel, M.O. Neural Recording and Stimulation of Dissociated Hippocampal Cultures Using Microfabricated Three-Dimensional Tip Electrode Array. *J. Neurosci. Methods* **2006**, *155*, 296–299, doi:10.1016/j.jneumeth.2006.01.014.
31. Rajaraman, S.; McClain, M.A.; Choi, S.-O.; Ross, J.D.; DeWeerth, S.P.; LaPlaca, M.C.; Allen, M.G. Three-Dimensional Metal Transfer Micromolded Microelectrode Arrays (MEAS) for In-Vitro Brain Slice Recordings. In Proceedings of the TRANSDUCERS 2007 - 2007 International Solid-State Sensors, Actuators and Microsystems Conference; IEEE, 2007; pp. 1251–1254.
32. Musick, K.; Khatami, D.; Wheeler, B.C. Three-Dimensional Micro-Electrode Array for Recording Dissociated Neuronal Cultures. *Lab Chip* **2009**, *9*, 2036–2042, doi:10.1039/b820596e.
33. Charvet, G.; Rousseau, L.; Billoint, O.; Gharbi, S.; Rostaing, J.-P.; Joucla, S.; Trevisiol, M.; Bourgerette, A.; Chauvet, P.; Moulin, C.; et al. BioMEA: A Versatile High-Density 3D Microelectrode Array System Using Integrated Electronics. *Biosens. Bioelectron.* **2010**, *25*, 1889–1896, doi:10.1016/j.bios.2010.01.001.
34. Dimaki, M.; Vazquez, P.; Olsen, M.H.; Sasso, L.; Rodriguez-Trujillo, R.; Vedarethinam, I.; Svendsen, W.E. Fabrication and Characterization of 3D Micro- and Nanoelectrodes for Neuron Recordings. *Sensors (Basel).* **2010**, *10*, 10339–10355, doi:10.3390/s101110339.
35. Goncalves, S.B.; Peixoto, A.C.; Silva, A.F.; Correia, J.H. Fabrication and Mechanical Characterization of Long and Different Penetrating Length Neural Microelectrode Arrays. *J. Micromechanics Microengineering* **2015**, *25*, 055014, doi:10.1088/0960-1317/25/5/055014.
36. Bartsch, H.; Baca, M.; Fernekorn, U.; Müller, J.; Schober, A.; Witte, H. Functionalized Thick Film Impedance Sensors for Use in In Vitro Cell Culture. *Biosensors* **2018**, *8*, 37, doi:10.3390/bios8020037.
37. Lorenzelli, L.; Spanu, A.; Pedrotti, S.; Tedesco, M.; Martinoia, S. Three-Dimensional Microelectrodes Array Based on Vertically Stacked Beads For Mapping Neurons' Electrophysiological Activity. In Proceedings of the 2019 20th International Conference on Solid-State Sensors, Actuators and Microsystems & Eurosensors XXXIII (TRANSDUCERS & EUROSENSORS XXXIII); IEEE, June 1 2019; pp. 987–990.
38. Spanu, A.; Colistra, N.; Farisello, P.; Friz, A.; Arellano, N.; Rettner, C.T.; Bonfiglio, A.; Bozano, L.; Martinoia, S. A Three-Dimensional Micro-Electrode Array for in-Vitro Neuronal Interfacing. *J. Neural Eng.* **2020**, *17*, 036033, doi:10.1088/1741-2552/ab9844.
39. Saleh, M.S.; Ritchie, S.M.; Nicholas, M.A.; Gordon, H.L.; Hu, C.; Jahan, S.; Yuan, B.; Bezbaruah, R.; Reddy, J.W.; Ahmed, Z.; et al. CMU Array: A 3D Nanoprinted, Fully Customizable High-Density Microelectrode Array Platform. *Sci. Adv.* **2022**, *8*, eabj4853, doi:10.1126/sciadv.abj4853.

40. Mapelli, L.; Dubochet, O.; Tedesco, M.; Sciacca, G.; Ottaviani, A.; Monteverdi, A.; Battaglia, C.; Tritto, S.; Cardot, F.; Surbled, P.; et al. Design, Implementation, and Functional Validation of a New Generation of Microneedle 3D High-Density CMOS Multi-Electrode Array for Brain Tissue and Spheroids. *bioRxiv* **2022**, doi:doi.org/10.1101/2022.08.11.503595.
41. Dong, S.; Dong, L.; Wang, R.; Wang, L.; Song, Z.; Wang, Z. A Simulation Model of Cardiomyocyte - 3D Microelectrode Arrays for Studying Single-Cell Electrical Properties. In Proceedings of the 2022 16th ICME International Conference on Complex Medical Engineering (CME); IEEE, November 4 2022; pp. 7–11.
42. Kundu, A.; McCoy, L.; Azim, N.; Nguyen, H.; Didier, C.M.; Ausaf, T.; Sharma, A.D.; Curley, J.L.; Moore, M.J.; Rajaraman, S. Fabrication and Characterization of 3D Printed, 3D Microelectrode Arrays for Interfacing with a Peripheral Nerve-on-a-Chip. *ACS Biomater. Sci. Eng.* **2021**, *7*, 3018–3029, doi:10.1021/acsbiomaterials.0c01184.
43. Molina-Martínez, B.; Jentsch, L.-V.; Ersoy, F.; van der Moolen, M.; Donato, S.; Ness, T. V; Heutink, P.; Jones, P.D.; Cesare, P. A Multimodal 3D Neuro-Microphysiological System with Neurite-Trapping Microelectrodes. *Biofabrication* **2022**, *14*, 025004, doi:10.1088/1758-5090/ac463b.
44. Spira, M.E.; Hai, A. Multi-Electrode Array Technologies for Neuroscience and Cardiology. *Nat. Nanotechnol.* **2013**, *8*, 83–94, doi:10.1038/nnano.2012.265.
45. Du, J.; Riedel-Kruse, I.H.; Nawroth, J.C.; Roukes, M.L.; Laurent, G.; Masmanidis, S.C. High-Resolution Three-Dimensional Extracellular Recording of Neuronal Activity with Microfabricated Electrode Arrays. *J. Neurophysiol.* **2009**, *101*, 1671–1678, doi:10.1152/jn.90992.2008.
46. Revyn, N.; Hu, M.H.Y.; Frimat, J.-P.M.S.; De Wagenaar, B.; Van den Maagdenberg, A.M.J.M.; Sarro, P.M.; Mastrangeli, M. Recording Neuronal Activity On Chip with Segmented 3D Microelectrode Arrays. In Proceedings of the 2022 IEEE 35th International Conference on Micro Electro Mechanical Systems Conference (MEMS); IEEE, January 9 2022; Vol. 2022-January, pp. 102–105.
47. Morales-Carvajal, P.M.; Kundu, A.; Didier, C.M.; Hart, C.; Sommerhage, F.; Rajaraman, S. Makerspace Microfabrication of a Stainless Steel 3D Microneedle Electrode Array (3D MEA) on a Glass Substrate for Simultaneous Optical and Electrical Probing of Electrogenic Cells. *RSC Adv.* **2020**, *10*, 41577–41587, doi:10.1039/D0RA06070D.
48. Grob, L.; Rinklin, P.; Zips, S.; Mayer, D.; Weidlich, S.; Terkan, K.; Weiß, L.J.K.; Adly, N.; Offenhäusser, A.; Wolfrum, B. Inkjet-Printed and Electroplated 3D Electrodes for Recording Extracellular Signals in Cell Culture. *Sensors (Basel).* **2021**, *21*, 3981, doi:10.3390/s21123981.
49. Veloso, W.B.; Paixão, T.R.L.C.; Meloni, G.N. 3D Printed Electrodes Design and Voltammetric Response. *Electrochim. Acta* **2023**, *449*, 142166, doi:10.1016/j.electacta.2023.142166.
50. Stett, A.; Egert, U.; Guenther, E.; Hofmann, F.; Meyer, T.; Nisch, W.; Haemmerle, H. Biological Application of Microelectrode Arrays in Drug Discovery and Basic Research. *Anal. Bioanal. Chem.* **2003**, *377*, 486–495,

doi:10.1007/s00216-003-2149-x.
51. THOMASJR, C.; SPRINGER, P.; LOEB, G.; BERWALDNETTER, Y.; OKUN, L. A Miniature Microelectrode Array to Monitor the Bioelectric Activity of Cultured Cells. *Exp. Cell Res.* **1972**, *74*, 61–66, doi:10.1016/0014-4827(72)90481-8.
52. Gross, G.W.; Rieske, E.; Kreutzberg, G.W.; Meyer, A. A New Fixed-Array Multi-Microelectrode System Designed for Long-Term Monitoring of Extracellular Single Unit Neuronal Activity in Vitro. *Neurosci. Lett.* **1977**, *6*, 101–105, doi:10.1016/0304-3940(77)90003-9.
53. Pine, J. Recording Action Potentials from Cultured Neurons with Extracellular Microcircuit Electrodes. *J. Neurosci. Methods* **1980**, *2*, 19–31, doi:10.1016/0165-0270(80)90042-4.
54. Novak, J.L.; Wheeler, B.C. Multisite Hippocampal Slice Recording and Stimulation Using a 32 Element Microelectrode Array. *J. Neurosci. Methods* **1988**, *23*, 149–159, doi:10.1016/0165-0270(88)90187-2.
55. Borkholder, D.A.; Bao, J.; Maluf, N.I.; Perl, E.R.; Kovacs, G.T. Microelectrode Arrays for Stimulation of Neural Slice Preparations. *J. Neurosci. Methods* **1997**, *77*, 61–66, doi:10.1016/s0165-0270(97)00112-x.
56. Hafizovic, S.; Heer, F.; Ugniwenko, T.; Frey, U.; Blau, A.; Ziegler, C.; Hierlemann, A. A CMOS-Based Microelectrode Array for Interaction with Neuronal Cultures. *J. Neurosci. Methods* **2007**, *164*, 93–106, doi:10.1016/j.jneumeth.2007.04.006.
57. Berdondini, L.; Imfeld, K.; Maccione, A.; Tedesco, M.; Neukom, S.; Koudelka-Hep, M.; Martinoia, S. Active Pixel Sensor Array for High Spatio-Temporal Resolution Electrophysiological Recordings from Single Cell to Large Scale Neuronal Networks. *Lab Chip* **2009**, *9*, 2644–2651, doi:10.1039/b907394a.
58. Ballini, M.; Müller, J.; Livi, P.; Chen, Y.; Frey, U.; Stettler, A.; Shadmani, A.; Viswam, V.; Jones, I.L.; Jäckel, D.; et al. A 1024-Channel CMOS Microelectrode Array With 26,400 Electrodes for Recording and Stimulation of Electrogenic Cells In Vitro. *IEEE J. Solid-State Circuits* **2014**, *49*, 2705–2719, doi:10.1109/JSSC.2014.2359219.
59. Wagenaar, D.A.; Pine, J.; Potter, S.M. An Extremely Rich Repertoire of Bursting Patterns during the Development of Cortical Cultures. *BMC Neurosci.* **2006**, *7*, 11, doi:10.1186/1471-2202-7-11.
60. Gramowski, A.; Jügelt, K.; Weiss, D.G.; Gross, G.W. Substance Identification by Quantitative Characterization of Oscillatory Activity in Murine Spinal Cord Networks on Microelectrode Arrays. *Eur. J. Neurosci.* **2004**, *19*, 2815–2825, doi:10.1111/j.0953-816X.2004.03373.x.
61. Meyer, T.; Boven, K.-H.; Günther, E.; Fejtl, M. Micro-Electrode Arrays in Cardiac Safety Pharmacology: A Novel Tool to Study QT Interval Prolongation. *Drug Saf.* **2004**, *27*, 763–772, doi:10.2165/00002018-200427110-00002.
62. Leach, J.B.; Achyuta, A.K.H.; Murthy, S.K. Bridging the Divide between Neuroprosthetic Design, Tissue Engineering and Neurobiology. *Front. Neuroeng.* **2010**, *2*, 18, doi:10.3389/neuro.16.018.2009.
63. Qing, Q.; Pal, S.K.; Tian, B.; Duan, X.; Timko, B.P.; Cohen-Karni, T.; Murthy,

V.N.; Lieber, C.M. Nanowire Transistor Arrays for Mapping Neural Circuits in Acute Brain Slices. *Proc. Natl. Acad. Sci. U. S. A.* **2010**, *107*, 1882–1887, doi:10.1073/pnas.0914737107.

64. Frega, M.; Tedesco, M.; Massobrio, P.; Pesce, M.; Williamson, A.; Schober, A.; Martinoia, S. 3D Engineered Neural Networks Coupled to Micro-Electrode Arrays: Development of an Innovative in-Vitro Experimental Model for Neurophysiological Studies. In Proceedings of the 2013 6th International IEEE/EMBS Conference on Neural Engineering (NER); IEEE, November 2013; pp. 957–960.
65. Lancaster, M.A.; Renner, M.; Martin, C.-A.; Wenzel, D.; Bicknell, L.S.; Hurles, M.E.; Homfray, T.; Penninger, J.M.; Jackson, A.P.; Knoblich, J.A. Cerebral Organoids Model Human Brain Development and Microcephaly. *Nature* **2013**, *501*, 373–379, doi:10.1038/nature12517.
66. Hai, A.; Shappir, J.; Spira, M.E. In-Cell Recordings by Extracellular Microelectrodes. *Nat. Methods* **2010**, *7*, 200–202, doi:10.1038/nmeth.1420.
67. Simitzi, C.; Ranella, A.; Stratakis, E. Controlling the Morphology and Outgrowth of Nerve and Neuroglial Cells: The Effect of Surface Topography. *Acta Biomater.* **2017**, *51*, 21–52, doi:10.1016/j.actbio.2017.01.023.
68. Qing, Q.; Jiang, Z.; Xu, L.; Gao, R.; Mai, L.; Lieber, C.M. Free-Standing Kinked Nanowire Transistor Probes for Targeted Intracellular Recording in Three Dimensions. *Nat. Nanotechnol.* **2014**, *9*, 142–147, doi:10.1038/nnano.2013.273.
69. Geramifard, N.; Lawson, J.; Cogan, S.F.; Black, B.J. A Novel 3D Helical Microelectrode Array for In Vitro Extracellular Action Potential Recording. *Micromachines* **2022**, *13*, doi:10.3390/mi13101692.
70. Schmidt, S.; Frank, R.; Krinke, D.; Jahnke, H.-G.; Robitzki, A.A. Novel PMMA Based 96-Well Microelectrode Arrays for Bioelectronic High Throughput Monitoring of Cells in a Live Mode. *Biosens. Bioelectron.* **2022**, *202*, 114012, doi:10.1016/j.bios.2022.114012.
71. Cho, Y.H.; Park, Y.-G.; Kim, S.; Park, J.-U. 3D Electrodes for Bioelectronics. *Adv. Mater.* **2021**, *33*, e2005805, doi:10.1002/adma.202005805.
72. Minev, I.R.; Wenger, N.; Courtine, G.; Lacour, S.P. Research Update: Platinum-Elastomer Mesocomposite as Neural Electrode Coating. *APL Mater.* **2015**, *3*, doi:10.1063/1.4906502.
73. Aregueta-Robles, U.A.; Woolley, A.J.; Poole-Warren, L.A.; Lovell, N.H.; Green, R.A. Organic Electrode Coatings for Next-Generation Neural Interfaces. *Front. Neuroeng.* **2014**, *7*, 15, doi:10.3389/fneng.2014.00015.
74. Green, R.A.; Lovell, N.H.; Wallace, G.G.; Poole-Warren, L.A. Conducting Polymers for Neural Interfaces: Challenges in Developing an Effective Long-Term Implant. *Biomaterials* **2008**, *29*, 3393–3399, doi:10.1016/j.biomaterials.2008.04.047.
75. Schendel, A.A.; Eliceiri, K.W.; Williams, J.C. Advanced Materials for Neural Surface Electrodes. *Curr. Opin. Solid State Mater. Sci.* **2014**, *18*, 301–307, doi:10.1016/j.cossms.2014.09.006.
76. Kaur, G.; Adhikari, R.; Cass, P.; Bown, M.; Gunatillake, P. Electrically Conductive Polymers and Composites for Biomedical Applications. *RSC Adv.* **2015**, *5*, 37553–37567, doi:10.1039/C5RA01851J.

77. Huang, Y.; Kormakov, S.; He, X.; Gao, X.; Zheng, X.; Liu, Y.; Sun, J.; Wu, D. Conductive Polymer Composites from Renewable Resources: An Overview of Preparation, Properties, and Applications. *Polymers (Basel).* **2019**, *11*, 187, doi:10.3390/polym11020187.
78. Wang, Y.; Gao, Y.; Pan, Y.; Zhou, D.; Liu, Y.; Yin, Y.; Yang, J.; Wang, Y.; Song, Y. Emerging Trends in Organ-on-a-Chip Systems for Drug Screening. *Acta Pharm. Sin. B* **2023**, *13*, 2483–2509, doi:10.1016/j.apsb.2023.02.006.
79. López Barreiro, D.; Martín-Moldes, Z.; Yeo, J.; Shen, S.; Hawker, M.J.; Martin-Martinez, F.J.; Kaplan, D.L.; Buehler, M.J. Conductive Silk-Based Composites Using Biobased Carbon Materials. *Adv. Mater.* **2019**, *31*, e1904720, doi:10.1002/adma.201904720.
80. Viswam, V.; Obien, M.E.J.; Franke, F.; Frey, U.; Hierlemann, A. Optimal Electrode Size for Multi-Scale Extracellular-Potential Recording From Neuronal Assemblies. *Front. Neurosci.* **2019**, *13*, doi:10.3389/fnins.2019.00385.
81. Wei, X.; Luan, L.; Zhao, Z.; Li, X.; Zhu, H.; Potnis, O.; Xie, C. Nanofabricated Ultraflexible Electrode Arrays for High-Density Intracortical Recording. *Adv. Sci. (Weinheim, Baden-Wurttemberg, Ger.* **2018**, *5*, 1700625, doi:10.1002/advs.201700625.
82. Hughes, M.P.; Bustamante, K.; Banks, D.J.; Ewins, D.J. Effects of Electrode Size on the Performance of Neural Recording Microelectrodes. In Proceedings of the 1st Annual International IEEE-EMBS Special Topic Conference on Microtechnologies in Medicine and Biology. Proceedings (Cat. No.00EX451); IEEE, 2000; pp. 220–223.
83. Kotani, Y.; Sawahata, H.; Yamagiwa, S.; Numano, R.; Koida, K.; Kawano, T. A High-Density Array of 3D Microneedle-Electrodes for Evaluation of Spatial Resolution of Neuronal Activity. In Proceedings of the 2019 20th International Conference on Solid-State Sensors, Actuators and Microsystems & Eurosensors XXXIII (TRANSDUCERS & EUROSENSORS XXXIII); IEEE, June 1 2019; pp. 2205–2208.
84. Frey, U.; Egert, U.; Heer, F.; Hafizovic, S.; Hierlemann, A. Microelectronic System for High-Resolution Mapping of Extracellular Electric Fields Applied to Brain Slices. *Biosens. Bioelectron.* **2009**, *24*, 2191–2198, doi:10.1016/j.bios.2008.11.028.
85. Jun, J.J.; Steinmetz, N.A.; Siegle, J.H.; Denman, D.J.; Bauza, M.; Barbarits, B.; Lee, A.K.; Anastassiou, C.A.; Andrei, A.; Aydın, Ç.; et al. Fully Integrated Silicon Probes for High-Density Recording of Neural Activity. *Nature* **2017**, *551*, 232–236, doi:10.1038/nature24636.
86. Smith, M.A.; Berry, S.; Parameswaran, L.; Holtsberg, C.; Siegel, N.; Lockwood, R.; Chrisp, M.P.; Freeman, D.; Rothschild, M. Design, Simulation, and Fabrication of Three-Dimensional Microsystem Components Using Grayscale Photolithography. *J. Micro/Nanolithography, MEMS, MOEMS* **2019**, *18*, 1, doi:10.1117/1.JMM.18.4.043507.
87. Mofazzal Jahromi, M.A.; Abdoli, A.; Rahmanian, M.; Bardania, H.; Bayandori, M.; Moosavi Basri, S.M.; Kalbasi, A.; Aref, A.R.; Karimi, M.; Hamblin, M.R. Microfluidic Brain-on-a-Chip: Perspectives for Mimicking Neural System Disorders. *Mol. Neurobiol.* **2019**, *56*, 8489–8512,

doi:10.1007/s12035-019-01653-2.
88. Urness, A.C.; Moore, E.D.; Kamysiak, K.K.; Cole, M.C.; McLeod, R.R. Liquid Deposition Photolithography for Submicrometer Resolution Three-Dimensional Index Structuring with Large Throughput. *Light Sci. Appl.* **2013**, *2*, e56–e56, doi:10.1038/lsa.2013.12.
89. Paik, S.; Kim, G.; Chang, S.; Lee, S.; Jin, D.; Jeong, K.-Y.; Lee, I.S.; Lee, J.; Moon, H.; Lee, J.; et al. Near-Field Sub-Diffraction Photolithography with an Elastomeric Photomask. *Nat. Commun.* **2020**, *11*, 805, doi:10.1038/s41467-020-14439-1.
90. Whitesides, G.M.; Ostuni, E.; Takayama, S.; Jiang, X.; Ingber, D.E. Soft Lithography in Biology and Biochemistry. *Annu. Rev. Biomed. Eng.* **2001**, *3*, 335–373, doi:10.1146/annurev.bioeng.3.1.335.
91. Yadav, N.; Lorenzelli, L.; Giacomozzi, F. A Novel Additive Manufacturing Approach towards Fabrication of Multi-Level Three-Dimensional Microelectrode Array for Electrophysiological Investigations. In Proceedings of the 2021 23rd European Microelectronics and Packaging Conference & Exhibition (EMPC); IEEE, September 13 2021; pp. 1–5.
92. Didier, C.M.; Kundu, A.; DeRoo, D.; Rajaraman, S. Development of in Vitro 2D and 3D Microelectrode Arrays and Their Role in Advancing Biomedical Research. *J. Micromechanics Microengineering* **2020**, *30*, 103001, doi:10.1088/1361-6439/ab8e91.
93. Gudapati, H.; Dey, M.; Ozbolat, I. A Comprehensive Review on Droplet-Based Bioprinting: Past, Present and Future. *Biomaterials* **2016**, *102*, 20–42, doi:10.1016/j.biomaterials.2016.06.012.
94. Zilinskaite, N.; Shukla, R.P.; Baradoke, A. Use of 3D Printing Techniques to Fabricate Implantable Microelectrodes for Electrochemical Detection of Biomarkers in the Early Diagnosis of Cardiovascular and Neurodegenerative Diseases. *ACS Meas. Sci. Au* **2023**, *3*, 315–336, doi:10.1021/acsmeasuresciau.3c00028.
95. Grob, L.; Yamamoto, H.; Zips, S.; Rinklin, P.; Hirano-Iwata, A.; Wolfrum, B. Printed 3D Electrode Arrays with Micrometer-Scale Lateral Resolution for Extracellular Recording of Action Potentials. *Adv. Mater. Technol.* **2020**, *5*, doi:10.1002/admt.201900517.
96. Kundu, A.; Rozman, A.; Rajaraman, S. Development of a 3D Printed, Self-Insulated, High-Throughput 3D Microelectrode Array (HT-3DMEA). *J. Microelectromechanical Syst.* **2020**, *29*, 1091–1093, doi:10.1109/JMEMS.2020.3003644.
97. Hopkins, A.M.; DeSimone, E.; Chwalek, K.; Kaplan, D.L. 3D in Vitro Modeling of the Central Nervous System. *Prog. Neurobiol.* **2015**, *125*, 1–25, doi:10.1016/j.pneurobio.2014.11.003.
98. Kim, G.; Kim, K.; Lee, E.; An, T.; Choi, W.; Lim, G.; Shin, J. Recent Progress on Microelectrodes in Neural Interfaces. *Materials (Basel).* **2018**, *11*, 1995, doi:10.3390/ma11101995.
99. Heim, M.; Yvert, B.; Kuhn, A. Nanostructuration Strategies to Enhance Microelectrode Array (MEA) Performance for Neuronal Recording and Stimulation. *J. Physiol. Paris* **2012**, *106*, 137–145, doi:10.1016/j.jphysparis.2011.10.001.

100. Novoselov, K.S.; Geim, A.K.; Morozov, S. V; Jiang, D.; Zhang, Y.; Dubonos, S. V; Grigorieva, I. V; Firsov, A.A. Electric Field Effect in Atomically Thin Carbon Films. *Science* **2004**, *306*, 666–669, doi:10.1126/science.1102896.
101. Fabbro, A.; Scaini, D.; León, V.; Vázquez, E.; Cellot, G.; Privitera, G.; Lombardi, L.; Torrisi, F.; Tomarchio, F.; Bonaccorso, F.; et al. Graphene-Based Interfaces Do Not Alter Target Nerve Cells. *ACS Nano* **2016**, *10*, 615–623, doi:10.1021/acsnano.5b05647.
102. Bareket-Keren, L.; Hanein, Y. Carbon Nanotube-Based Multi Electrode Arrays for Neuronal Interfacing: Progress and Prospects. *Front. Neural Circuits* **2013**, *6*, 35286, doi:10.3389/fncir.2012.00122.
103. Vafaiee, M.; Mohammadpour, R.; Vossoughi, M.; Asadian, E.; Janahmadi, M.; Sasanpour, P. Carbon Nanotube Modified Microelectrode Array for Neural Interface. *Front. Bioeng. Biotechnol.* **2021**, *8*, 582713, doi:10.3389/fbioe.2020.582713.
104. Purcell, E.; Becker, M.; Guo, Y.; Hara, S.; Ludwig, K.; McKinney, C.; Monroe, E.; Rechenberg, R.; Rusinek, C.; Saxena, A.; et al. Next-Generation Diamond Electrodes for Neurochemical Sensing: Challenges and Opportunities. *Micromachines* **2021**, *12*, 128, doi:10.3390/mi12020128.
105. Richardson, R.T.; Wise, A.K.; Thompson, B.C.; Flynn, B.O.; Atkinson, P.J.; Fretwell, N.J.; Fallon, J.B.; Wallace, G.G.; Shepherd, R.K.; Clark, G.M.; et al. Polypyrrole-Coated Electrodes for the Delivery of Charge and Neurotrophins to Cochlear Neurons. *Biomaterials* **2009**, *30*, 2614–2624, doi:10.1016/j.biomaterials.2009.01.015.
106. Green, R.A.; Lovell, N.H.; Poole-Warren, L.A. Cell Attachment Functionality of Bioactive Conducting Polymers for Neural Interfaces. *Biomaterials* **2009**, *30*, 3637–3644, doi:10.1016/j.biomaterials.2009.03.043.
107. Yang, X.; Zhou, T.; Zwang, T.J.; Hong, G.; Zhao, Y.; Viveros, R.D.; Fu, T.-M.; Gao, T.; Lieber, C.M. Bioinspired Neuron-like Electronics. *Nat. Mater.* **2019**, *18*, 510–517, doi:10.1038/s41563-019-0292-9.
108. Tian, B.; Cohen-Karni, T.; Qing, Q.; Duan, X.; Xie, P.; Lieber, C.M. Three-Dimensional, Flexible Nanoscale Field-Effect Transistors as Localized Bioprobes. *Science* **2010**, *329*, 830–834, doi:10.1126/science.1192033.
109. Keefer, E.W.; Botterman, B.R.; Romero, M.I.; Rossi, A.F.; Gross, G.W. Carbon Nanotube Coating Improves Neuronal Recordings. *Nat. Nanotechnol.* **2008**, *3*, 434–439, doi:10.1038/nnano.2008.174.
110. Bharucha, E.; Sepehrian, H.; Gosselin, B. A Survey of Neural Front End Amplifiers and Their Requirements toward Practical Neural Interfaces. *J. Low Power Electron. Appl.* **2014**, *4*, 268–291, doi:10.3390/jlpea4040268.
111. Jochum, T.; Denison, T.; Wolf, P. Integrated Circuit Amplifiers for Multi-Electrode Intracortical Recording. *J. Neural Eng.* **2009**, *6*, 012001, doi:10.1088/1741-2560/6/1/012001.
112. Krasteva, V.T.; Papazov, S.P. Estimation of Current Density Distribution under Electrodes for External Defibrillation. *Biomed. Eng. Online* **2002**, *1*, *7*, doi:10.1186/1475-925x-1-7.
113. Liu, Y.; Pereira, J.L.; Constandinou, T.G. Event-Driven Processing for Hardware-Efficient Neural Spike Sorting. *J. Neural Eng.* **2018**, *15*, 016016, doi:10.1088/1741-2552/aa9124.

114. Novellino, A.; Chiappalone, M.; Maccione, A.; Martinoia, S. Neural Signal Manager: A Collection of Classical and Innovative Tools for Multi-channel Spike Train Analysis. *Int. J. Adapt. Control Signal Process.* **2009**, *23*, 999–1013, doi:10.1002/acs.1076.
115. Lewicki, M.S. A Review of Methods for Spike Sorting: The Detection and Classification of Neural Action Potentials. *Network* **1998**, *9*, R53-78.
116. Bakkum, D.J.; Frey, U.; Radivojevic, M.; Russell, T.L.; Müller, J.; Fiscella, M.; Takahashi, H.; Hierlemann, A. Tracking Axonal Action Potential Propagation on a High-Density Microelectrode Array across Hundreds of Sites. *Nat. Commun.* **2013**, *4*, 2181, doi:10.1038/ncomms3181.
117. Einevoll, G.T.; Franke, F.; Hagen, E.; Pouzat, C.; Harris, K.D. Towards Reliable Spike-Train Recordings from Thousands of Neurons with Multielectrodes. *Curr. Opin. Neurobiol.* **2012**, *22*, 11–17, doi:10.1016/j.conb.2011.10.001.
118. Eke, G.; Vaysse, L.; Yao, X.; Escudero, M.; Carrière, A.; Trevisiol, E.; Vieu, C.; Dani, C.; Casteilla, L.; Malaquin, L. Cell Aggregate Assembly through Microengineering for Functional Tissue Emergence. *Cells* **2022**, *11*, doi:10.3390/cells11091394.
119. Gallego-Perez, D.; Higuita-Castro, N.; Sharma, S.; Reen, R.K.; Palmer, A.F.; Gooch, K.J.; Lee, L.J.; Lannutti, J.J.; Hansford, D.J. High Throughput Assembly of Spatially Controlled 3D Cell Clusters on a Micro/Nanoplatform. *Lab Chip* **2010**, *10*, 775, doi:10.1039/b919475d.
120. Napolitano, A.P.; Dean, D.M.; Man, A.J.; Youssef, J.; Ho, D.N.; Rago, A.P.; Lech, M.P.; Morgan, J.R. Scaffold-Free Three-Dimensional Cell Culture Utilizing Micromolded Nonadhesive Hydrogels. *Biotechniques* **2007**, *43*, 494, 496–500, doi:10.2144/000112591.
121. Brisson, V.; Tilton, R.D. Self-Assembly and Two-Dimensional Patterning of Cell Arrays by Electrophoretic Deposition. *Biotechnol. Bioeng.* **2002**, *77*, 290–295, doi:10.1002/bit.10146.
122. de Groot, T.E.; Veserat, K.S.; Berthier, E.; Beebe, D.J.; Theberge, A.B. Surface-Tension Driven Open Microfluidic Platform for Hanging Droplet Culture. *Lab Chip* **2016**, *16*, 334–344, doi:10.1039/c5lc01353d.
123. Timmins, N.E.; Nielsen, L.K. Generation of Multicellular Tumor Spheroids by the Hanging-Drop Method. *Methods Mol. Med.* **2007**, *140*, 141–151, doi:10.1007/978-1-59745-443-8_8.
124. Banerjee, M.; Bhonde, R.R. Application of Hanging Drop Technique for Stem Cell Differentiation and Cytotoxicity Studies. *Cytotechnology* **2006**, *51*, 1–5, doi:10.1007/s10616-006-9001-z.
125. Skowron, M.A.; Watolla, M.M.; Nettersheim, D. Three-Dimensional Cultivation of Germ Cell Cancer Cell Lines as Hanging Drops. *Methods Mol. Biol.* **2021**, *2195*, 77–83, doi:10.1007/978-1-0716-0860-9_6.
126. Tekin, H.; Anaya, M.; Brigham, M.D.; Nauman, C.; Langer, R.; Khademhosseini, A. Stimuli-Responsive Microwells for Formation and Retrieval of Cell Aggregates. *Lab Chip* **2010**, *10*, 2411–2418, doi:10.1039/c004732e.
127. Selimović, Š.; Piraino, F.; Bae, H.; Rasponi, M.; Redaelli, A.; Khademhosseini, A. Microfabricated Polyester Conical Microwells for Cell

Culture Applications. *Lab Chip* **2011**, *11*, 2325, doi:10.1039/c1lc20213h.
128. Forget, A.; Burzava, A.L.S.; Delalat, B.; Vasilev, K.; Harding, F.J.; Blencowe, A.; Voelcker, N.H. Rapid Fabrication of Functionalised Poly(Dimethylsiloxane) Microwells for Cell Aggregate Formation. *Biomater. Sci.* **2017**, *5*, 828–836, doi:10.1039/c6bm00916f.
129. Ochsner, M.; Dusseiller, M.R.; Grandin, H.M.; Luna-Morris, S.; Textor, M.; Vogel, V.; Smith, M.L. Micro-Well Arrays for 3D Shape Control and High Resolution Analysis of Single Cells. *Lab Chip* **2007**, *7*, 1074–1077, doi:10.1039/b704449f.
130. Hoffman, A.S. Hydrogels for Biomedical Applications. *Adv. Drug Deliv. Rev.* **2012**, *64*, 18–23, doi:10.1016/j.addr.2012.09.010.
131. Langer, R.; Vacanti, J.P. Tissue Engineering. *Science (80-.).* **1993**, *260*, 920–926, doi:10.1126/science.8493529.
132. Groll, J.; Burdick, J.A.; Cho, D.-W.; Derby, B.; Gelinsky, M.; Heilshorn, S.C.; Jüngst, T.; Malda, J.; Mironov, V.A.; Nakayama, K.; et al. A Definition of Bioinks and Their Distinction from Biomaterial Inks. *Biofabrication* **2018**, *11*, 013001, doi:10.1088/1758-5090/aaec52.
133. Yu, L.; Ding, J. Injectable Hydrogels as Unique Biomedical Materials. *Chem. Soc. Rev.* **2008**, *37*, 1473–1481, doi:10.1039/b713009k.
134. Orive, G.; Hernández, R.M.; Gascón, A.R.; Calafiore, R.; Chang, T.M.S.; De Vos, P.; Hortelano, G.; Hunkeler, D.; Lacík, I.; Shapiro, A.M.J.; et al. Cell Encapsulation: Promise and Progress. *Nat. Med.* **2003**, *9*, 104–107, doi:10.1038/nm0103-104.
135. Hwang, C.M.; Sant, S.; Masaeli, M.; Kachouie, N.N.; Zamanian, B.; Lee, S.-H.; Khademhosseini, A. Fabrication of Three-Dimensional Porous Cell-Laden Hydrogel for Tissue Engineering. *Biofabrication* **2010**, *2*, 035003, doi:10.1088/1758-5082/2/3/035003.
136. Bae, K.H.; Yoon, J.J.; Park, T.G. Fabrication of Hyaluronic Acid Hydrogel Beads for Cell Encapsulation. *Biotechnol. Prog.* **2006**, *22*, 297–302, doi:10.1021/bp050312b.
137. Jabbari, E. Hydrogels for Cell Delivery. *Gels* **2018**, *4*, 58, doi:10.3390/gels4030058.
138. Ling, Y.; Rubin, J.; Deng, Y.; Huang, C.; Demirci, U.; Karp, J.M.; Khademhosseini, A. A Cell-Laden Microfluidic Hydrogel. *Lab Chip* **2007**, *7*, 756–762, doi:10.1039/b615486g.
139. Robinson, D.A. The Electrical Properties of Metal Microelectrodes. *Proc. IEEE* **1968**, *56*, 1065–1071, doi:10.1109/PROC.1968.6458.
140. Nam, Y.; Wheeler, B.C. In Vitro Microelectrode Array Technology and Neural Recordings. *Crit. Rev. Biomed. Eng.* **2011**, *39*, 45–61, doi:10.1615/critrevbiomedeng.v39.i1.40.
141. Ruiz-Amaya, J.; Rodriguez-Perez, A.; Delgado-Restituto, M. A Review of Low-Noise Amplifiers for Neural Applications. In Proceedings of the 2010 2nd Circuits and Systems for Medical and Environmental Applications Workshop (CASME); IEEE, 2010; pp. 1–4.
142. Lee, T.; Jang, D.; Jung, Y.; Jeon, H.; Hong, S.; Han, S.; Chu, J.-U.; Lee, J.; Je, M. A Neural Recording Amplifier Based on Adaptive SNR Optimization Technique for Long-Term Implantation. In Proceedings of the 2017 IEEE

Biomedical Circuits and Systems Conference (BioCAS); IEEE, October 2 2017; Vol. 2018-January, pp. 1–4.
143. Taghavi, M.H.; Belostotski, L.; Haslett, J.W. Signal-to-Noise-Ratio-Constrained Jitter Optimization for Wideband Amplifiers. In Proceedings of the 2012 25th IEEE Canadian Conference on Electrical and Computer Engineering (CCECE); IEEE, April 2012; pp. 1–4.
144. Cogan, S.F. Neural Stimulation and Recording Electrodes. *Annu. Rev. Biomed. Eng.* **2008**, *10*, 275–309, doi:10.1146/annurev.bioeng.10.061807.160518.
145. Fattahi, P.; Yang, G.; Kim, G.; Abidian, M.R. A Review of Organic and Inorganic Biomaterials for Neural Interfaces. *Adv. Mater.* **2014**, *26*, 1846–1885, doi:10.1002/adma.201304496.
146. Warren, D.; Tomaskovic-Crook, E.; Wallace, G.G.; Crook, J.M. Engineering in Vitro Human Neural Tissue Analogs by 3D Bioprinting and Electrostimulation. *APL Bioeng.* **2021**, *5*, 020901, doi:10.1063/5.0032196.
147. Boyden, E.S.; Zhang, F.; Bamberg, E.; Nagel, G.; Deisseroth, K. Millisecond-Timescale, Genetically Targeted Optical Control of Neural Activity. *Nat. Neurosci.* **2005**, *8*, 1263–1268, doi:10.1038/nn1525.
148. Brette, R.; Destexhe, A. Intracellular Recording. In *Handbook of Neural Activity Measurement*; Cambridge University Press, 2012; pp. 44–91.
149. Bruno, G.; Colistra, N.; Melle, G.; Cerea, A.; Hubarevich, A.; Deleye, L.; De Angelis, F.; Dipalo, M. Microfluidic Multielectrode Arrays for Spatially Localized Drug Delivery and Electrical Recordings of Primary Neuronal Cultures. *Front. Bioeng. Biotechnol.* **2020**, *8*, doi:10.3389/FBIOE.2020.00626/PDF.
150. Pelkonen, A.; Pistono, C.; Klecki, P.; Gómez-Budia, M.; Dougalis, A.; Konttinen, H.; Stanová, I.; Fagerlund, I.; Leinonen, V.; Korhonen, P.; et al. Functional Characterization of Human Pluripotent Stem Cell-Derived Models of the Brain with Microelectrode Arrays. *Cells* **2021**, *11*, 106, doi:10.3390/cells11010106.
151. Venkataraman, L.; Fair, S.R.; McElroy, C.A.; Hester, M.E.; Fu, H. Modeling Neurodegenerative Diseases with Cerebral Organoids and Other Three-Dimensional Culture Systems: Focus on Alzheimer's Disease. *Stem cell Rev. reports* **2022**, *18*, 696–717, doi:10.1007/s12015-020-10068-9.
152. Park, J.; Wetzel, I.; Marriott, I.; Dréau, D.; D'Avanzo, C.; Kim, D.Y.; Tanzi, R.E.; Cho, H. A 3D Human Triculture System Modeling Neurodegeneration and Neuroinflammation in Alzheimer's Disease. *Nat. Neurosci.* **2018**, *21*, 941–951, doi:10.1038/s41593-018-0175-4.
153. Krokidis, M.G.; Exarchos, T.P.; Vlamos, P. Data-Driven Biomarker Analysis Using Computational Omics Approaches to Assess Neurodegenerative Disease Progression. *Math. Biosci. Eng.* **2021**, *18*, 1813–1832, doi:10.3934/mbe.2021094.
154. Hsiao, M.-C.; Yu, P.-N.; Song, D.; Liu, C.Y.; Heck, C.N.; Millett, D.; Berger, T.W. An in Vitro Seizure Model from Human Hippocampal Slices Using Multi-Electrode Arrays. *J. Neurosci. Methods* **2015**, *244*, 154–163, doi:10.1016/j.jneumeth.2014.09.010.
155. Dossi, E.; Blauwblomme, T.; Nabbout, R.; Huberfeld, G.; Rouach, N. Multi-

Electrode Array Recordings of Human Epileptic Postoperative Cortical Tissue. *J. Vis. Exp.* **2014**, e51870, doi:10.3791/51870.
156. Hill, A.J.; Jones, N.A.; Williams, C.M.; Stephens, G.J.; Whalley, B.J. Development of Multi-Electrode Array Screening for Anticonvulsants in Acute Rat Brain Slices. *J. Neurosci. Methods* **2010**, *185*, 246–256, doi:10.1016/j.jneumeth.2009.10.007.
157. Engel, J. Mesial Temporal Lobe Epilepsy: What Have We Learned? *Neuroscientist* **2001**, *7*, 340–352, doi:10.1177/107385840100700410.
158. Bliss, T.V.P.; Collingridge, G.L. A Synaptic Model of Memory: Long-Term Potentiation in the Hippocampus. *Nature* **1993**, *361*, 31–39, doi:10.1038/361031a0.
159. Biran, R.; Martin, D.C.; Tresco, P.A. Neuronal Cell Loss Accompanies the Brain Tissue Response to Chronically Implanted Silicon Microelectrode Arrays. *Exp. Neurol.* **2005**, *195*, 115–126, doi:10.1016/j.expneurol.2005.04.020.
160. Ioannidis, J.P.A.; Greenland, S.; Hlatky, M.A.; Khoury, M.J.; Macleod, M.R.; Moher, D.; Schulz, K.F.; Tibshirani, R. Increasing Value and Reducing Waste in Research Design, Conduct, and Analysis. *Lancet (London, England)* **2014**, *383*, 166–175, doi:10.1016/S0140-6736(13)62227-8.
161. Kotov, N.A.; Winter, J.O.; Clements, I.P.; Jan, E.; Timko, B.P.; Campidelli, S.; Pathak, S.; Mazzatenta, A.; Lieber, C.M.; Prato, M.; et al. Nanomaterials for Neural Interfaces. *Adv. Mater.* **2009**, *21*, 3970–4004, doi:10.1002/adma.200801984.
162. Cho, Y.; Park, S.; Lee, J.; Yu, K.J. Emerging Materials and Technologies with Applications in Flexible Neural Implants: A Comprehensive Review of Current Issues with Neural Devices. *Adv. Mater.* **2021**, *33*, e2005786, doi:10.1002/adma.202005786.
163. Pachitariu, M.; Steinmetz, N.; Kadir, S.; Carandini, M.; D., H.K. Kilosort: Realtime Spike-Sorting for Extracellular Electrophysiology with Hundreds of Channels. *bioRxiv* **2016**, 061481, doi:doi.org/10.1101/061481.
164. Mishchenko, Y.; Vogelstein, J.T.; Paninski, L. A Bayesian Approach for Inferring Neuronal Connectivity from Calcium Fluorescent Imaging Data. *Ann. Appl. Stat.* **2011**, *5*, 1229–1261, doi:10.1214/09-AOAS303.
165. Mestre, A.L.G.; Cerquido, M.; Inácio, P.M.C.; Asgarifar, S.; Lourenço, A.S.; Cristiano, M.L.S.; Aguiar, P.; Medeiros, M.C.R.; Araújo, I.M.; Ventura, J.; et al. Ultrasensitive Gold Micro-Structured Electrodes Enabling the Detection of Extra-Cellular Long-Lasting Potentials in Astrocytes Populations. *Sci. Reports 2017 71* **2017**, *7*, 1–11, doi:10.1038/s41598-017-14697-y.
166. Weremfo, A.; Carter, P.; Hibbert, D.B.; Zhao, C. Investigating the Interfacial Properties of Electrochemically Roughened Platinum Electrodes for Neural Stimulation. *Langmuir* **2015**, *31*, 2593–2599, doi:10.1021/la504876n.
167. Dini, J.W. *Electrodeposition: The Materials Science of Coatings and Substrates*; 1st Edition.; Noyes Publications, 1993; ISBN 9780815513209.
168. Rutten, W.L.C. Selective Electrical Interfaces with the Nervous System. *Annu. Rev. Biomed. Eng.* **2002**, *4*, 407–452, doi:10.1146/annurev.bioeng.4.020702.153427.
169. Shah, K.G.; Tolosa, V.M.; Tooker, A.C.; Felix, S.H.; Pannu, S.S. Improved

Chronic Neural Stimulation Using High Surface Area Platinum Electrodes. *Annu. Int. Conf. IEEE Eng. Med. Biol. Soc. IEEE Eng. Med. Biol. Soc. Annu. Int. Conf.* **2013**, *2013*, 1546–1549, doi:10.1109/EMBC.2013.6609808.

170. Weidlich, S.; Krause, K.J.; Schnitker, J.; Wolfrum, B.; Offenhäusser, A. MEAs and 3D Nanoelectrodes: Electrodeposition as Tool for a Precisely Controlled Nanofabrication. *Nanotechnology* **2017**, *28*, 095302, doi:10.1088/1361-6528/aa57b5.
171. Dharmadasa, I.M.; Haigh, J. Strengths and Advantages of Electrodeposition as a Semiconductor Growth Technique for Applications in Macroelectronic Devices. *J. Electrochem. Soc.* **2006**, *153*, G47, doi:10.1149/1.2128120.
172. Ortigoza-Diaz, J.; Scholten, K.; Larson, C.; Cobo, A.; Hudson, T.; Yoo, J.; Baldwin, A.; Weltman Hirschberg, A.; Meng, E. Techniques and Considerations in the Microfabrication of Parylene C Microelectromechanical Systems. *Micromachines* **2018**, *9*, 422, doi:10.3390/mi9090422.
173. Ning, F.; Cong, W. Ultrasonic Vibration-Assisted (UV-A) Manufacturing Processes: State of the Art and Future Perspectives. *J. Manuf. Process.* **2020**, *51*, 174–190, doi:10.1016/j.jmapro.2020.01.028.
174. Wei, C.; Shixing, W.; Libo, Z.; Jinhui, P.; Gengwei, Z. The Application of Ultrasound Technology in the Field of the Precious Metal. *Russ. J. Non-Ferrous Met.* **2015**, *56*, 417–427, doi:10.3103/S1067821215040215.
175. Hyde, M.E.; Compton, R.G. How Ultrasound Influences the Electrodeposition of Metals. *J. Electroanal. Chem.* **2002**, *531*, 19–24, doi:10.1016/S0022-0728(02)01016-1.
176. Gadkari, S.A.; Nayfeh, T.H. Micro Fabrication Using Electro Deposition and Ultrasonic Acoustic Liquid Manipulation. *Int. J. Adv. Manuf. Technol.* **2008**, *39*, 107–117, doi:10.1007/s00170-007-1196-4.
177. Viventi, J.; Kim, D.-H.; Vigeland, L.; Frechette, E.S.; Blanco, J.A.; Kim, Y.-S.; Avrin, A.E.; Tiruvadi, V.R.; Hwang, S.-W.; Vanleer, A.C.; et al. Flexible, Foldable, Actively Multiplexed, High-Density Electrode Array for Mapping Brain Activity in Vivo. *Nat. Neurosci.* **2011**, *14*, 1599–1605, doi:10.1038/nn.2973.
178. Peng, Q.; Tan, X.; Venkataraman, M.; Militky, J.; Xiong, W.; Mahendran, A.R.; Lammer, H.; Kejzlar, P. Effects of Ultrasonic-Assisted Nickel Pretreatment Method on Electroless Copper Plating over Graphene. *Sci. Rep.* **2022**, *12*, 21159, doi:10.1038/s41598-022-25457-y.
179. Tudela, I.; Zhang, Y.; Pal, M.; Kerr, I.; Mason, T.J.; Cobley, A.J. Ultrasound-Assisted Electrodeposition of Nickel: Effect of Ultrasonic Power on the Characteristics of Thin Coatings. *Surf. Coatings Technol.* **2015**, *264*, 49–59, doi:10.1016/j.surfcoat.2015.01.020.
180. Costa, J.M.; Almeida Neto, A.F. de Ultrasound-Assisted Electrodeposition and Synthesis of Alloys and Composite Materials: A Review. *Ultrason. Sonochem.* **2020**, *68*, 105193, doi:10.1016/j.ultsonch.2020.105193.
181. Bonin, L.; Bains, N.; Vitry, V.; Cobley, A.J. Electroless Deposition of Nickel-Boron Coatings Using Low Frequency Ultrasonic Agitation: Effect of Ultrasonic Frequency on the Coatings. *Ultrasonics* **2017**, *77*, 61–68, doi:10.1016/j.ultras.2017.01.021.

182. Coleman, S.; Roy, S. Electrodeposition of Copper Patterns Using Enface Technique under Ultrasonic Agitation. *J. Appl. Electrochem.* **2015**, *45*, 889–898, doi:10.1007/s10800-015-0823-2.
183. Scherrer, P. Bestimmung Der Größe Und Der Inneren Struktur von Kolloidteilchen Mittels Röntgenstrahlen. *Nachrichten von der Gesellschaft der Wissenschaften zu Göttingen, Math. Klasse 1918*, 98–100.
184. Frega, M.; van Gestel, S.H.C.; Linda, K.; van der Raadt, J.; Keller, J.; Van Rhijn, J.-R.; Schubert, D.; Albers, C.A.; Nadif Kasri, N. Rapid Neuronal Differentiation of Induced Pluripotent Stem Cells for Measuring Network Activity on Micro-Electrode Arrays. *J. Vis. Exp.* **2017**, *2017*, doi:10.3791/54900.
185. Aprile, D.; Fruscione, F.; Baldassari, S.; Fadda, M.; Ferrante, D.; Falace, A.; Buhler, E.; Sartorelli, J.; Represa, A.; Baldelli, P.; et al. TBC1D24 Regulates Axonal Outgrowth and Membrane Trafficking at the Growth Cone in Rodent and Human Neurons. *Cell Death Differ.* **2019**, *26*, 2464–2478, doi:10.1038/s41418-019-0313-x.
186. Bologna, L.L.; Pasquale, V.; Garofalo, M.; Gandolfo, M.; Baljon, P.L.; Maccione, A.; Martinoia, S.; Chiappalone, M. Investigating Neuronal Activity by SPYCODE Multi-Channel Data Analyzer. *Neural Netw.* **2010**, *23*, 685–697, doi:10.1016/j.neunet.2010.05.002.
187. Maccione, A.; Gandolfo, M.; Massobrio, P.; Novellino, A.; Martinoia, S.; Chiappalone, M. A Novel Algorithm for Precise Identification of Spikes in Extracellularly Recorded Neuronal Signals. *J. Neurosci. Methods* **2009**, *177*, 241–249, doi:10.1016/j.jneumeth.2008.09.026.
188. Pasquale, V.; Martinoia, S.; Chiappalone, M. A Self-Adapting Approach for the Detection of Bursts and Network Bursts in Neuronal Cultures. *J. Comput. Neurosci.* **2010**, *29*, 213–229, doi:10.1007/s10827-009-0175-1.
189. Yadav, N.; Giacomozzi, F.; Cian, A.; Giubertoni, D.; Lorenzelli, L. Enhancing the Deposition Rate and Uniformity in 3D Gold Microelectrode Arrays via Ultrasonic-Enhanced Template-Assisted Electrodeposition. *Sensors* **2024**, *24*, 1251, doi:10.3390/s24041251.
190. Yadav, N.; Lisa, D. Di; Giacomozzi, F.; Cian, A.; Giubertoni, D.; Martinoia, S.; Lorenzelli, L. Development of Multi-Depth Probing 3D Microelectrode Array to Record Electrophysiological Activity within Neural Cultures. *J. Micromechanics Microengineering* **2023**, *33*, 115002, doi:10.1088/1361-6439/acf940.

Publications

- **Yadav, N.**; Lorenzelli, L.; Giacomozzi, F. A Novel Additive Manufacturing Approach towards Fabrication of Multi-Level Three-Dimensional Microelectrode Array for Electrophysiological Investigations. In Proceedings of the 2021 23rd European Microelectronics and Packaging Conference & Exhibition (EMPC); IEEE, September 13, 2021; pp. 1–5, doi: 10.23919/EMPC53418.2021.9584948.
- **Yadav, N.**; Lisa, D. Di; Giacomozzi, F.; Cian, A.; Giubertoni, D.; Martinoia, S.; Lorenzelli, L. Development of Multi-Depth Probing 3D Microelectrode Array to Record Electrophysiological Activity within Neural Cultures. *J. Micromechanics Microengineering* 2023, *33*, 115002, doi:10.1088/1361-6439/acf940.
- **Yadav, N.**; Giacomozzi, F.; Cian, A.; Giubertoni, D.; Lorenzelli, L. Enhancing the Deposition Rate and Uniformity in 3D Gold Microelectrode Arrays via Ultrasonic-Enhanced Template-Assisted Electrodeposition. *Sensors* 2024, *24*, 1251, doi:10.3390/s24041251.

Conferences, Workshops, and Schools attended

- Oral Presentation on “Fabrication of Multi-Level 3D Microelectrode Arrays”, 2021 23rd European Microelectronics and Packaging Conference & Exhibition (EMPC), 2021.
- Oral Presentation on “Developments in multilevel three-dimensional microelectrode array technology”, 21a Conferenza Nazionale Sensori e Microsistemi: AISEM 2022.[Invited talk]
- Oral Presentation on “Influence of ultrasonic bath on mold-assisted electrodeposition of gold microelectrode arrays”, XXXV EUROSENSORS Conference: Eurosensors, 2023.

Acknowledgment

I extend my heartfelt gratitude to Dr. Leandro Lorenzelli, my thesis supervisor, for entrusting me to this interesting research topic. Throughout the challenges posed by the COVID pandemic, Dr. Lorenzelli's support and encouragement were invaluable. Dr. Lorenzelli's breadth of knowledge in microsystems technology and his exemplary humility serve as sources of inspiration for my personal and professional growth. Furthermore, I am grateful for his understanding and flexibility, allowing me to work at a pace conducive to my academic journey.

I am deeply grateful to my thesis advisors, Prof. Ing. Gian-Franco Dalla Betta and Dr. Andrea Adami, for their invaluable support and guidance during my academic endeavors. Their unwavering availability and willingness to address any doubts or concerns that arose throughout my research journey have been instrumental in shaping the outcome of my thesis.

I am profoundly thankful to Flavio Giacomozzi, whose guidance and mentorship were invaluable to me throughout this journey. His extensive expertise in microfabrication and cleanroom technologies has provided me with invaluable insights and opportunities for learning. I extend my gratitude to Severino Pedrotti and Paolo Mattevi for their consistent support and assistance whenever I required their help. Their willingness to offer guidance and share their knowledge has been instrumental in overcoming challenges and achieving milestones in my academic pursuits.

I am immensely thankful to Prof. Sergio Martinoia and Dr. Donatella Di Lisa for their invaluable support in validating the device performance, ensuring the accuracy of our results. Additionally, I extend my gratitude to colleagues Alessandro Cian, Dr. Damiano Giubertoni, and Dr. Rossana Dell'Anna for their expertise in materials processing, which enriched our research. Special thanks go to Dr. Andrea Spanu for his continuous support and insightful discussions, which greatly contributed to the project's success.

I had the privilege of interacting with several exceptional researchers and fellow PhD students throughout my journey, from whom I gained valuable insights, either directly or indirectly. Among them are Dr. Ashish Bisht, Dr. Federica Mantegazzini, Teferi Sitotaw Yallew, Giulia Di Gregorio, Dr. Ankur Sinha, Alessandro Irace, and Johanna Mae Indias. Their diverse perspectives and contributions greatly enriched my understanding and enhanced the quality of my work. Furthermore, I am profoundly grateful to Inci Ruya Temel and Dr. Felix Klaus Ahrens for their selfless assistance during the final stages of my PhD, which was invaluable in bringing the project to fruition.

I would like acknowledge the MUR-PNRR project SAMOTHRACE (ECS00000022) for supporting the a part of this research work financially.

Finally, I express my gratitude to my family members in India: my mother, Mrs. Suman Devi; my sisters, Sarita and Poonam; and my father, Mr. Ajit Singh. Their unwavering

support and encouragement have been sources of strength throughout my journey. Additionally, I am thankful to my friend, Dr. Manisha Sharma, who has been a patient listener and a pillar of support. Despite the distance, their kindness and understanding have been a constant source of motivation for me.
Neeraj Yadav